Assessing the drivability of a monopile through the rock armour layer

An analysis using Discrete Element Method and small-scale testing

Teodora Elena Barbuntoiu

Assessing the drivability of a monopile through the rock armour layer

An analysis using Discrete Element Method and small-scale testing

by

Teodora Elena Barbuntoiu

to obtain the degree of Master of Science

at the Delft University of Technology

to be defended publicly on the 22nd of November 2021 at 13:00 p.m.

TUDelft
Delft
University of
Technology

Boskalis

Summary

Deployment of renewable energy is essential to reach a carbon neutral economy. Offshore wind farms have caught the interest of many developed countries since they are an essential source of green energy. The interest of this thesis lays in the design of the foundation used for offshore wind farms, in particular the interaction between the monopiles and the scour protection layer. An optimised one-stage installation process for the scour protection is investigated, which consists of first placing the rock armour and then driving the monopile through the entire scour protection layer. This is an efficient method to reduce the installation time and the operational cost.

The purpose of this research is to identify the limitations which are related to the penetration of the monopile through the stone armour. The scour protection material is composed of large diameter rocks, which can hinder the penetration of the pile, or even damage the tip of the pile. A restricting ratio of the mean size of the rock (d_{50}) to the thickness of the monopile wall (w) is explored, as well as an investigation of the effect of penetration resistance on different material and geometry characteristics. The first research method employed is a literature study, which proves that the analytical formulation of the axial capacity provided by the available standards is inappropriate for the application of this thesis. Thus, two other research methods are identified, which include designing an experimental small-scale test and a Discrete Element Model (DEM) of a penetration test.

DEM is an applicable numerical model for the application for this thesis since one can investigate the motion and effect of individual rock particles at each time step. In addition, it can capture the interaction between the pile and the particles during the installation process very well. Previous research on the DEM modelling of a penetration test reveals that there are numerous studies which investigate the scenario of a thick object penetrating soil-like material, however no research was done using a d_{50}/w larger than unity. With respect to the shape of particles used in DEM, several authors have identified the need to use non-spherical particles, thus this research makes use of both multi-spheres are polyhedrons to represent more accurately the shape of the armour rocks.

A preliminary analysis identifies a calibration strategy for the input parameters of the DEM penetration test. The model environment involves a dry quasi-static penetration of a plate in a coarse granular medium. To reduce the large computational time, techniques such as shape simplification, scaling, reduction of elastic modulus and domain are revised. The plan for calibration consists of checking available literature to define constant, dependent and independent variables for the DEM model. A Design of Experiments (DoE) approach is used to plan the simulations such that an optimised set of input parameters can be achieved. The presented calibration plan is then applied on a case study which uses an experimental lab test with a recorded penetration resistance for a case of d_{50}/w equal to 1.8. A sensitivity analysis reveals that the plate penetration velocity is an important parameter and needs to replicate the speed used in the laboratory. Particle shear modulus directly influences the computational time, however, one needs to use a realistic value as an input parameter such that similar material bulk behaviour to the experimental test can be accomplished.

It is then decided that further calibration of the DEM input parameters based on this case study test is not feasible given the organizational structure of this thesis project. Therefore, a specialised laboratory penetration test experiment is designed such that it can contribute to the calibration of the DEM model, but also provide with a data set of penetration residence for multiple ratios d_{50}/w. The choice of domain, scale, particle size, geometries and kinematics are chosen such that it aids replication of the test set-up in DEM. Additional tests such as the Angle of Repose (AoR) provide an insight into the micro and macro behaviour of the material. Among the observations of the experimental test, buckling of the thinnest plate during the most extreme case (largest d_{50}/w) is experienced, as well as breakage of the rocks under the tip of the pile is observed. The penetration resistance recorded during the test shows an

increasing force over depth with larger particle sizes. It is also shown that for the same ratio d_{50}/w reached in two separate experiments, the work required for penetration is higher when using a wider plate.

A DEM model is constructed based on the laboratory experiment. The calibration consists of performing a DoE strategy, where the static friction and rolling friction coefficients between particles are optimised. The results of the calibration study identify that only the spherical particle show bulk behaviour similar to what was found during experimental testing, whereas multi-spheres and tetrahedrons underestimate the penetration resistance. Furthermore, the final set of input parameters for the spherical particles is verified and validated using the results from the additional experimental tests. With the purpose to investigate the dependence of penetration resistance on the ratio d_{50}/w, multiple simulations are conducted in DEM. Same ratios as used during the experimental testing are accomplished using the same particle size for the reference case and varying the width of the plate. The results show potential bottom boundary effects for the wider plate which results in a higher penetration force. When replicating the exact same plate width and particle size as considered during the experiments, only the results of the larger rock sizes can then be validated. It is thus concluded that a different calibration procedure is required for the smaller particles, due to a non-linear dependence of the force on the ratio d_{50}/w.

A combined conclusion from the experimental and DEM results indicates two regimes for the penetration resistance. First, a lower regime which is described by a constant and relatively low value for the penetration resistance and then an upper regime characterised by a steady increase in the force. The threshold between the two regimes is identified as $d_{50}/w = 3$, which becomes the limiting relation inquired by the research question. It is imperative to highlight that the full scale scenario of a monopile penetrating through the scour protection layer is a much more complex process and one of the major distinctions with the methods investigated in this thesis is different boundaries conditions for the two scenarios. Nevertheless, it is suggested that the ratio to be considered as a conservative estimate of the threshold after which the monopile will be more likely to experience a hindered self-weight installation in the scour protection layer.

Among the recommendations of this thesis, one can mention the need to improve the calibration strategy for non-spherical particles, but also to create a separate set of calibration input parameters for the lower regime. Moreover, it is suggested the need to perform additional experimental and DEM simulations to validate the limiting ratio found in this research. Also, a more complex set-up may be investigated, such as creating a submerged penetration or layering for the material, as well as adding a dynamic load for the plate penetration. Lastly, it is recommended a larger scale test model to better quantify the effects of scaling, boundaries and geometry simplifications made in this research.

Preface

This thesis was written during the COVID-19 pandemic, times when the university was mostly closed, as well as the access to company office was restricted. This thesis is the product of another great cooperation between TU Delft and Boskalis. Remote connection, virtual meetings and work at home were part of my daily routines for this research. I was fortunate enough to be able to get excellent guidance from both university and company supervisors.

I would like to take the opportunity to express my gratitude to everyone involved in this project. First and foremost, Ike van Giffen and Rene Thijssen for their continuous perseverance, help and support throughout this process, even in moments when I seemed to hit the wall. Moreover, I thank Javad Mohajeri for his continuous help with solutions and guidance regarding the thesis and the numerical model. I would also like to thank Dingena Schott who provided me with the software licence and access to the much needed hardware.

Furthermore, I would like to extend my appreciation for all their assistance to the last two members of my committee, Ken Gavin and Amin Askarinejad. Moreover, thanks to Ed Stock, I was allowed to perform lab testing in the dredging laboratory in 3mE faculty. I would also like to thank the engineering team of Vuicon who helped with the experimental set-up on such short notice. I also acknowledge Etienne Alderlieste from Deltares who provided me with data I used especially during the first period of my research.

Last but not least, I would like to thank my parents, my sister and Walid for all their support especially during these difficult times.

Teodora Elena Barbuntoiu
Delft, November 2021

Contents

List of Figures

List of Tables

Nomenclature

Abbreviations

AoR	Angle of Repose
API	American Petroleum Institute
CFD	Computational Fluid Dynamics
CPT	Cone Penetration test
DEM	Discrete Element Modelling
FEM	Finite Element Method
FFD	Full Factorial Design
HM	Heavy Grading
IFR	Incremental Filling Ratio
KC	Keulegan - Carpenter number
KLT	Kanade Lucas Tomasi Tracker
KPI	Key Performance Indicator
LM	Light Grading
OWT	Offshore Wind Turbine
PSD	Particle Size Distribution

List of Symbols

α_{AoR}	Angle of repose
β	Shaft friction factor
δ	Friction angle pile-soil
δ_n	Normal overlap
δ_t	Tangential overlap
μ_r	Coefficient of rolling friction
μ_s	Coefficient of static friction
ν	Poisson's ratio
ω_i	Unit angular velocity
ϕ	Internal friction angle
ρ	Density
σ'_{hf}	Horizontal effective stress at failure

σ'_{v0}	Effective vertical stress in-situ
τ	Torque
τ_{s-lim}	Limiting shaft resistance
τ_{sf}	Ultimate unit shaft resistance
θ	Angular distance
A_{over}	Overlapping Area
c_h	Consolidation coefficient
C_n	Normal damping coefficient
C_t	Tangential damping coefficient
D	Horizontal domain extent
d_{50}	Mean rock size
D_{AoR}	Diameter cylinder AoR
D_{out}	Outer diameter of the pile
E'	Equivalent Young's modulus
E	Young's Modulus
e	Coefficient of restitution
F_t	Tangential force
f_{crit}	Critical load
F_n	Normal force
G'	Equivalent shear modulus
G	Shear modulus
H	Vertical domain extent
h	Height penetrating object
H_{AoR}	Height cylinder AoR
HB	Hardness Number
I	Second moment of area
$I_{s,50}$	Point Load Index
k	Hydraulic conductivity
L	Length pile
l	Length penetrating object
L_p	Plug pile length

L_{dom}	Length rectangular domain	R_{min}	Smallest particle size
m'	Equivalent mass	R_{NK}	Effective radius
m	Mass of each particle	S_n	Normal stiffness
N	Scaling factor	S_t	Tangential stiffness
n	Porosity	T_h	Contact time
N_q	Bearing capacity factor	T_r	Theoretical maximum time step
P	Load	V	Normalised velocity
p	Pressure	v	Penetration speed
Q_b	Base resistance	v_c	Critical velocity
q_{b-lim}	Limiting base resistance	v_n^{rel}	Normal relative velocity
Q_{bf}	Base resistance at failure	v_t^{rel}	Tangential relative velocity
q_{bf}	Maximum stress mobilised at the base	v_{AoR}	Lifting speed AoR
Q_{in}	Inner shaft friction	V_{over}	Overlapping volume
Q_{out}	Outer shaft friction	V_{ult}	Axial capacity
Q_{sf}	Shaft resistance at failure	W'_{pile}	Submerged weight of the pile
R'	Equivalent particle radius	W	Weight of the pile
R	Radius of each particle	w	Width penetrating object
R_a	Roughness interface	W_p	Buoyant weight of of the plug
R_i	Distance contact point to centre of mass	W_{dom}	Width rectangular domain
R_{disk}	Effective disk radius	z	Penetration depth

<div align="right">

1

</div>

Introduction

1.1. Background

The continuous development of strategies concerning the deployment of renewable energy sources is a key aspect in the transition to a cost-effective carbon neutral economy (Almuni et al., 2020). The European Environmental Agency acknowledges that renewables are a fundamental pillar in achieving the decarbonisation plan, which is part of the EU's climate commitments under the Paris Agreement[1]. Wind power is currently an essential source to generate green electricity for various uses and its main advantages are the fact that it is safe, non-polluting, renewable, widely distributed and unlimited (Zheng et al., 2016). In 2019, wind power represented 22% of worldwide renewable energy generation, which explains why wind energy remains the fastest growing technology on a global scale (Almuni et al., 2020).

Construction of offshore wind turbines (OWTs) comes with several disadvantages in comparison to those land based. Installations and maintenance cost are generally higher, as well as the difficulty to connect them to the local energy grid (here it can also be mentioned the added cost of a pipeline which needs to connect the offshore to the main land). On the other hand, offshore winds are more abundant, stronger and more consistent than those inland (Wang et al., 2015). Since the driving force of these structures is a natural resource, the choice of their location is highly dependent on the direction and strength of the wind. In addition to this, noise pollution is not a problem and the efficiency of the turbines is the highest since there is unobstructed wind out in the sea.

Figure 1.1 shows the current challenge for the engineers of OWTs foundations. Over the years, the size and power generated by the turbines has increased, which indicates that the technology that was available a decade ago, is now outdated. In order to make the step and double the energy production of an OWT, the turbine size needs to be increased, which has a direct influence on the hub height. A taller tower implies larger foundation which needs to sustain this increase in load. In itself, this is not a problem, however clients and contractors in the offshore industry are continuously looking for ways to cut down expenses originating from the increased size. For instance, Veja Mate offshore wind farm project (Boskalis, 2016b) required the installation of 67 OWTs in the North Sea in a very short time (2015-2016). The size of the monopiles and the constrained time of installation lead to a modified design, which will be later explained in Section 1.2.

---

[1]The Paris Agreement's aims is to strengthen the global response to the threat of climate change by keeping the global temperature rise this century well below 2 °C above pre-industrial levels and to pursue efforts to limit the temperature increase even further to 1.5 °C (Almuni et al., 2020)
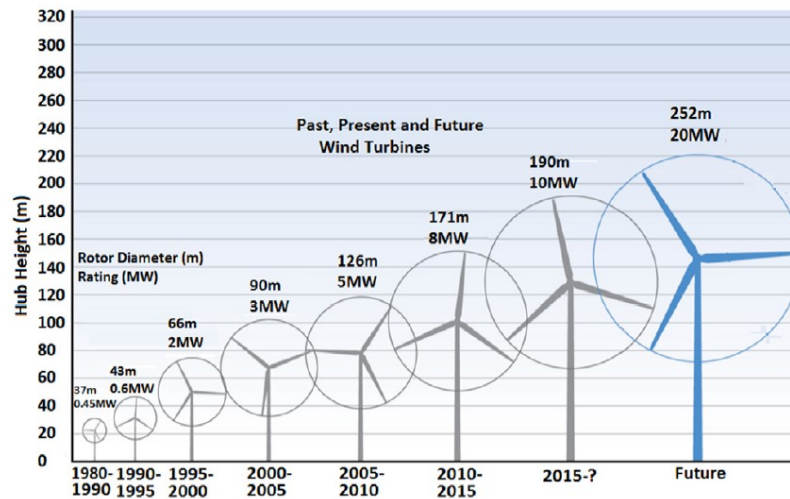
Figure 1.1: Trend growth of size and power of wind turbines (Igwemezie et al., 2019)

The historical evolution of offshore wind farms foundation suggests that monopiles remain the most cost-effective type of foundation provided that there are suitable ground conditions. Doherty and Gavin (2012) state that monopiles are by far the most common support structure, accounting for over 75% of existing turbine foundations. The main reason is the economical benefit due to low production and installation costs. Initially used for shallow water depths, there is a clear trend of transition to deeper water (for instance 50 m depth). This poses certain issues for the design of the foundation as the slenderness ratio and the diameter of the monopile may need to consequently increase. In perspective, the cost of the wind turbines support structures is about 30% of the total cost of the offshore wind farm (Leblanc, 2009). Therefore, considering the great expense of the foundation in such a project, an overview of the support structure of a monopile needs to be made.

Figure 1.2 shows the components of a monopile, highlighting both the substructure and the foundation. The work platform connects the structure with the OWT while the J-tubes have the role to support and protect cables. The monopile can penetrate in the ground in order to provide stability for the vertical and lateral loading of the foundation. Figure 1.2 also identifies the scour protection layer, an additional layer of material which, as it names says, aims to prevent scouring at the base of the monopile. The scour protection represents the focus of this study, thus a more extensive description will be made later in the thesis.
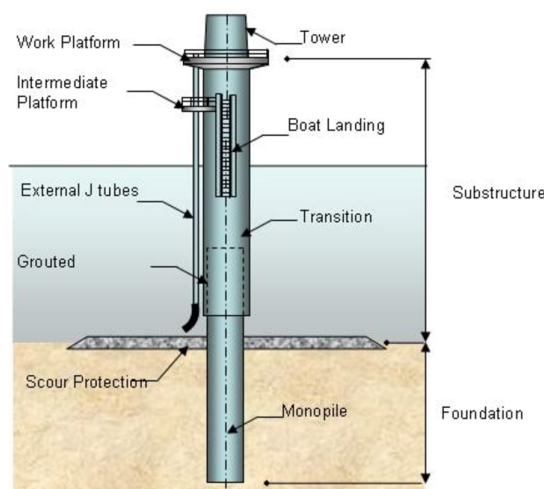
Figure 1.2: Monopile foundation overview (Garcia, G, 2012)

1.2. Problem analysis

Monopile installations of OWTs come with an immediate problem relevant to the geotechnical design. The process of scouring is a natural phenomenon which happens in an submerged environment in the surroundings of an embedded object. The flow of water, mainly due to waves, currents and tidal variations erodes and creates a hole in the soil. Moreover, many of the wind farms are located in places where sediments are mobile due to severe hydrodynamics conditions. CIRIA et al. (2007) acknowledges that scour is detrimental to the stability and lifetime of the foundation due to resonance behaviour of monopiles, which is highly dependent on the embedded depth and the rock armour thickness.

Unprotected OWTs monopiles naturally develop in time an erosion hole around the structure. Therefore, it is important to outline two main approaches to protect the objects against scouring effects, as shown in Figure 1.3. In a static design, the scouring process is prevented and the seafloor is protected by placing the armour layer immediately after installation of the monopile. The second approach is a mitigation measure and consists of allowing a scour pit to form until an equilibrium is reached and only then, the scour protection is installed, with the purpose to prevent any additional scouring.
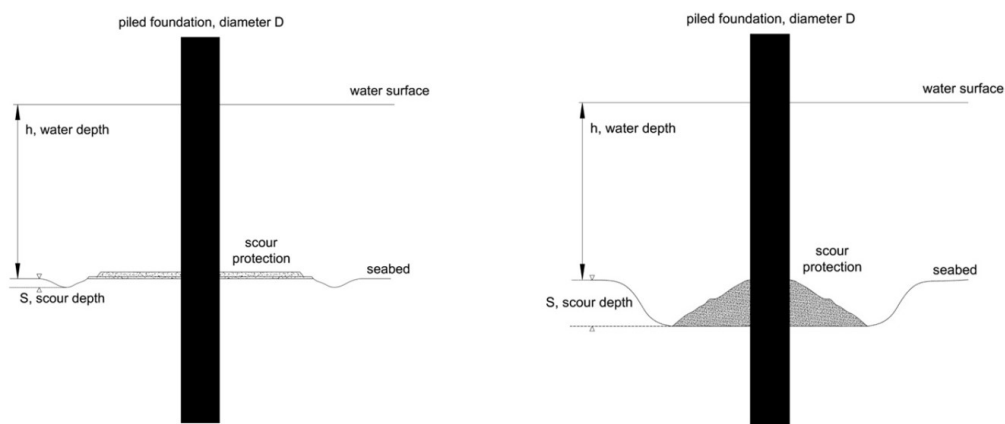
Figure 1.3: Left: Scour protection laid on seabed before or shortly after installation of the pile. Right: Scour protection laid as a mound in the already developed scour hole (Whitehouse et al., 2011)

In the static design of a scour protection, it is a common practice to lay down the filter layer (if needed) before the installation process of the pile begins. After the pile has been fully installed, the rock armour layer can be placed at the base of the monopile. However, this process lacks efficiency since the vessel which provides the scour protection material needs to leave after placing the filter layer and then to return to lay down the stone armour. This two-step approach of rock dumping is not cost-efficient due to higher vessel transportation costs but also since it is a major drawback for the project management as it creates an additional stage in the project planning. On top of this, from an engineering perspective, if the rocks are placed after the pile is installed, one can identify the risk of damage to the structure (even when the rock material is precisely positioned by a fallpipe vessel), but also a more complex dumping process since the vessel orientation needs to be altered during the installation.

It is thus proposed that in order to optimize the installation processes of the monopile and the scour protection, one should pre-install the filter layer along with the stone armour layer, and then drive the monopile through it. This would reduce the rock placement process to one step, allowing for a faster discharge of rocks (less caution is needed since the pile is not yet installed). This is an efficient way to reduce the installation time of the pile and the scour protection, while decreasing the transportation costs. For instance, this process was successfully implemented in a project when time constraints were the main problem. Pile-driving operations for Veja Mate offshore wind farm in Germany took each 24 h and were done after the scour protection layer was laid. Initially, a fallpipe vessel executed the sub-sea rock installation of the filter layer and the stone armour, and only then the pile was driven through it (Boskalis, 2016a). The project was successfully finished and opens the possibility to use this technique for future operations as well.

1.3. Research objective

Bearing in mind the trend of increased monopile sizes and the idea of minimizing the OWT foundation costs, one might investigate the possibility to optimize the installation process of such structures. The solution discussed in this thesis refers to placing the filter and rock armour layers on the the bed soil prior to the installation of the monopile. Research has been extensively done on driving of pile through sand or clay, however, there is a gap in the available literature on driving through a material with larger grain sizes (as required by the stone armour characteristics).

From the experience gained by the industry specialised in offshore installations, driving of a monopile through the armour layer could impose some challenges. For instance, if the wall thickness of the monopile in comparison to the mean diameter of the rock is not large enough, then some damage and increased resistance could be experienced at the tip of the pile. This raises the main research question of this study, which can be formulated as follows:

What are the limiting factors behind the self-weight penetration and subsequent driving of a monopile through the scour protection layer with regards to finding a relation between the mean size of the scour protection armour rock and the thickness of the wall of the monopile?

In order to answer the main research question, it is essential to quantify the pile resistance while driving through the rock armour to investigate whether the self-weight of the pile is sufficient for the penetration in the scour protection layer. Therefore, the following sub-questions come to complete the main research question of the thesis:

- *How does the penetration resistance change with depth with respect to its dependence on the characteristics the rock armour?*

- *What is the effect of changing the wall thickness of the monopile on the driving resistance of the monopile through the armour layer?*

A better understanding of the mechanism behind driving of monopiles through armour rock reduces the risks of such operations. This research provides guidance on the limiting factors and brings more confidence for any design requiring a pre-installed scour protection. Pre-installation of the stone-armour is a promising cost and time saving strategy, as it is predicted to become a standard practice in the installation process of monopiles for OWTs.

1.4. Research method

Several research methods have been designed in order to reach the scope of this thesis. An integrated approach is implemented in this thesis, where both an experimental test and a numerical model are used to simulate the penetration of the monopile through the rock armour layer. The main methodological steps can be structured as follows:

1. **Literature research** is the starting point of this thesis. It is important to describe with the available scientific books and papers, the theory behind monopile driving, key geotechnical aspects and rock armour design. Lastly, the numerical method, Discrete Element Method (DEM) is described, focusing on the theoretical background and the applicability to the topic of this thesis.

2. **Experimental small-scale testing** is performed with the purpose of providing a data-set with various penetration resistance for different case studies. Moreover, this data can be used for calibration, verification and validation of the DEM model.

3. **DEM** is the numerical model chosen to simulate the self-weight penetration of the monopile through the rock armour. For the objective of this research, parameters such as the mean rock size and the wall thickness of the pile are to be varied in these simulations.

1.5. Report structure

In this section, an outline on the report structure and contents is made. The three research methods are highlighted in the corresponding chapters. A standard procedure for DEM modelling includes model setup, simulations, validation with experiments or available data sets, discussion and conclusion. Thus, this thesis aims to incorporate these steps in the respective chapters with the aim of answering the main research question of the paper. Figure 1.4 shows the chapters included in the main body of the thesis.
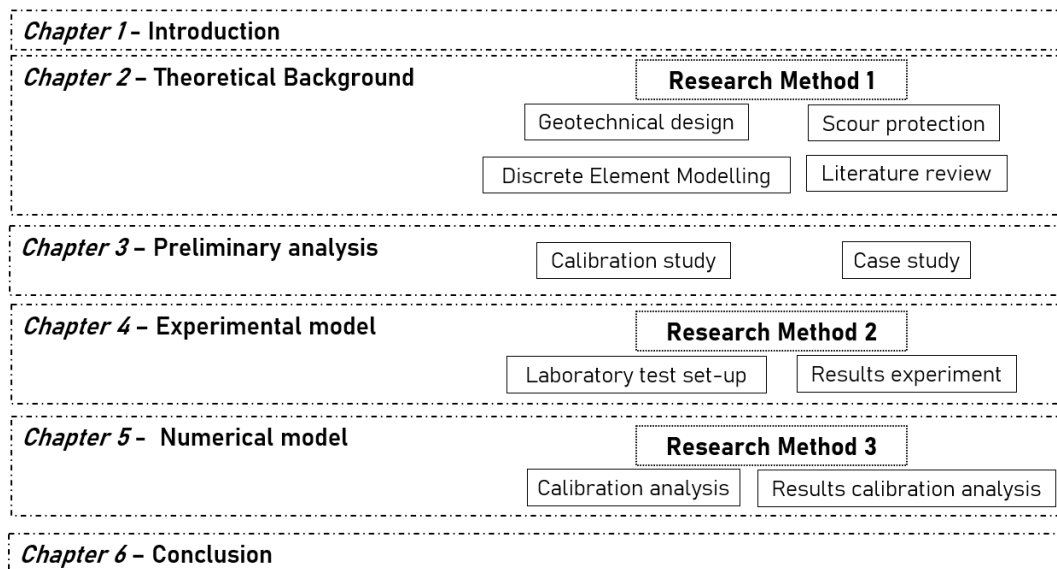
Figure 1.4: Overview of the structure of the thesis report including research methods and chapter division

Chapter 1 involves an introduction to the topic of offshore monopile installations and incorporates the relevancy of the topic for current industry demands and the objective of the research from an academical point of view.

Chapter 2 includes the first research method, which refers to creating a theoretical background for the topic. Aspects such as principles of design of monopile foundations, scour protection but also Discrete Element Modelling theory are introduced to the reader. Lastly, an overview with the state of the art in the available scientific literature is included.

Chapter 3 brings a preliminary analysis, which involves a calibration study designed for a DEM penetration test. The chapter also includes a case study, which involves applying this calibration study with the purpose to numerically replicate an already existing laboratory penetration test.

Chapter 4 describes the experimental test conducted in this research. The test involves the penetration of a plate into a coarse granular medium. A discussion and conclusion are constructed around the main results revealing the penetration resistance for various ratios of size of the particles to thickness of the penetrating tool.

Chapter 5 aims to replicate the previously performed laboratory experiments in a DEM software. The model needs calibration, verification and validation. Results of each of these steps are included and conclusion are drawn on the applicability of the numerical model to answer the main research question.

Chapter 6 brings the research to an end by outlying the main findings of this research. The objective of the thesis is revised and conclusions are drawn. Recommendation for future research is also included in this chapter.

2

Theoretical Background

The theoretical background chapter comes with an overview of the main aspects related to the topic of monopile driving through the armour rock. In particular, geotechnical aspects related to the installation of the piles are identified in Section 2.1. Next, scour protection characteristics are included in Section 2.2. The theory behind Discrete Element Modelling is presented in Section 2.3. Lastly, the literature search in Section 2.4 identifies the state-of-art with respect to DEM modelling of penetration tests.

2.1. Geotechnical design of monopiles

The geotechnical engineering team has to construct one design for each cluster of OWTs with similar depths and soil conditions. The main difficulty of the monopile foundations is that their weight is relatively low, making the applied vertical load smaller than the overturning load generated by wind or waves (Byrne and Houlsby, 2003), in contrast to the loading conditions in gravity based solutions. Open ended monopiles offer superior moment resistance, high axial capacity and can be driven to greater depths to provide larger tension resistance (Gavin, 2020). Randolph and Gourvernec (2011) group the numerous aspects related to the geotechnical design of piles as follows:

- Installation (drivability, hole stability and grouting)

- Axial capacity and performance under axial cyclic loading

- Lateral capacity and performance under lateral cyclic loading

- Group effects (leading to an overall foundation stiffness)

- Other considerations (seismic response, local seabed stability and scour).

The overview provided by Randolph and Gourvernec (2011) is applicable to both onshore and offshore pile foundations, thus not specific to monopiles for OWTs. Due to the specific scope of this thesis, not all of the above mentioned topics are worth to be discussed in this paper. It is thus considered to focus the attention on the following:

- Types of piles, see Section 2.1.1

- Axial capacity, see Sections 2.1.2

- Drivability issues, see Section 2.1.3

- Scour protection, see Section 2.2

2.1.1. Characteristics of piles used for OWTs

Pile can be classified as either displacement pile, such as driven piles, and non-displacement piles, for instance bored piles. In the offshore environment, driven piles are the most common due to several advantages: fast method, underwater hydraulic hammers, compaction of the soil resulting in increasing the bearing capacity of the piles, pre-casting the piles (for concrete piles) and the ability to be checked for quality control purposes before the installation.

Offshore piled foundations can also be seen as piled jacket structures or monopiles. The main difference is that jackets provide the required structural stiffness by increasing the substructures surface area or by concentrating mass away from the central axis (Damiani et al., 2016). Therefore, the diameters of the piles are significantly different, jackets requiring 1 up to 3 m, while monopiles between 2 up to 7 m (see Table 2.3). However, considering the trend identified in Figure 1.1, new designs of the monopile are now using diameters between 8 and 11 m.

In the last couple of years, the need to build deeper foundation on more difficult soil conditions is remarked. By consulting the latest industry demands, an estimation of the monopile characteristics was done in Table 2.1. The values displayed are chosen as an average of the current demands in offshore wind industry. The table includes the dimensions of the turbine, as well as the diameter (D_{out}), length (L), thickness of the wall (w) and weight of the monopile (W).

Table 2.1: Example of OWT open-ended monopile characteristics (own research)

Turbine (MW)	D_{out} (m)	L (m)	w (mm)	W (t)
10	8	90	70	1300

2.1.2. Design methods

Several aspects of the geotechnical design of the monopiles are mentioned in this section. As previously indicated, one of the sub-research questions identifies the necessity to get the penetration resistance in order to answer the main research question. It is thus considered necessary to start this research with an overview on the analytical ways to calculate the penetration resistance. For instance, axial capacity is introduced, including the main approach to analytically calculate it using the guidance from various standards.

The axial capacity or strength of the pile is the maximum load which can be applied to the pile without causing failure. It depends on the stress changes during installation, due to the mobilisation of the stresses and densification of the soil because of the need to accommodate the pile volume (Igoe et al., 2010). The load bearing capacity of the pile is represented by the shaft (side) resistance and tip (base) resistance. The side resistance is usually mobilised early in the loading progress, which implies that any additional axial load is transferred to the base, which makes the base resistance of the highest importance in the design of the pile (Lee and Salgado, 1999).

This axial strength of the pile can be calculated using the shaft resistance (also referred to as shaft friction or skin friction), the base resistance and the buoyant weight of the pile as indicated in Equation 2.1 (Pisanò, 2020). For open-ended pile, the shaft resistance is calculated for inner and outer side of the pile, while the base resistance applies only to the surface area at the tip (ring shape).

$$V_{ult} = Q_{sf} + Q_{bf} - W'_{pile} \qquad (2.1)$$

where:

V_{ult} = Axial capacity (kN) Q_{bf} = Base resistance (kN)
Q_{sf} = Shaft resistance (kN) W'_{pile} = Submerged weight of the pile (kN)

For the purpose of this thesis, only the formulas applicable to granular, cohesionless soils (such as sand) are included. Thus, the shaft resistance can be calculated using the Coulomb's law of friction as included in Equation 2.2 and the base resistance is computed using the formula in Equation 2.3. The calculation of the ultimate shaft resistance and the maximum stress mobilised at the base can be a challenge because during installation and loading stage, as the in situ conditions of the soil change into failure mode in order to allow for the penetration of the pile.

$$Q_{sf} = \pi D_{out} \int_0^L \tau_{sf}\, dz = \pi D_{out} \int_0^L \sigma'_{hf} \tan \delta\, dz \tag{2.2}$$

where:

D_{out} = Diameter of pile (m) τ_{sf} = Ultimate unit shaft resistance (kPa)
L = Length of pile (m) δ = Friction angle pile-soil (^{o})
σ'_{hf} = Horizontal effective stress active on the pile shaft at failure (kPa)

$$Q_{bf} = \frac{\pi D_{out}^2}{4} q_{bf} \tag{2.3}$$

where:

D_{out} = Diameter of the pile (m)
q_{bf} = Maximum stress mobilised at the pile base (kPa)

API (American Petroleum Institute) Recommended Practice (RP2A) indicates the most common design method to calculate the components for the axial capacity of piles in sand. Also known as the $\beta -$ $approach$, the ultimate unit shaft resistance τ_{sf} in sand can be predicted using the formula in Equation 2.4. The shaft friction factor and the limiting shaft resistance depend on the soil type and density, as shown in Table 2.2. Moreover, API recommends the calculation of the base resistance q_{bf} using shallow foundations theory, for instance using Terzaghi's bearing capacity factors which are a function of the friction angle of the soil ϕ. Thus, Equation 2.5 shows the base resistance calculated using the end bearing factor, which decreases inversely proportional with the stress level (Randolph and Gourvernec, 2011).

$$\tau_{sf} = \beta \sigma'_{v0} \leq \tau_{s-lim} \tag{2.4} \qquad\qquad q_{bf} = N_q \sigma'_{v0} \leq q_{b-lim} \tag{2.5}$$

where:

σ'_{v0} = Effective vertical in-situ stress (kPa) β = Shaft friction factor (-)
τ_{s-lim} = Limiting shaft resistance (kPa) N_q = Bearing capacity factor (-)
q_{b-lim} = Limiting base resistance (MPa)

Randolph and Gourvernec (2011) explain that API uses a database of load tests on mainly uninstrumented piles. Due to the weak theoretical base and the poor experimental correlations, the API method turns out to be unreliable for long and large diameter piles, as concluded by (Schneider et al., 2008). There are other available methods to calculate more accurately the shaft and base resistance, for instance CPT (Cone Penetration Test) base methods such as UWA-05 method, ICP-05, Fugro-05 and NGI-05. They incorporate the contribution of the effect plugging (explained in Section 2.1.3) and some other parameters such as effective area, relative density and correlations to the CPT cone resistance. For an overview of the above mentioned methods and their calculation methods, one should refer to the work of Schneider et al. (2008). For the purpose of the topic of this thesis, the introduced API method is considered sufficient, since it can be used to easily calculate a preliminary value for the axial capacity of the pile.

Table 2.2: API RP2A (2000) Selected design guidelines for shaft resistance calculation,
after Schneider et al. (2008) and Pisanò (2020)

Soil relative density	Soil type	δ	$\beta(-)$	$\tau_{s-lim}(kPa)$	$N_q(-)$	$q_{b-lim}(MPa)$
Medium dense to dense	Sand	25	0.37	81.3	20	4.8
Dense to very dense	Sand	30	0.46	95.7	40	9.6
Very dense	Sand & Gravel	35	0.56	114.8	50	12.0

2.1.3. Installation and drivability issues

Other topics related to the installation and drivability of the monopile in the subsurface are going to be discussed in this section. Although the available literature on material structure interaction is with respect to soil-like material, subjects like friction fatigue, plugging and interface friction are applicable to the interaction of pile and scour protection armour as well. Therefore, this section will consider a brief overview of these aspects with the purpose of highlighting the complexity of problem.

First of all, it is important to elaborate on the stress changes when the pile penetrate through a granular material since the stress level rises as the grains are radially pushed away from the pile tip. As the pile penetrated further, the grains reach the pile shaft, the stress level behind the tip is reduced. This phenomena is known as friction fatigue and leads to a reduced unit shaft resistance τ_{sf} with increasing distance behind the pile tip. With each blow of the hammer, the adjacent material gets sheared in a cyclic manner composed of contraction (at the tip of the pile) and relaxation stage (along the shaft). The mechanism of friction fatigue is confirmed using the results from Lehane et al. (1994), who constructed experimental pile tests and recorded the evolution of shear stress with increasing penetration depth of the instrument.

In an open-ended pile, the amount of displaced soil is lower than in closed ended pile, as the soil can advance in the inside of a pile. This is also known as plugging effect and has a direct influence on the resisting component of the axial capacity of the open ended piles. The degree of plugging can thus affect the degree of soil displacement and therefore the pile installation resistance. The degree of soil plugging can be described by the Incremental Filling Ratio (IFR) which is defined as the incremental change in plug length, L_p, relative to change in pile penetration, L ($IFR = \Delta L_p/\Delta L$). Fully plugged, means that no soil enters and the $IFR = 0$ $(-)$, while fully coring implies $IFR = 1$ $(-)$. For visualisation of the plugging mechanism, refer to Figure 2.1. The shaft friction is denoted as Q_{out} and Q_{in} depending if it is applicable to the outside or the inside of the pile, respectively. In case of plugging, the base base resistance is divided into two components, Q_{an} is applied to annulus the while Q_b only to the base of the soil inside the pile.

During static loading (e.g. when the acceleration of the pile is null), plug slippage will occur if the end bearing of the soil beneath the plug exceeds the friction generated between the internal soil column and the inner pile wall. This plugged/unplugged situation can be evaluated using the condition in Equation 2.6. The mechanisms controlling plugging during driving are complex and are influenced by pile diameter and inner pipe surface roughness (as shown in Equation 2.6), sand density, compressibility, but also driving energy (Brucy et al., 1991).

$$Q_{sf-i} > Q_{bf-p} - W_p \tag{2.6}$$

where:

Q_{sf-i} = Internal shaft friction (kN)
Q_{bf-p} = Base resistance plug (kN)
W_p = Buoyant weight plug (kN)
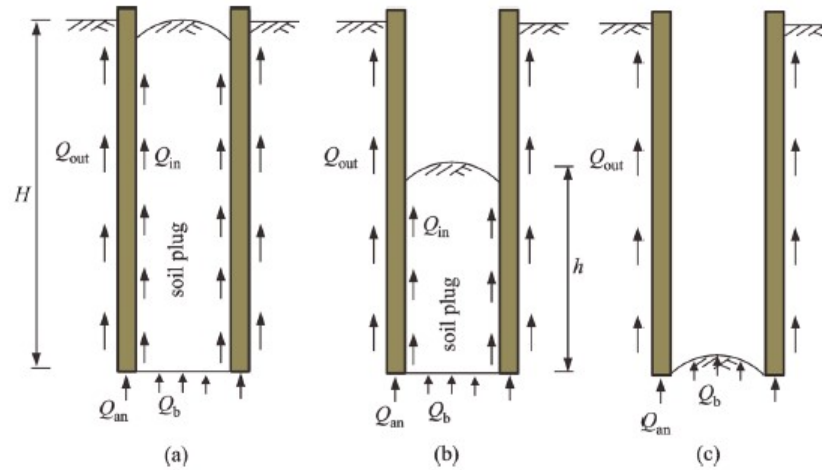
Figure 2.1: Modes of penetrations for open ended piles: (a) fully coring, (b) partially-plugged and (c) fully-plugged (Kumara et al., 2016)

The last aspect worth discussing here is the interface friction between pile and granular material. The friction angle pile-sand depends on the roughness of the interface (R_a) but also the mineral composition of the material and the shape of the grains. Provided that the sand particles are large, relative to the 'smooth' interface, then the shearing resistance is governed by sliding of the particles over the interface surface of the pile. The friction angle does not depend on the relative density of the material and as the mean diameter of the grains increases, the friction angle of the soil-pile interface dramatically decreases (Jardine et al., 1993). For example, with a typical roughness of the steel pile of $R_a = 10$ (-) and considering a coarse sand, then the friction angle soil-sand δ is between $20 - 24^o$ (Pisanò, 2020).

2.1.4. Conclusive remarks

What is very clear to conclude from this short overview on the current geo-technical analytical design is that the guidelines provided by various standards have never been verified using a different material of the subsurface, one that is not a soil type. Therefore, for the purpose of having a scour protection made out of rocks, the analytical formulation of penetration resistance is not sufficient to answer the research question. Therefore, this thesis needs to use other methods apart from the analytical approach to approximate the axial capacity of the monopile through the rock armour layer.

Nevertheless, the mechanism of material-structure interactions can be identified also when the pile penetrates the scour protection layer. Topics such as plugging and friction fatigue are also relevant when discussing the penetration of open-ended piles through the armour layer. Therefore, it is important to highlight the complexity of the problem and that the penetration resistance can be influenced by various factors which can make the real in-situ scenario harder to replicate in a numerical or experimental model.

2.2. Scour protection

The relevancy of the scour protection to the topic of this thesis was previously defined in the problem analysis Section (Section 1.2). Nevertheless, a more detailed description of the components and the standard practices is included in Section 2.2.1. It is also important to get an insight into the type material for the rock armour (see Section 2.2.2), knowledge which can later used to create a realistic setup for the experimental tests and DEM simulations.

2.2.1. Scour process

Scouring is a natural process which can be intensified by placing a structural element on the sea bed and interrupting the natural flow of water. Scour can have a direct effect on the bearing capacity of a foundation and on the structural response that governs the ultimate and fatigue load effects in structural components (DNV, 2010). The expected scour development depends on parameters such as dimensions and shape of the pile, seabed composition and hydrodynamic climate (Deltares, 2017), as it will be further explained.

The mechanics of scour identify two types of scour: local scour (steep-sided erosion pit around structural elements) and global scour (shallow eroded basin with larger lateral extent) (GL, 2012). In addition to this, edge scour occurs on the outside due to interaction of the flow with the structure and the protection. The main difference between local and global scour is with respect to the effective stress, as explained by Mostafa (2012). Since the effective stress depends on the weight of the soil above it, global scour comes with a reduced effective soil pressure at all depths, while for the local scour, only the effective stress near the pile is diminished.

In this section, the focus is laid on local scour, since it directly influences the design of the armour rock layer, as it will be described in Section 2.2.2. For detailed calculations of local scour extent, the reader should refer to the formulas indicated in the standard provided by DNV (2010). However, it is important to emphasise in this section the factors that influence the scour depth, lateral extension and time development. For the case of a steady current, the scour process is mainly caused by the presence of the horseshoe vortex. However, when waves are present, the horseshoe vortex and the lee-wake vortex (see Figure 2.2) form the scour process. This is governed by the Keulegan- Carpenter number KC which is a function of the wave period, diameter of the pile and maximum value of the orbital velocity at the bed.
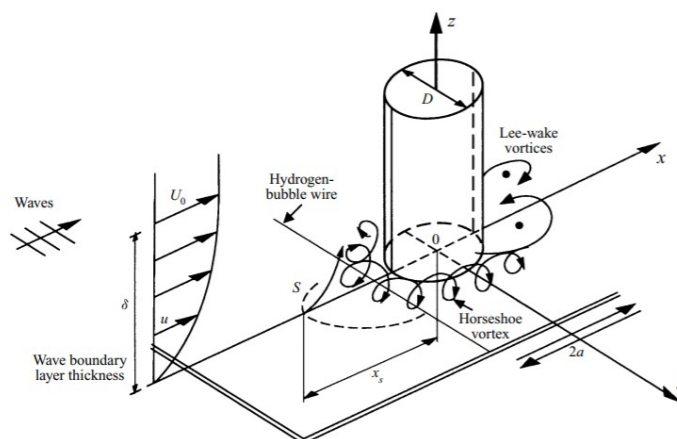
Figure 2.2: Flow around the base of a monopile (Sumer et al., 1997)

The scour depth is calculated using the Shields parameter, which is directly proportional to the square root of the bed shear velocity and inverse proportional to the mean bed grain diameter. Seabed erosion starts when the Shields parameter exceeds a critical value. Furthermore, the lateral extension of the scour hole can be estimated based on the friction angle ϕ of the soil, and assuming that the slope of the

scour hole equals this friction angle. The development in time of the scour cavity can be calculated using empirical formulas which make use a non-dimensional time scale, dependent on other parameters such as KC, Shields parameter, diameter of the pile and depth of the scour pit.

Kou et al. (2008) affirms that the theoretical equilibrium scour depth should be between 1.3 and 2.4 times the pile diameter (Sumer et al. (1992) and Melville and Sutherland (1998)). In practical applications, a lower factor of 1 to 1.5 is usually adopted (as shown in Table 2.3), and most contractors have a rule of thumb, considering the maximum depth of scour as 1.5 times the pile diameter. Matutano et al. (2013) made an overview on the various authors and their proposed methods of calculating the scour depth. A paper on methods of calculation of scour depth written by Zanke et al. (2011) proposes design curves for the equilibrium scour depth under the action of currents and waves. The new curve was fitted on an extensive data-set which shows the influence of the KC number but also the sediment characteristics.

Table 2.3: Scour evolution per each site location, after Whitehouse et al. (2011) (OWF- Offshore Wind Farms)

Location	Diameter Monopile (D_{out}) (m)	Maximum scour depth (m)
Scroby Sands OWF	4.2	$1.38D_{out}$
Arklow Bank OWF	5.0	$1.05D_{out}$
N7	6.0	$0.80D_{out}$
Scarweather Sands	2.2	$0.59D_{out}$
Egmond aan Zee OWF	2.9	$0.79D_{out}$
Otzumer Balje inlet	1.5	$1.47D_{out}$
Barrow OWF	4.7	$1.21D_{out}$
Kentish Flats OWF	5.0	$0.46D_{out}$
North Hoyle OWF	4.0	$0.13D_{out}$

Reviewing the classification of scour protection mechanisms, one can identify two main types: an immediate static design and a dynamic design. The former requires less maintenance and it is applicable to soil conditions with very mobile sediments and severe tidal currents and when scour can develop in days to weeks. This design consists of dumping the filter layer prior to monopile driving and then placing the armour around the foundation, with a usual entire installation time of a few months. Whitehouse et al. (2011) identified that the scour protection placed in a static design is an effective method to prevent the bed subsidence adjacent to the monopile foundations.

2.2.2. Rock armour

In order to avoid the formation of a scour pit, preventive mechanism such as the installation of rock armour, composite rubber mat, and collar are commonly used in OWTs farm projects. In addition to inhibiting erosion at the base of the monopile, these methods aim to decreases the danger of a pore pressure increase induced by the motion of the structure, also known as the liquefaction phenomenon (GL, 2012). An alternative to these measures is to create a much longer pile, however this is not in most cases the most cost-efficient method, since the manufacturing costs of additional pile length can outweigh those of scour protection. Thus, rock armour remains one of the cheapest and most used methods for prevention of scour protection.

Knowing the metocean data such as wave heights, peak periods, tidal currents velocities and water depth at each foundation, one can calculate the required stone size of the armour rock using the previously described Shield's criterion (see Section 2.2.1). Scour protection material should be designed to provide both external and internal stability. The former offers protection against excessive surface erosion of the scour material and the latter protects against transportation or suction of sediments from the underlying natural soil (DNV, 2010). In addition, there is a third geotechnical requirement, which is the flexibility of the scour protection to adapt for edge scour without completely failing. This "falling apron behavior" can also be visualised on the right image in Figure 2.3.

.
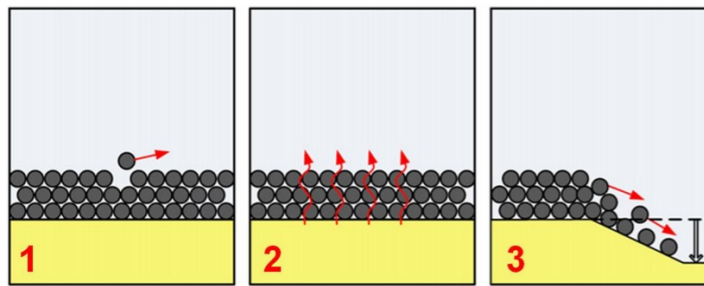
Figure 2.3: Technical requirements of scour protection: 1) external stability, 2) internal stability and
3) flexibility (Deltares, 2017)

The Rock Manual (CIRIA et al., 2007) emphasises the factors behind the choice of stone-armour. Having a calculation that indicates the required weight and quality of the rock is insufficient, since in most cases, a 'supply based design' is adopted. Suitable rocks for the armour stone are mostly igneous but also some sedimentary and metamorphic are acceptable, such as quartzite, limestone, gneiss, marble, serpentine and eclogite. In general, granite is used (a density of about 2650 kg/m^3), or a heavier rock such as gabbro (a density of about 3100 kg/m^3). Apart from the density requirement, the rock needs to be sound, compact, hard, durable, resistant to action of water and free of cracks and fissures. In some cases, however, the availability of certain type of rock existent at a local quarry dictates the design criteria of the stone armour. This was the case for Thornton Bank when the initial design gradation of $10/200kg$ was replaced by a stone mixture combination, as indicated in Table 2.4. This gradation and other characteristics of the quarried rocks will be explained below.

Table 2.4: Rock armour characteristics (own research)

Location	Density ρ (kg/m^3)	EN 13383 standard grading	Grading d_{85}/d_{15}
Thornton Bank	2700	$LM_{5/40kg}$ (20%) & $LM_{40/200kg}$ (80%)	5 (very wide)
Coastal Virginia	3100	$LM_{40/200kg}$	unknown
Veja Mate	2650	$LM_{10/60kg}$	2 (wide)
Gode Wind	3100	$CP_{90/250mm}$	unknown

The nominal rock size of which 50% of the rocks are smaller is known as the d_{50} or the mean rock size. The Rock Manual made by CIRIA et al. (2007) indicates the friction angle which is usually used by designers of scour protection. In general, for quarried rock, the friction angle ϕ should be $40 - 55^o$. A 'one-man stone' can be defined as a rock with a d_{50} between 100 to 300 mm, while a gravel is between 10 and 80 mm. Angular shaped gravels can also have very high friction angle, a loose packing comes with $\phi = 39^o$, while a densely packed gravel has $\phi = 45^o$. Other important characteristics of the material are defined using the EU standard grading, as exemplified in Figure 2.4. In the plot, the following notations are used:

- ELL (Extreme Lower Limit): no more than 5% of mass is permitted to pass.

- NLL (Nominal Lowe Limit): no more than 10% of mass is permitted to pass.

- NUL (Nominal Upper Limit): no more than 70% of mass is permitted to pass.

- EUL (Extreme Upper Limit): no more than 97% of mass is permitted to pass.

Using the Rock Size Distribution from Figure 2.4, one can understand the EN 13383 standard grading requirements used for the design of stone armour (refer to CIRIA et al. (2007)). A distinction between heavy (HM), light (LM) and coarse (CP) grading is made. The latter is mostly used for filter layers. Table 2.4 shows the grading, as well as NLL/NUL of each material used in various projects. The armour-stone grading is related to uniformity using the ratio d_{85}/d_{15}. Narrow grading is used when the ratio is less than 1.5, and wide gradation for values between 1.5 and 2.5. The grading generally becomes wider
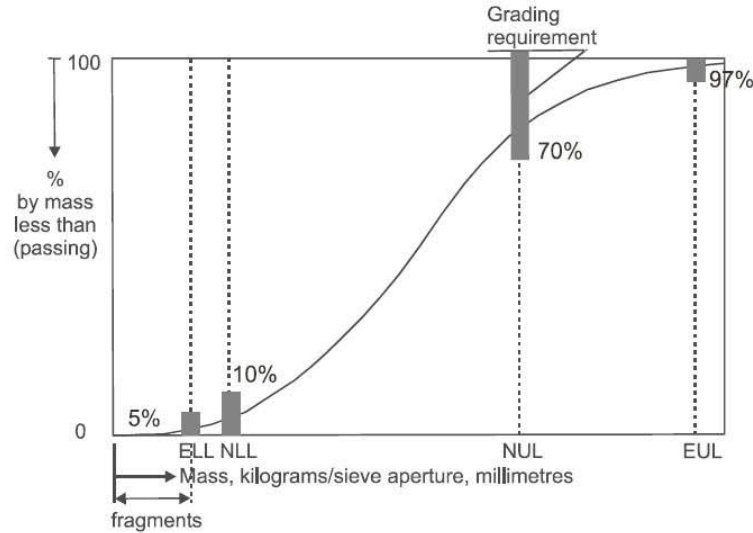
Figure 2.4: Rock size distribution - EU standard grading (CIRIA et al., 2007)

as it become lighter (LM). Since for stone-armour heavy graving (HM) is required, a narrow graded is usually adopted. However, Table 2.4 shows there are exceptions to these guidings. The designers prefer to use light grading (LM) and heavier stones, which comes back to the previously point, that the material used for the stone armour is highly dependent available quarried material.

Having established the general characteristics of rocks used for the stone-armour, it is relevant to show some past projects of OWTs farms and their design of rock armour. Table 2.5 indicates the d_{50} of both the scour protection and the rock armour in several projects, as well as their respective layer thicknesses. In addition to the data set presented in this table, there are two rules of thumb for an easy calculation of the vertical and lateral extent, according to (Hoffmans and Verheij, 1997). The minimum layer thickness is usually considered 2 times the d_{50} of the rock armour, but often a greater thickness is advantageous. Moreover, the lateral extent of the rock armour protection layer can be considered to be between 2.5 and 4 times the diameter of the pile.

Table 2.5: Stone size and thickness scour protection (own research)

Location	d_{50} filter (m)	Thickness filter (m)	d_{50} armour (m)	Thickness armour (m)
Egmond aan Zee	0.05	0.4	0.4	1.4
Horns Rev	0.10	0.5	0.40	1.0
Thornton Bank	0.05	0.6	0.35	0.7
Coastal Virginia	0.17	1.0	0.45	0.9
Veja Mate	0.01	0.5	0.19	0.5
Gode Wind	-	-	0.13	1.1

Furthermore, Table 2.6 gives an indication of the most common engineering properties of fragmented igneous rock which can be later used to decides on the input constants in the DEM simulations. The values are chosen as the average values for the properties of a fragmented granite rock, which is generally used for offshore scour protection armour rock.

Table 2.6: Engineering properties of granite (fragmented rock) (own research,
consulted the work of Bosscher et al. (1988) and Zhu (2016))

Property	Notation	Range
Internal friction angle (^{o})	ϕ	30-35
Coefficient of static friction (-)	μ_s	0.5-0.8
Interface friction with steel (-)	$tan(\delta)$	≈ 0.43
Density (kg/m^3)	ρ	2650-2750
(Bulk) Porosity (%)	n	10-40
Young's Modulus (GPa)	E	10-70
Shear Modulus (GPa)	G	10-50
Poisson's ratio (-)	ν	0.2-0.3
Hydraulic conductivity (cm/s)	k	0.5-1

2.2.3. Final remarks

As conclusions for the scour protection and the rock armour sections, one can emphasise the need to design a static protection mechanism such that the scour effects at the base of the monopiles can be effectively minimised. Moreover, the rock which stabilizes the soil is very important, from its lateral and vertical expend to its general properties. In particular, the mean rock size d_{50}, the gradation and other engineering properties are the most definitive in order to ensure that the design uses the most suitable choice of material for each case scenario.

Therefore, there is a clear dependency between the structural and geotechnical design of the monopile and the characteristics of the rock armour layer. A certain diameter of the monopile implies a certain extent of the scour hole, which can be filled with filter and rock armour such that it increases the stability of the pile. Depending on the marine conditions, availability of nearby material and certain design standards, a choice on the type of material used for the scour protection layer needs to be made. Thus, this research will focus on this interdependence and will consider the relation between the design characteristics of the monopile and the properties of the rock armour layer.

2.3. Discrete Element Modelling theory

2.3.1. Introduction DEM

Numerical models can provide recommendations for design and operation of rock engineering structures where there is a high degree of uncertainty, as well as provide a deeper insight into the fundamental behaviour of the rock masses (Jing and Stephansson, 2007). Moreover, numerical modelling shows more flexibility in the variety of applications than analytical method. Furthermore, in comparison to physical modelling, the data from numerical models can be accessed at any stage of the test (Cundall and Strack, 1979).

There are two main modelling approaches used to simulate particulate systems: continuum (making use of the Eulerian framework: coordinate system are fixed in space) and discrete (using Lagrangian description, where special coordinates are fixed in material). The most common method currently used is the continuum approach which describes the behaviour of the granular material based on constitutive laws. Mechanical variables such as stress and strains are calculated using differential equations which are then solved numerically using, for instance, Finite Element Method (FEM) or Material Point Method (MPM). Both FEM and MPM use complex constitutive laws and consider the soil to be a continuous material, without investigating the relative movements and rotations of each particle inside the material (O'Sullivan, 2011b).

Discrete Element Modelling (DEM), on the other hand, uses the Lagrangian approach by considering individual particles and their interactions which have a direct influence on the macroscopic behaviour of

the material. DEM has several advantages over continuum approaches, since it uses simpler numerical models for contacts between particles and it can represent very precise particle geometries, allowing for a very realistic representation of the overall behaviour of the material. In particular for geo-engineering applications, there are several benefits of using DEM as suggested by O'Sullivan (2011b). First and foremost, using DEM it is possible to measure the evolution of contact forces, particle and contact orientations in order to predict a more accurate response of the material. DEM allows to look inside the material behaviour, in contrast to laboratory and field test which allow only for an inspection of overall material behaviour. Secondly, DEM allows for large displacements problems for which the FEM shows limitations. It can thus simulate penetration movements, failure of soils associated with large deformations and other specific problems which cannot be simulated using the continuum approach, such as internal erosion, scour and sand production in oil reservoirs (O'Sullivan, 2011b).

The topic of this thesis involves the penetration of an object in a discrete medium. It is considered a viable solution to use a discrete method to simulate the individual rock fragments forming the scour protection. Full scale testing is difficult to carry out due to the large size of the rock armour. Moreover, stone armour is a quarried rock, thus it comes with certain heterogeneity with respect to its grain shape, size distribution and roughness, aspects which can be incorporated to some extent in the DEM model. Lastly, DEM is ideal to simulate installation aspects of pile driving, aspects which cannot be fully captured using a continuum approach.

2.3.2. DEM theoretical background

Overview DEM procedure

One of the first to introduce the concept of a Discrete Element Model is Alder and Wainwright (1957). Their code focused on solving classical equations of motion of molecular particles. Later, Cundall and Strack (1979) laid the basis of the discrete element model (also known as distinct element method), and for this reason, they are often referred to as the founders of DEM for analysis of rock mechanics problems. In essence, the problem involves a transient interaction of particles with equilibrium developing when there is a balance in their internal forces. The main purpose of discrete method is to model the particles (microscopic level) to compute the bulk behaviour of the material (the macroscopic level).

Discrete element method has gained popularity over the years in the area of geomechanics due to its large applicability to certain scenarios where traditional FEM cannot express the bulk behaviour of the materials. Figure 2.5 shows an overview on the sequence of calculations steps in a general DEM algorithm, which can be described as follows:
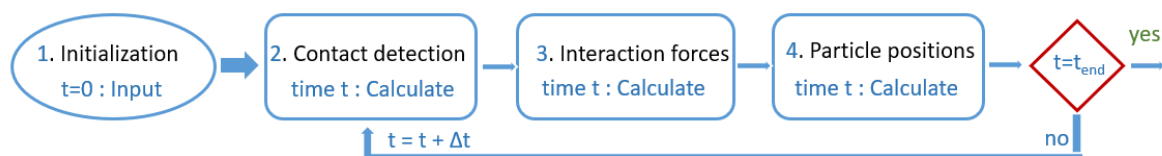
Figure 2.5: Flowchart with the calculation steps in a DEM algorithm

1. Initiation refers to creating of particles, geometries, boundaries and time-step. In particular, the particle properties are to be defined, as well as their initial positions, velocities and accelerations. The environment is also created and the properties of the geometry are inputted, as well as the interactions in the model are defined through the use of a contact model.

2. At each time-step, contacts are identified using a detection algorithm. A time consuming method is to direct check of every particle, however faster methods can be used such as Verlet neighbour lists (which uses a cut-off distance) or space based search (which uses a cell size and distance between particles).

3. The inter-particle forces are then calculated based on the overlap of the soft particles. Both body and external forces are included in the expression of the contact forces.

4. Using the interaction forces, the resulting force and toque acting on each particle can be determined. Each particle has 6 degrees of freedom in 3D, thus can experience two types of motion: translational and rotational. The dynamic equilibrium of a particle involves two sets of equations which are then calculated according to Newton's law of motion. The resultant applied force (gravitational contact and non-contact) determines the translational movement, while the resultant applied moment is used to calculate the rotational motion. The accelerations are then numerically integrated over a time step (using for instance central difference) to update the particle velocities and positions. At the next time step, the newly determined positions and orientation will be used, and the calculations can be repeated if the current time has not reached the end time of the simulation.

Characteristics DEM models

Numerous assumptions are used in DEM, as indicated by O'Sullivan (2011b). For the purpose of outlying how DEM works, the key assumptions are briefly described here. The particles are rigid, can move and rotate independently. The program automatically identifies new contacts over an infinitesimal area, allowing the particles to overlap. For this reason, the method is called soft-sphere, and it can be visualised in Figure 2.6. Compressive forces can then be calculated from the overlap, and at the contact points, normal and tangential forces are determined. When the tensile force exceeds a maximum, then the particles move away from each other.
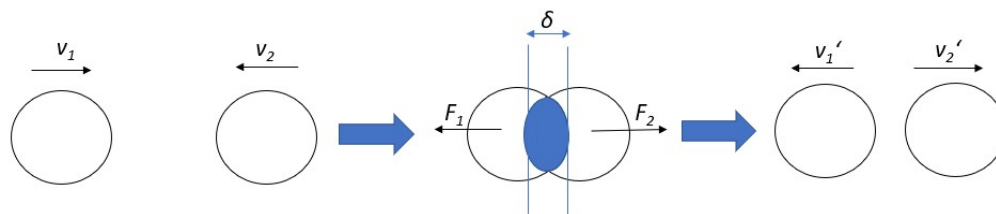
Figure 2.6: Soft-sphere contact between two particles

DEM simulations can be computationally expensive if the number and complexity of the particles is very large. The timestep should be as large as possible to decrease the calculation time, however small enough to justify the assumption of constant acceleration within each time step and to ensure stability of the calculations. If the timestep is too large, accuracy decreases and erratic behaviour might occur as the overlap is too large which leads to very large forces and velocities.

One way to determine the time step is to use the Rayleigh timestep method, which is defined as the time for a shear wave to propagate through a solid particle. The theoretical maximum timestep (T_r) where the coordination number (total number of contacts per particle) is larger than one is as indicated in Equation 2.7. The time step is directly dependent on the size of certain parameters. It is directly proportional to the particle size, and inverse proportional to the shear modulus. One way to increase the time step would then be to reduce the number of very small particles and use a shear modulus which is relatively small. Moreover, in practice, for quasi-static systems, some fraction of this maximum value is used. For high coordination numbers a typical time step of $0.2T_R$ (20%) is appropriate, while for lower coordination numbers, $0.4T_R$ (40%) is suitable.

$$T_r = \frac{\pi R_{min}\sqrt{\frac{\rho}{G}}}{0.1631\nu + 0.8766} \tag{2.7}$$

where:

T_r = Theoretical maximum time step (s) ρ = Density particle (kg/m^3)
R_{min} = Smallest particle radius (m) v = Poisson's ratio (-)
G = Shear modulus (Pa)

Contact models

Complex contact models include certain characteristics such as wear, cohesion and bonding or aim to incorporate elasto-plasticity for compressible bulk material. For the application of this thesis, a more simple and computational efficient contact model is used. Hertz-Mindlin contact model uses a non-linear spring dashpot and it is generally used for accurate and efficient force calculation in a dry bulk material. Using a simple elastic contact no residual overlap results after unloading, which is a good approximation when considering the collision of dry cohesionless particles. In addition, it is well known that the behaviour of rocks is rather nonlinear since when a load is applied to a rock, a non-linear behaviour between the stress and the strain can be observed.

The Hertz-Mindlin contact model has a normal force component F_n based on Herzinian theory and a tangential force component F_t based on Mindlin-Deresiewicz theory (see Figure 2.7). Refer to Table 2.7 for the full equations of these force components. Both normal and tangential forces have damping components where the damping coefficients C_n and C_t are related to the coefficient of restitution e. The tangential friction force needs to obey the Coulomb's law of friction using the friction coefficient μ_s. In addition, rolling friction can be accounted for by applying a torque to the contacting surfaces τ, which uses the coefficient of rolling friction μ_r.

Among limitations of the contact model, a maximum 4% overlap allowed for the soft spheres which suggests the importance of the time step since it has direct influence on the stability of the model. If the stiffness and damping coefficient are changed, then this has a direct influence on the contact forces and distance travelled by particles. If the relative velocities between the particles increase, then the contact overlap and damping also change accordingly.

DEM offers the possibility to choose the particle shape, as it will be tackled later in Section 2.4.2. A common way to take into account the irregular shape of the particle (for instance polyhedrons) in the calculation of the contact forces is to apply the approach first introduced by Nassauer and Kuna (2013). The method considers a new effective radius calculated as $R_{NK} = \frac{V_{over}}{\pi * \delta_n^2}$, where V_{over} is the overlapping volume. This radius can be then used to calculate the equivalent radius of particle R' and then inserted in the formula of the normal force F_n, but needs to be corrected by a factor, as shown in the formula 2.8 (EDEM, 2021b).

$$F_n = \frac{0.62}{0.752} \frac{4}{3} E' \sqrt{R_{NK}} \delta_n^{3/2} \tag{2.8}$$
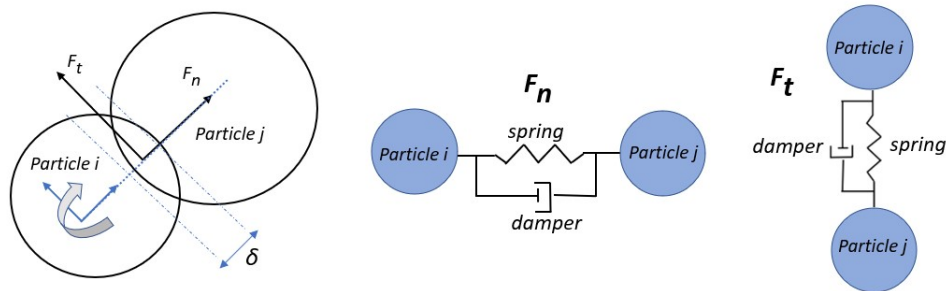
Figure 2.7: Contact forces between two particles

Table 2.7: Equations used for the Hertz-Mindlin contact model, as indicated by EDEM (2018)

Equation	Conditions
$$F_n = -\frac{4}{3}E'\sqrt{R'}\delta_n^{3/2} + C_n\vec{v_n^{rel}}$$ (2.9)	F_n = Normal force (N) E' = Equivalent Young's modulus (Pa) (calculated using Equation 2.17) R' = Equivalent radius particle (m) (calculated using Equation 2.18) C_n = Normal damping coefficient $(N \cdot kg/m)^{1/2}$ (calculated using Equation 2.12) δ_n = Normal overlap (m) $\vec{v_n^{rel}}$ = Normal relative velocity (m/s)
$$F_t = min(S_t\delta_t + C_t\vec{v_t^{rel}}, \mu_s F_n)$$ (2.10)	F_t = Tangential force (N) S_t = Tangential stiffness (Pa) (calculated using Equation 2.16) C_t = Tangential damping coefficient $(N \cdot kg/m)^{1/2}$ δ_t = Tangential overlap (m) μ_s = Coefficient of static friction (-) $\vec{v_n^{rel}}$ = Tangential relative velocity (m/s)
$$\tau_i = -\mu_r F_n R_i \omega_i$$ (2.11)	τ = Torque $(N \cdot m)$ μ_r = Coefficient of rolling friction (-) R_i = Distance contact point to center of mass (m) ω_i = Unit angular velocity (m/s)
$$C_n = -2\sqrt{\frac{5}{6}}\beta\sqrt{S_n m'}$$ (2.12)	S_n = Normal stiffness (Pa) (calculating using Equation 2.15) β = Coefficient (-) (calculated using Equation 2.14) m' = Equivalent mass (kg) (calculated using Equation 2.19)
$$C_t = -2\sqrt{\frac{5}{6}}\beta\sqrt{S_t m'}$$ (2.13)	S_t = Tangential stiffness (Pa) (calculated using Equation 2.16)
$$\beta = \frac{\ln e}{\sqrt{\ln^2 e + \pi^2}}$$ (2.14)	e = Coefficient of restitution (-)
$$S_n = 2E'\sqrt{R'\delta_n}$$ (2.15)	See conditions Equation 2.9
$$S_t = 8G'\sqrt{R'\delta_n}$$ (2.16)	G'= Equivalent shear modulus (Pa)
$$\frac{1}{E'} = \frac{1-v_i^2}{E_i} + \frac{1-v_j^2}{E_j}$$ (2.17)	$E_{i,j}$ = Young's Modulus of each particle (Pa) $v_{i,j}$ = Poisson's Ratio of each particle (-)
$$\frac{1}{R'} = \frac{1}{R_i} + \frac{1}{R_j}$$ (2.18)	$R_{i,j}$ = Radius each particle (m)
$$m' = (\frac{1}{m_i} + \frac{1}{m_j})^{-1}$$ (2.19)	m_i, j = Mass each particle (kg)

Moreover, for non-spherical particles, rolling resistance is less important and spinning friction becomes relevant. Spinning friction applies when a particle face is rotating against another particle or geometry (EDEM, 2021b). An effective disk radius $R_{disk} = \sqrt{\frac{A_{over}}{\pi}}$ is calculated by approximating the contact as a disk with area equal to the normal overlap area A_{over}. Then, the torque on the particles is determined using formula in Equation 2.20 which acts in the opposite direction to the normal part of the relative angular velocity. A limiting torque is considered in order to avoid oscillating behaviour when the angular velocity is small (refer to the documentation provided by EDEM (2021b) for further details of how to find the torque which eliminates the angular velocity in each timestep).

$$\tau = \frac{2}{3}\mu_s F_n R_{disk} \tag{2.20}$$

2.4. Literature review of relevant papers

This section describes how previous researches have used DEM to construct a penetration test model. For this, key references overview with previous research done on the topic is included in Section 2.4.1. Moreover, Section 2.4.2 identifies papers which investigated the effect of creating more complex shapes for the DEM input particle shapes.

2.4.1. Key references concerning DEM penetration test models

Overview past-research

One of the research methods of this thesis is to construct a DEM model which consists of a penetrating object in a granular material. For this purpose, Table 2.8 was gathered in order to highlight the extent of research already done of the subject. The inventorisation was done with the focus on granular, cohesionless materials, such that only materials with similar behaviour to those used in the application of this thesis are considered. As it was shown in Section 2.1.2, axial capacity of piles is highly dependent on the soil characteristics, thus DEM simulations using materials exhibiting cohesion or bonding are left out of the overview. Several key aspects are highlighted in Table 2.8 and each column is discussed separately:

- 2rd **column**: It can be seen that almost all of the researchers considered a ratio of the mean size of the particles d_{50} to the width of the penetrating tool w to below unity. The only exception is Breul et al. (2009) which considered ballast rocks of larger diameter.

- 3rd **column**: The number of particles represents the maximum number of spheres and disks involved in each simulation and it can be seen that it can vary between thousands and millions. The particle number chosen by each author depends on the purpose of its research, but also on the capabilities of the computers at the time of each research. Thus, researchers searched for ways to cut down on the computation cost of the DEM and used certain techniques. For instance, Lin and Wu (2012) and McDowell et al. (2012) considered only a fraction of the 3D simulated space, thus reducing the number of required simulated spheres. Others such as Huang et al. (1992), Jiang et al. (2006), Shoda et al. (2009), Falagush et al. (2015) and Liu and Wang (2016) simulated only the half-space for a 2D simulation, taking advantage of the symmetry of the model.

- 4rd **column**: Numerous researches have investigated how far the bottom boundary should be such that little to no wall effects are captured in their DEM models. Although it is common practice that this bottom boundary is expressed in terms of the width of the penetrating tool, for the purpose of this research, it is considered more convenient to compare the ratios between the vertical domain and the maximum penetration depth (H/z).

- 5rd **column**: This column indicates the spatial domain used by the majority of researchers. It can be seen that the boundary needs to be at minimum 5 times the diameter of the penetrating

object w, but in general, researchers used a factor of 10 or 20 in order to ensure that there is no contribution of the wall effects on the penetration resistance.

- 6rd **column**: Hertz-Mindlin contact model was defined in subsection 2.3.2, Moreover, the choice of a (non-linear) elastic model was made by other researchers investigating the topic of penetration tests. The conclusion is that a relatively simple and computationally inexpensive model is considered applicable to describe the interaction between the particles and between the particle and the penetrating object, without requiring any additional, more complex contact models.

Table 2.8: Overview past papers concerning DEM simulations of a penetrating object through granular material

Author	d_{50}/w	Particle no.[b]	H/z	Domain[c]/w	Contact	Software
Huang et al. (1992)	0.08	12,000*	2.4	16.0	Linear	in-house (2D)
Tanaka et al. (2000)	≈0.10	944	1.8	30.0	Linear	in-house (2D)
Lobo-Guerrero et al. (2005)	0.20	6,500	2.0	13.3	NS[a]	PFC2D
Chung and Ooi (2006)	0.40	4,608	5.0	5.8	Hertz-Mindlin	PFC3D & EDEM
Jiang et al. (2006)	0.08	10,000*	1.2	17.5	NS[a]	in-house (2D)
Breul et al. (2009)	≈0.35	2,200	1.1	27.6	NS[a]	in-house(3D)
Butlanska et al. (2009)	0.37	60,000	1.4	16.8	NS[a]	PFC3D
Shoda et al. (2009)	0.10	10,000*	2.0	10.0	NS[a]	in-house(2D)
Butlanska et al. (2010a)	0.05-0.16	65,000	1.4	5.6-33.7	Elasto-plastic	PFC3D
Jin and Zhou (2010)	0.60	NS[a]	1.6	7.1	NS[a]	PFC3D
Arroyo et al. (2011)	0.24-1.6	65,000	1.4	16.8	Elasto-plastic	PFC3D
Lin and Wu (2012)	0.09-0.34	422,191*	1.5	10.0-40.0	Hertz-Mindlin	PFC3D
McDowell et al. (2012)	0.11	46,800*	1.0	33.3	Linear-elastic	PFC3D
Tran et al. (2013)	NS[a]	5,000	1.3	NS[a]	Linear-elastic	PFC3D
Zhang and Wang (2014)	0.17	608,088	2.0	12.0	Hertz-Mindlin	in-house(3D)
Falagush et al. (2015)	0.05	37,050*	1.0	16.6	Linear-elastic	PFC2D
Liu and Wang (2016)	0.05-0.11	696,649*	1.3	30.0-60.0	Linear	PFC2D
Duan et al. (2018)	0.13	10,080	2.2	26.6	Linear	PFC2D
Esposito et al. (2018)	0.12	114,036	2.1	10.0	Elasto-plastic	PFC2D
Ciantia et al. (2019)	0.02	442,335	1.1	12.0	Hertz-Mindlin	PFC3D
Feng et al. (2019)	0.06	460,000	4.0	6.6	Hertz-Mindlin	in-house(3D)
Li et al. (2019)	0.07	175,310	1.9	80.0	Linear	PFC 2D
Miyai et al. (2019)	0.01-0.38	35,500,000	6.0	24.8	Linear	in-house(3D)
Shi et al. (2019)	0.13	NS[a]	2.0	40.0	NS[a]	PFC3D
Zhao et al. (2019)	NS[a]	NS[a]	≈5.2	NS[a]	Linear	PFC3D
Gezgin et al. (2020)	0.25-0.33	111,624	1.5-3.0	16.7	Hertz-Mindlin	EDEM
Macaro et al. (2021)	0.03-0.06	36,961	16.0	5.0	Hertz-Mindlin	YADE (3D)

* Only a fraction of the domain is considered
[a] NS - Not Specified
[b] Particle no. - Maximum number of disks/spheres
[c] Domain - Full lateral extent (penetrating object in the middle)

- 7rd **column**: Numerous software are currently available to use for DEM simulations. One can identify that PFC by Itasca is one of the most common software (see the last column of Table 2.8) which uses a code closely linked to Trubal (first developed by Cundall and Strack (1979). However EDEM by Altair, Rocky by ESSS and the recently launched (2019), Geo-Wise by University of Ghent, are gaining popularity as commercial software. Open-source software such as Mercury-DPM by University of Twente, LIGGGHTS by Johannes Kepler University, YADE by Grenoble University, BLOCKS3D by University of Illinois and ESyS Particle by University of Queensland are general purpose DEM software (refer to Figure 2.8). However, most of the open-source software require a significant amount of coding and they lack the friendly user interface of commercial software. In addition, the open-source software have several drawbacks such as compatibility issues, limited maintenance and development as well as an increased security risk.

Therefore, due to the time constrains imposed by this thesis, the commercial software, EDEM, was chosen to be the most reliable and easy to use DEM software, which is able to model the desired scenario. EDEM has recently been acquired by Altair Engineering (previously owned by DEM Solutions) and over the past years, it has shown some promising advancements, however few researches have

investigated the capabilities of EDEM with respect to the topic of this thesis. Chung and Ooi (2006) used a beta version of the software and then, 10 years later, Gezgin et al. (2020) constructed a model which simulates the penetration process using a sensitivity analysis. Gezgin et al. (2020) showed that EDEM is a great tool to investigate penetration resistance, thus this thesis will continue the investigation on the applicability of the EDEM software for the concerned topic.
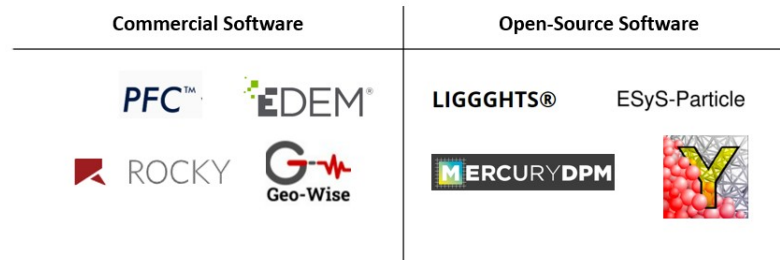
Figure 2.8: The most common software for DEM

Classification of DEM models of penetration tests

Research in the area of DEM geomechanics can be classified according to their purpose: calibration of DEM model; validation of DEM models; comparison between micro-scale and bulk material behaviour; simulations of laboratory tests; simulations of field-scale problems (O'Sullivan, 2011a). In particular, numerous papers have been published for the application of DEM to simulate physical systems, at element scale. O'Sullivan (2011a) indicated key reference for typical geotechnical laboratory tests such as triaxial, biaxial, plain strain, direct shear, simple shear, interface shear tests, but also identified other categories for DEM geomechanics such as machine-soil interaction and penetration models.

Several area of interest have been considered with respect to penetration mechanisms using various DEM software. The moving objects exhibit a certain resistance to penetration which aim to replicate the penetration of:

- penetrometers: Jin and Zhou (2010), Lin and Wu (2012)

- CPTs: Jiang et al. (2006), Arroyo et al. (2011) ,Tran et al. (2013), Butlanska et al. (2014), Janda and Ooi (2016)

- Pandas: Breul et al. (2009)

- closed cylinders: Chung and Ooi (2006), Feng et al. (2019),

- spheres: Peng et al. (2009), Macaro et al. (2021)

- piles: Shoda et al. (2009), Duan et al. (2018), Li et al. (2019), Shi et al. (2019), Gezgin et al. (2020)

Moreover, some of the studies mentioned in Table 2.8 considered crushing as an important aspect to be included in the DEM model (Lobo-Guerrero and Vallejo (2005), Falagush et al. (2015), Liu and Wang (2016), Ciantia et al. (2019)). Others, aimed to see the effect of plugging during penetration of simulated piles (Li et al., 2019). A couple of the researches increased the gravitational acceleration, for instance Bolton et al. (1999) by a factor 4, 7 and 12.5, Jiang et al. (2014) by a factor 2, Duan et al. (2018) by a factor 10. There is also an interest in coupling DEM with FEM in order to efficiently reduce the amount of particle used as showed by Jin and Zhou (2010), who used an interface between the two domains as velocity boundary.

Numerous researches from Table 2.8 have constructed models with particle composed on single spheres (3D) and single disks (2D). However, there are some authors that investigated the shape effect on the

penetration resistance such as Chung and Ooi (2006) (4 overlapping spheres), McDowell et al. (2012) (2 spheres), Tran et al. (2013) (cylinders), Falagush et al. (2015) (2 spheres) Liu and Wang (2016) (24 disks), Feng et al. (2019) (1, 2 and 3 spheres) and Gezgin et al. (2020) (1 and 2 spheres). Others have inhibited the rotation of sphere to mimic the effect of angularity and non-sphericity, crucial to obtain a more realistic behaviour of the particles (Butlanska et al. (2010b), Arroyo et al. (2011), Butlanska et al. (2014), Falagush et al. (2015), Esposito et al. (2018) and Gezgin et al. (2020)).

Chronological evolution: state-of-the-art penetration test DEM model research
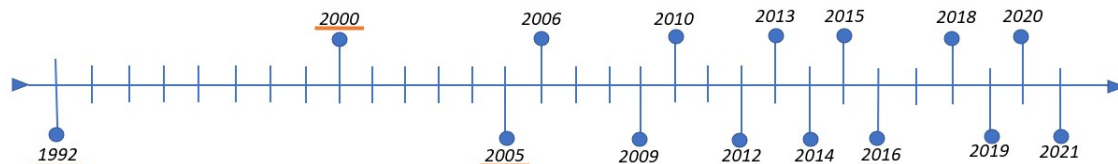
One of the first to use microscopic concepts for the interpretation of cone penetration was Huang et al. (1992), who identified the development of large strains in the vicinity of the penetrometer. Contact stresses around the tip of the cone increase (which can be explained by an eventual crushing of the particles) and reduce sharply behind the cone tip. Later, Tanaka et al. (2000) tackled problems such as stability of the DEM simulations and conducted a sensitivity analysis for the coefficient of friction between the pile and the particles. Among the results of the paper, it is shown that with an increase in the coefficient of friction, heave appears at the surface. The study also recommends investigation of interlocking effects in the mechanical model. Lobo-Guerrero and Vallejo (2005) is among the first to consider crushing around driven piles using a simplified tensile criterion. Using crushable material, the contact forces do not concentrate at the tip and the crushed particles migrate upward along the shaft. Thus, the authors include breakage in their model which allows for particle rearrangement, stress relaxation and lower resistance at driving.
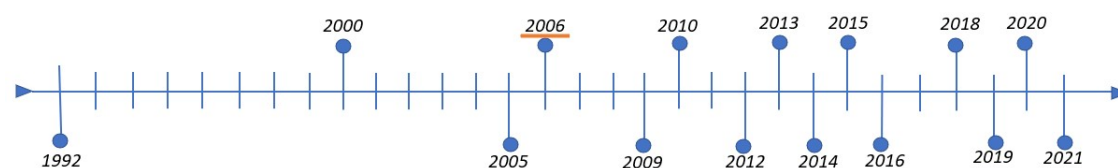
Another research team that investigated the response of CPT penetration in granular soil is Jiang et al. (2006). They investigated tip resistance, displacement paths, velocity vector distributions, stress fields and stress paths. Among the conclusions of the paper, the tip resistance increases with depth, however it reaches a constant at certain depth. During penetration, the soil near penetrometer moves downward and then upward and sideways. Maximum velocity occurs near the tip, but in the case of perfectly smooth interface, the location changes to the shoulder of the penetrometer. Furthermore, Chung and Ooi (2006) uses a calibration procedure to verify if the DEM model is able to give a quantitative prediction rather than qualitative representation of the behaviour of solids. Experimental tests to calibrate certain coefficients were undertaken, such as laser scanning for the curvature at contact, sliding tests for static friction, drop test for restitution coefficient. For spherical particles, it is shown that the macroscopic friction is smaller than the inter-particle microscopic friction coefficient. The sensitivity analysis showed that when the shear modulus is reduced (by a factor 1000) for non-spherical particles, then no significant difference in penetration resistance can be noticed.
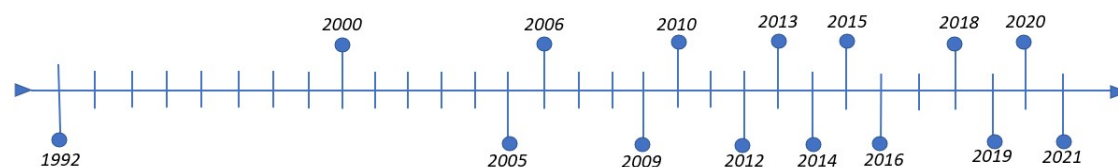
In addition, Breul et al. (2009) is one of the few researchers which investigate a coarse material (a ballast of basaltic origin with average d_{50} of the rock between 25 and 50 mm) for a penetration test.

The authors propose a logarithmic relation between the density and the penetration energy, which is tested on the experimental and DEM data sets and conclude that the simulated penetration energy is smaller than those coming from experiments on the same type of material.

Computational efficiency was a key topic in the research of Butlanska et al. (2009), who considered the aspect of symmetry in the cylindrical domain by taking a full, a half and a quarter model, thus the different number of particles in each. Symmetry is shown using the quarter chamber by looking at the porosity, which is higher in their vicinity of the wall and increases during cone penetration. This symmetry induces a bias towards higher cone resistance, but overall, the tip resistance from the simulation is in accordance with that from experimental results.
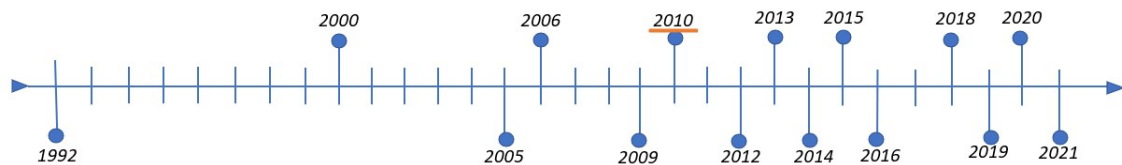
Later, Butlanska et al. (2010b) uses the virtual calibration chamber based on the physical model to calibrate the model. Trial and error for inter-particle friction, stiffness and damping parameters is conducted in order to provide best fit for a drained triaxial test result. The result of the study show that by decreasing the ratio of the mean grain size to the cone diameter, then the cone resistance curve is smoother. An exponential function is fitted though the cone resistance and the results of the 3D DEM simulations show an improvement than previous 2D simulation, where the comparison with the experimental data was only qualitative and not quantitative. In addition, a second paper of Butlanska et al. (2010a) considered various ranges for the diameter of penetrating cone and for the domain extent.
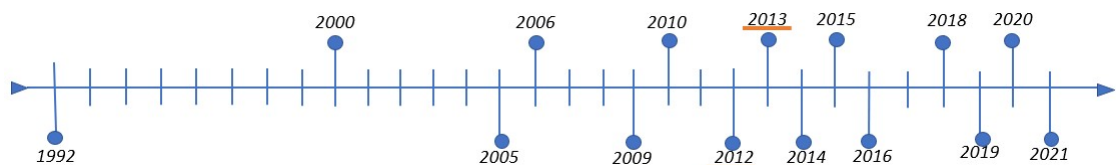
Other researchers such as Lin and Wu (2012) show that penetration resistance increases with a growth in sleeve friction and with larger penetrometer diameter. Moreover, McDowell et al. (2012) showed that it is better to use a refinement strategy in which smaller particles are used near the tip so that there are enough contacts between particle and cone tip. In this way, the cone resistance was found to be the same order of magnitude and shape as the experimental data. Tran et al. (2013) considered the case of dynamic loading using impact energy instead of a constant velocity rod penetrating granular medium. The sample is constructed using different particle arrangements, thus the authors construct a probability density function of the tip resistance at each simulation. Then, a correlation between the static and the dynamic conditions was created and an agreement between the two trend line is found. By looking at the volumetric strain, sample expansion during dynamic loading was found.
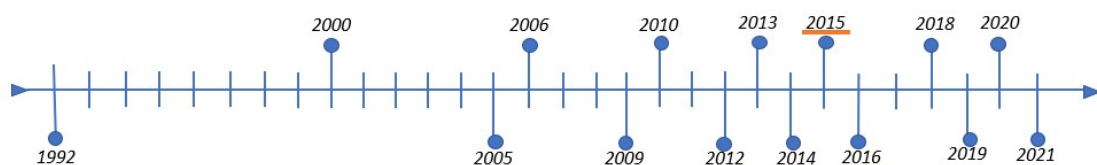
A 3D DEM simulation is developed by Zhang and Wang (2014) which aims to correlate the DEM results with that from centrifuge pile tests and shows that modelled base resistance resembles the experimental data. The downwards motion of the particles change into a diagonally movement towards the tip of the cone, phenomena which is indicated also by the chain force network which indicated shearing of the material due to the rotation of principal stresses. A 2D model is constructed by Falagush et al. (2015) who investigated both shape and crushing of particles. Particle rotation was inhibited which resulted in an increase in tip resistance. Particle crushing showed that the resistance decrease when allowing

for crushing, while the confining stress increased. Also Liu and Wang (2016) considers crushing of particles using a parallel bond breakage model for the disk agglomerates. The simulation is calibrated using a biaxial test, which is then used for the penetration tests. Tip resistance, horizontal and vertical stresses are recorded and shear stress contours are successfully constructed.

2000   2006   2010   2013 2015   2018 2020
1992   2005   2009   2012 2014 2016   2019 2021
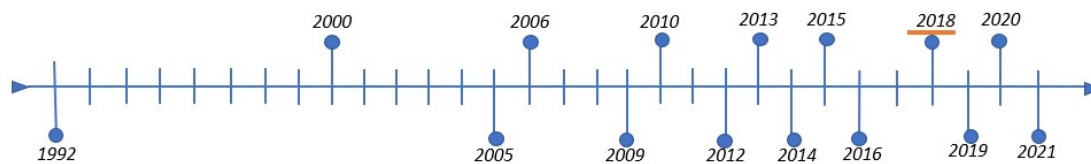
Esposito et al. (2018) creates an extensive review of the available papers on DEM simulations involving penetration mechanisms. It is the starting point for Table 2.8 constructed in this thesis. The paper of Esposito et al. (2018) identifies the three main types of sample generation process, radius expansion, sample compaction and small sample reproduction, however concludes that the difference between them is negligible. A reference model is created and a sensitivity analysis is performed to check for particle rotation, pile velocity, lateral boundary, sample generation, particle size, pile friction and pile installation method. The simulations aimed to give an indication of several parameters such as tip resistance and skin friction, horizontal stress state and porosity variations, contact orientation and displacement patterns. Among the conclusions of the paper, inhibiting rotation is not the best approach for pile penetration mechanisms since it does not influence the skin friction and creates disturbance in the sample.

2000   2006   2010   2013 2015   2018 2020
1992   2005   2009   2012 2014 2016   2019 2021
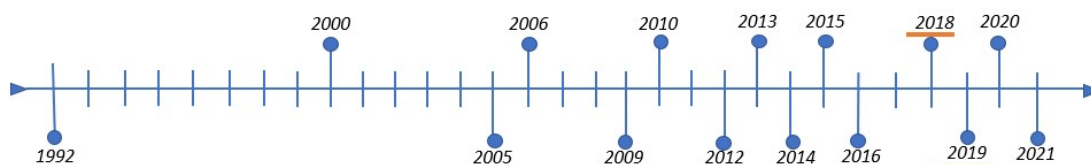
An example of a high gravitational force is used in the model of Duan et al. (2018) for both driven and bored piles. Driven piles do not show settlement at the beginning of the penetration due to their available base capacity. The conclusion of the paper showed that the surrounding region experiences high lateral stresses and that the ultimate unit shaft resistance of driven pile is larger than for bored piles due to the appearance of friction fatigue and residual forces. In addition, the paper of Feng et al. (2019) considers cylindrical objects penetrating in granular medium both in a numerical and an experimental manner. Force-depth relation is divided in three zones: compression, developing stagnant zone and fully developed zone. Sensitivity analysis is made on the packing, sliding friction, rolling friction, shear modulus, grain sizes and grain aspect ratio. The general behaviour is consistent with the experimental data, except when the spheres show no friction as no stagnant zone is observed.

2000   2006   2010   2013 2015   2018 2020
1992   2005   2009   2012 2014 2016   2019 2021
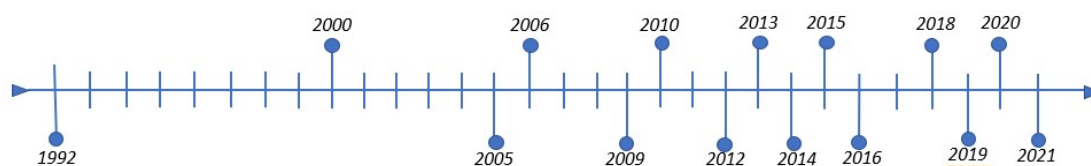
Shi et al. (2019) constructed DEM simulations for screw piles which uses a particle refinement method, first introduced by McDowell et al. (2012) and three zones: core, transition and boundary, each with different PSDs. Measurement spheres of different sizes were used for void ratios and soil stresses calculation. The model uses a scaling rule for optimization of contact stiffness parameters, which is then validated using triaxial tests. The scaling law involves an elastic behaviour parameters which can be kept the same, and just the particle contact and d_{50} of the rocks should be scaled by a factor. The conclusion of the paper is as follows: the higher the drilling velocity ratio, the lower the driving force and torque due to an increase of downward force as a consequence of change in movement of particles. Zhao et al. (2019) used also a particle refinement method (here it is called hierarchical model) with parameters calibrated using triaxial testing to test a penetration model with the pile and a cap.

Miyai et al. (2019) comes with a relevant paper for the topic of this thesis. They consider the influence of particle size on the penetration mechanism of a plate in a dense granular medium. The authors use a quasi-2D model and keep the thickness of the plate constant but vary the size of the particle, simulating ratios d_{50}/w between 0.02 and 0.38. The initial packing was kept constant and among the findings of this research, tip penetration resistance grows linearly with increasing the d_{50}/w ratio, while tangential forces rise with the penetration depth squared, independent of the same ratio. The authors also investigated the wedge-shaped flow formed in front of the plate tip which corresponded to the evolution of shear band formation. The paper also concludes that for a small ratio, no wedge-flow are formed and no shear bands can be identified.

Relevant for the topic of this thesis, the research of Li et al. (2019) considered open ended pile in their 2D simulation as two rectangular walls with the purpose to investigate the plugging effect between the two walls. With increasing penetration depth, soil mass flows inside with a lower rate. Considering contact force chain and principal stress direction, the particle rearrange in an arch shape, thus the authors proposed a improved arch model for the plugging behaviour. Another breakage criterion applied to elasto-brittle spheres was used in the research of Ciantia et al. (2019). It is shown that the average stresses below the pile tip increase and decline very fast as the pile penetrate further. Stress paths were depicted using DEM and arching of the soil was accentuated by grain crushing.
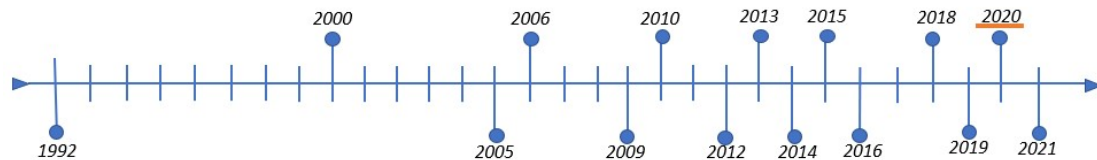
Gezgin et al. (2020) constructed a sensitivity analysis to calibrate the most significant parameters needed for simulation of a penetration steel bar in granular material. The authors investigated the effect of particle stiffness, void ratio, inter-particle static friction, particle size, particle size distribution, particle shape and rolling friction, in this order. The paper described a dynamic air pluviation generation of particles, which leads to higher coordination number when using a low friction coefficient. Other conclusions of the paper are that using larger particles, higher resistance to penetration is created and having wider PSD shows lower resistance, but increases the computational time. Higher aspect ratio and larger rolling friction makes it harder for the pile to penetrate. Moreover, it is also concluded that restraining rolling, does not give the same effect as using non-spherical particles.

Although not considering directly a DEM method, a very relevant paper is that of Bolton et al. (1999), who constructed experiments of penetration of CPTs in the centrifuge. Laboratory experiments used a sand with a constant mean diameter, while varying the cone diameter with ratios d_{50}/w between 0.025-0.028 which allowed to record tip resistance versus depth for different relative densities of the soil. Peng et al. (2009) also considered the depth dependence of an intruder penetrating a granular medium using an experimental method. A force is applied to intruders of certain size and shape, while keeping the diameter of the particles constant. Ratios of $d50/w$ between 0.012 and 0.025 are considered and the research proved that the increasing sub-linear penetration resistance is not a result of the sidewall support. Thus, a power-law dependence for shallow regime can be extrapolated to fit deeper penetrations.

Concluding remarks

The conclusions of this overview on the current available papers with DEM simulations on the topic of pile penetration mechanisms can be formulated as follows. Clear improvements in the accuracy and complexity of the penetration tests models constructed can be seen in the last 20 years. However, very few papers tackled the scenario of a smaller diameter penetrating object being driven in a large granular material and investigating the drivability of such object.

There is sufficient studies which investigate the movement and interaction of a penetrating object in a soil-like material, however there is no study (to the author's knowledge) which specifically aims to

simulate the industrial application of a pile penetrating the scour protection. In particular, what this research aims to do differently is to allow the d_{50}/w to be higher than unity but also to investigate the effect of more complex particle shapes. Thus, this thesis will contribute to the academic world twofold. First of all, it simulates a scenario which was never investigated before and secondly, it will expand on the knowledge of the research community by bringing another well calibrated and validated penetration DEM model.

2.4.2. Shape of particles

General notions

Shape is an essential topic when discussing the theory behind Discrete Element Modelling. Provided that computation time is oftentimes the biggest limitation for this numerical technique, shape is identified to be an important topic when representing large angular rock material. This research considered essential to create a 3D simulation (despite the computational cost) in view of a better visualisation of penetration mechanism. The third dimension allows for a better calculation for the penetration resistance, since there are more particle in contact with the bottom of the plate.

Theoretically speaking, particle shape analysis refers to 3 aspects: form, angularity/roundness and surface texture (Suhr and Six, 2020). The form involves a definition of aspect ratios such as elongation and flatness. Roundness is the opposite of angularity and defines how blunted or rounded the corners and edges of the particle are (Bullard and Garboczi, 2013). The last shape descriptor is the surface texture comes from a black/white or gray-scale pictures (Suhr and Six, 2020) and identifies small scale particle surface details. One can use several techniques to quantify the 2D aspect of the grain: shape factor, angularity factor, fractal analysis, Fourier shape descriptors (Das, 2007). In addition, 3D shape descriptors are usually determined based on spherical coordinates, but they follow the same principle of shape analysis as in 2D.

Particle shape modelling refers to how to implement the real shape of the particle in a numerical model. The most simple and most used shape of particle used in DEM is sphere (one of the first was Cundall and Strack (1979) who considered circles in 2D). Spherical particles are usually preferred due to the efficiency of contact detection, however the bulk friction becomes too low when compared to real granular material like crushed rock (Coetzee, 2016). Because of this, the alternative is to consider non-spherical particles such as ellipsoids, super-quadrics, polygons, clumps and clusters. For the visualisation of some example of these shapes previously modelled in DEM, refer to Table 2.9. A recent paper written by Guo et al. (2020) creates an overview of various papers on ballast rock, with an emphasis on calibration procedures and different particle shapes used in DEM models.

Table 2.9: Example non-spherical shapes DEM

Multi-spheres		Clumps & Clusters	Polyhedrons	Dilated polyhedrons	Potential particles
Zhang et al. (2021)	Zhou et al. (2012)	McDowell and Li (2016)	Huang and Tutumluer (2011)	Ji et al. (2017)	Ahmed et al. (2016)

Multi-sphere particles

Clumps or clusters are usually referred to as the multi-spheres since they are made of two or more spherical particles which form one rigid particle where contact forces are not generated between the particles. The difference between clumps and clusters is that clusters can crush since the spheres are bounded together by parallel bonds (Guo et al., 2020). However, there is also a combination of clump and cluster, when the spheres bonded in clump can be released from the clump, thus breaking the particle.

Multi-spheres are a common approach, and a reasonable trade-off between accuracy and computation time is made by Zhou et al. (2012). If the sole purpose is to represent more accurately the shape of the particles, then one can choose a particle composed of multiple spheres. One of the first to consider the multi-sphere method is Favier et al. (1999), who extenuate the computational speed advantage and accuracy of contact detection for (multi) spheres. Moreover, Zhang et al. (2021) create a FORTRAN code which can generate multi-spheres such that it accurately represents a polyhedron and thus a more realistic shape of the particles. Moreover, multi-spheres approach can be used to represent crushing phenomena, since a single sphere can be fragmented into multiple smaller spheres (Lobo-Guerrero et al., 2006). Multi-sphere approach was validated by Kruggel-Emden et al. (2008) who compared the collision of a single-sphere with wall with the impact of a multi-spheres with the flat surface. The authors recognise the limitations of the methods and advises towards further validations studies but in the context of larger granular assemblies.

Other authors also investigated the number of spheres which form the clump, such as Coetzee (2016) who investigated two methods of shape generation. The first and more complex approach refers to laser scanning the rock fragments and then fitting 2, 4 or 8 spheres in the irregular shape. Alternatively, the author manually created the clumps as either elongated or pyramid shape particles. The conclusions of the study reveals that 4 and 8 spheres clumps give a more accurate bulk response than the 2-clumps, however any non-spherical shape can be used to model accurately a hopper discharge. Moreover, the author reached the conclusion that the manually generated clumps performed relatively similar to the optimised clumps, making the laser scan operation less essential. Another laser scanning approach was performed by Zhang et al. (2017) who created a point cloud of various ballast samples using a laser scan, from which they constructed for each more than 100 bonded spheres configurations. However, more complex shapes constructed with multi-spheres is not necessarily needed, as the research of Laryea et al. (2014) showed. In other words, more there must be a trade-off between the number of spheres and the additional computational time, such that the bulk behaviour can be correctly simulated using a low number of spheres.

Non-spherical particles

Non-spherical particles come with two main difficulties for the DEM solver: contact detection and contact computation (Abou-Chakra et al., 2004). The polyhedron is a shape which is identifiable by its sharp edges and corners (Guo et al., 2020), thus it can be used to represent more accurately the real shape of crushed rock fragments. Polyhedrons are especially a common choice for research investigating ballast, since the crushed rock comes with high angularity, thus a more accurate representation of their shape is ac hived by using polyhedrons.

Several studies used polyhedrons to model the angular shape of ballast (Huang and Tutumluer (2011), Qian et al. (2013), Eliáš (2014), Deiros et al. (2016)) or rock fragments (Lee, 2014). Others have compared the applicability of polyhedrons in comparison with that of multi-spheres (Höhner et al., 2014), or used tetrahedral clumps with a breakable asperities to represent more realistically the ballast rock McDowell and Li (2016). Research has been identified also on optimising the contact detection algorithm between polyhedrons, such as the research of Peng and Hanley (2019), who aimed to improve the contact detection algorithm between superquadrics and polyhedrons.

It is common practise to take sample from the rocks used in the experiment and categorize them in terms of their shape, along with a sieve analysis for their size. One way to create the polyhedrons based on their real angular shape is to use Voronoi-based tessellation. An alternative to traditional polyhedrons are the dilated polyhedrons, which are constructed such that the vertices and edges of the original polyhedron become spheres with semi-spherical ends and the sharpness of the dilated polyhedron can be adjusted by changing the dilating sphere radius (Ji et al., 2017). Another alternative is a potential particle shapes which take the form of rounded convex polyhedron (Ahmed et al., 2016). Lastly, one can mention super-quadratics, such as the cubes with different edge sharpness or blockiness modelled by Soltanbeigi et al. (2017).

When comparing the multi-sphere approach versus the polyhedrons, there are several authors which

have investigated this topic. Szarf et al. (2011) looked at the 2D representation of the shape of particle and conducted an investigation into the influence of shape (polygons versus clumps) on the mechanical behaviour of the material in compression tests. They define a parameter $\alpha = \Delta R/R_1$ which allows for creation of various shapes for both polygons and clumps, as shown in Figure 2.9. Polygons exhibit large damage zones in a compression test, whereas clumps reveal shear bands, which is a direct difference between the two shapes with respect to the kinematics of the deformed sample. In addition, the research of Soltanbeigi et al. (2017) identified that after properly calibrating the numerical model (in their case they used a shear test), it is acceptable to substitute the super-quadrics for multi-spheres approach since their produced similar results for the application of the study, a silo flow simulation.
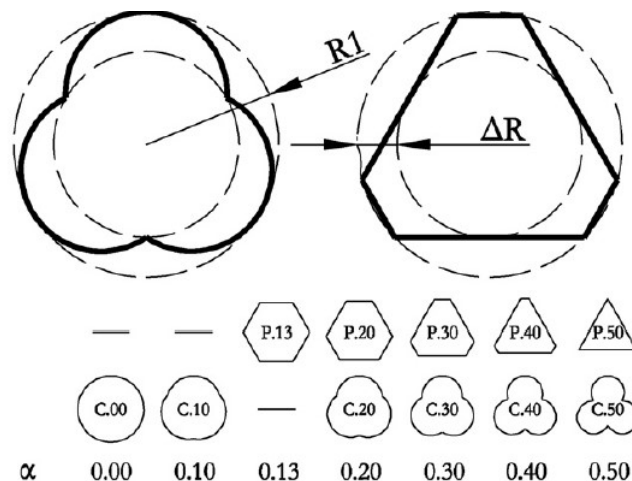
Figure 2.9: Example of particle shape construction (2D): clump and polygon (Szarf et al., 2011)

Concluding remarks

Starting with EDEM 2021, it is possible to use more complex shapes than multi-spheres to represent the shape of the particles. As it was previously described, there are numerous researches which emphasised the need to construct more complex shapes in order to capture the behaviour of the particles. For penetration test in particular, the majority of the previous research did not include a study on the shape of the particles. Considering that the case studied in this research involves large angular rock particles, it is considered beneficial to make use of the new features of EDEM and investigate the effect of different shapes on the outcome of the simulations. Therefore, the novelty of this research consists of making use of three shapes of particles, spheres, multi-spheres and polyhedrons, since to the best of the author's knowledge, the concept of polyhedrons was never applied before in a DEM simulation of a penetration test.

3

Preliminary analysis

This preliminary analysis consists of two separate sections. Section 3.1 brings an analysis of the components which need to be considered before setting up the DEM simulations of a penetration test. In other words, it describes aspects such as general calibration strategies and methods to reduce the DEM computation time. Then, Section 3.2 includes a case study on which the calibration strategy can be applied to. The chapter concludes with a discussion and subsequent conclusion on the lessons learnt from conducting this preliminary analysis in Section 3.3.

3.1. Calibration study

3.1.1. Introduction to calibration

Calibration is an important step in achieving accurate results from the DEM simulation. It involves finding a set of contact model parameters which best fits the experimental result. Thus, calibration links the micro parameters (shape of particle, PSD, coefficient of restitution, particle density, contact sliding and rolling friction coefficients, etc.) and macro-parameters (bulk density, porosity, energy dissipation, friction, stiffness etc.). Fine-scale parameters such as shape, PSD, stiffness and density are those that influence the computational time, as indicated by Equation 2.7. In more detail, Katterfeld et al. (2019) explains the influence of each of these four parameters on the bulk material:

- **Particle shape**: The particle shape influences the packing porosity of the material. The bulk friction behaviour is strongly influenced by the particle shape, for example in angle of repose or direct shear tests. The less spherical the shape is, the higher the interlocking effect and thus the higher the bulk friction.

- **Particle side distribution(PSD)**: The PSD also influences the packing porosity and hence the bulk density for a given particle density. Usually, with a wider PSDs, the porosity decreases. A reduction in the total number of particles in a given model results in a logarithmic reduction in the calculation time.

- **Particle density**: The particle density highly influences time step; the higher the particle density, the larger the time step.

- **Contact stiffness**: In the Hertz-Mindlin contact model, the contact stiffness is not only dependent on the overlap, but also on the particle size. The effect of Poisson's ratio is negligible in terms of bulk material behaviour. In general, with the Hertz-Mindlin contact model, realistic bulk flow results can often be achieved using relatively low values for elastic moduli.

There are other micro-parameters which can influence the bulk behaviour of the material. In the paper of Katterfeld et al. (2019), three other coefficients are discussed: sliding and rolling coefficients and co-efficient of restitution. The bulk friction is strongly influenced by both the sliding and rolling coefficients, which, in combination with spherical particles, can also produce accurate levels of bulk friction. Higher sliding friction values between particles lead to a less dense packing (higher porosity). In addition to the inter-particles sliding friction, the particle-wall sliding friction is one of the major parameters influencing the bulk friction behaviour. Lastly, the coefficient of restitution, together with sliding friction, are one of the major mechanisms for the dissipation of energy.

3.1.2. Model environment

This section describes the type of DEM simulation which is modelled in this thesis: *a quasi-static penetration of a plate in a dry granular medium*. The model environment is explained in detail in this section.

Penetration velocity

Pile driving through scour protection under self-weight penetration is a slow process since the penetration through the rocks is only due to the submerged weight of the steel pile with no hammer blows applied to the head of the pile. The process can be considered quasi-static since there is a low flow regime. Albert et al. (1999) indicated an expression which calculates the critical velocity v_c for the velocity regime of the pile v, by considering the mean diameter of the grains d_{50} and the gravitational acceleration g, as shown in Equation 3.1. Later, Feng et al. (2019) and Gezgin et al. (2020) used this expression to establish the maximum quasi-static penetration of an intruder object in a granular medium. By having a penetration velocity smaller than the critical velocity, this insures that the resistance force is independent of the velocity of the penetrating object.

$$v < v_c = \frac{\sqrt{4gR_{min}}}{10} \tag{3.1}$$

For the application in this thesis, by considering a R_{min} of about 2.5 mm, then the critical velocity becomes 3.1 cm/s. If the grain radius is larger, for instance 100 mm, then the penetration velocity can be increased up to 19.8 cm/s in order to insure that it has no influence on the resistance force. Esposito et al. (2018) identifies that penetration velocities in the range 5 to 125 cm/s were used by various authors for the penetration tests, however, the most common values of 0.2, 1, 2 and 10 cm/s are found. It can also be seen, that slower velocities (such as 0.2 cm/s) are only used with 2D models due to their advantageous computation time.

Influence of water

Although the real application of monopile penetration takes place in the offshore waters, there is no need to consider a particle-fluid coupling when representing the scenario in DEM, for several reasons. According to Zhu et al. (2008), DEM - CFD coupling is generally used to represent the interactions in the particle-fluid systems such as fluidization problems but also in processes where the packing of grains is loose and turbulent flow conditions can develop. In geomechanics, density of particles is rather high, so in most cases, flow can considered laminar (O'Sullivan, 2011b). Some typical geotechnical scenarios where DEM- CFD is applicable are problems involving total head variation, internal erosion or liquefaction. These can cause particle motion, large deformations, instabilities or even major failures, thus in this case it becomes essential to consider the influence of water on the behaviour of the material. However, for the application of quasi-static penetration of pile through scour protection layer, no geotechnical concerns are predicted with respect to instabilities of the scour protection due to the particle-fluid interaction.

Another argument which supports the lack of water influence for the application of this thesis, can be formulated in terms of effective stress. Helmons and Miedema (2007) considered the drainage behaviour in scenario when a cutting tool is used for underwater rock exaction. Because the Pore-Peclet number for pore pressure dissipation is difficult to approximate for the case of pile penetration, the drained regime can be identified using an alternative solution. DeJong et al. (2013) uses the formula indicated in Equation 3.2 to identify if the regime is drained, which means that the fluid can migrate through the pores without having an effect on the rock skeleton. For gravel type material, the consolidation coefficient c_h is very large since it is direct proportional to the Young's modulus E and hydraulic conductivity k of the material (see Table 2.6). As calculated before, the penetration rate v for quasi-static regime should be below 20 cm/s for particle size up to 200 mm in diameter. In Equation 3.2, w denotes the cone diameter, but it can be considered also the thickness of the pile wall or the plate in the experiment. Figure 3.1 plots the normalised velocity V and it can be seen that at very high consolidation coefficients and low penetration speeds, the regime is drained. Thus, this shows that the there is a fast dissipation of water pressure and no influence of the pore pressure on the rock skeleton.

$$V = \frac{v \cdot w}{c_h} \tag{3.2}$$
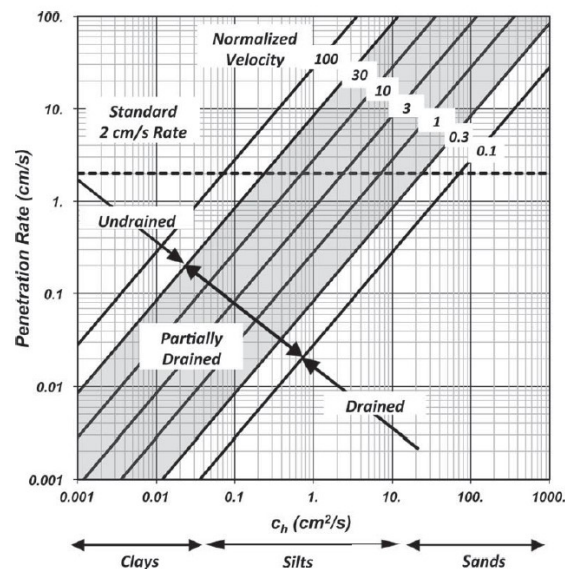
Figure 3.1: Field decision chart indicating the relation between coefficient of consolidation and penetration velocity (DeJong et al., 2013)

3.1.3. Methods to reduce DEM computation time

This section brings several methods which have been identified as ways to reduce the amount of computation time required for the DEM simulations. Some of the techniques applicable for the case of a quasi-statically penetrating plate in a granular medium are: shape simplification, scaling techniques, reduction of elastic moduli and domain reduction.

Shape simplification

Scour protection material comes with irregular shapes since they are broken quarried rocks, however for the purpose of reducing the computation time, their shape in DEM can simplified to spheres. In EDEM, this simplification of particle shape can be implemented as either single spheres or multi-spheres. The advantages of each of these shapes can be summarised as follows:

- **Sphere**: For a reduced computational time, one could choose this shape as an approximation to the real particle shape. The problem with spherical particles is that the bulk friction is too low compared to real granular material, a crushed angular rock Coetzee (2016). The lack of shape complexity is dealt with by imposing static and rolling friction in order to represent a hindrance to rolling or a more realistic packing and interlocking. In this way, spheres can approximate fairly good the behaviour of non-round particles. In addition to the low computation cost, spheres also provide the most accurate contact detection as well as very accurate evaluation of contact overlap EDEM (2018).

- **Multi-sphere**: Particle shape can also be approximated by a number of overlapping or touching spheres giving a better approximation to the real irregularities of the particles. In comparison to polyhedrons, multi-spheres come with a high computational efficiency and are able to maintain from the accuracy of spheres. Theoretically speaking, any particle shape could be modelled by increasing the number of overlapping spheres, however, one has to make a trade-off between the accuracy of the model desired and the computational time, since an increased number of smaller spheres comes with a higher computation cost.

Therefore, to compensate for the shape simplification, rotation can be inhibited such that angular motion of the particles is minimised and a better interlocking can be achieved. Another option is to use a rolling friction model. There are multiple options for a spring-damper rolling friction models, however the most common are:

- **Model A**: Applies a constant resistive torque, proportional to the normal contact force and which acts in a direction opposite to the rolling direction. This is the build-in model in EDEM, however this model is most applicable for a dynamic environment. In static conditions, the bulk material creeps due to rapid oscillations in the rolling resistance due to the discontinuity in the equation of torque when the relative angular velocity of the two particles in contact is zero (Wensrich and Katterfeld, 2012). The equations for the rolling friction model A, the build-in rolling friction model of EDEM, were included in Table 2.7.

- **Model C** (Iwashita and Oda, 1998): An elastic–plastic spring dashpot model, which introduce an amount of compliance and viscous damping to each rolling contact. Thus, this model deals with the discontinuity of model A, allowing for a continuous calculation of rolling resistance torque, even where there is zero angular velocity. The difference between the two rolling friction model can be seen in Figure 3.2, which shows the relation between the torque τ and angular distance θ for particles which roll for a fixed angular distance before stopping and rolling in the opposite direction. For the equations of this rolling friction model described in a incremental way, one should refer to the paper of Wensrich and Katterfeld (2012).
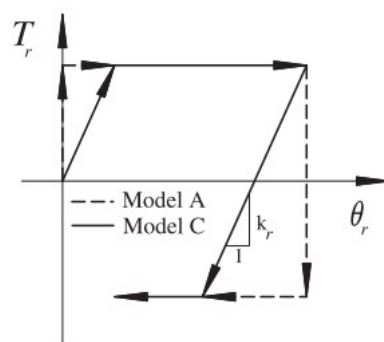
Figure 3.2: Elastic components comparison between the rolling friction Model A and C (Wensrich and Katterfeld, 2012)

In EDEM, particle can be randomly generated using a dynamic factory defined based on a pre-set generation rate until a certain mass is reached. The generation rate is important for the computational time and and it can be described as follows: if the mass per-timestep is greater than the smallest particle mass, then the factory is able to place particles until it reaches the required mass per timestep EDEM (2018). Simultaneously, with the particle generation, particles are allowed to settle under gravity until reach a quasi-static condition which implies that their average velocity should be lower than 10^{-5} m/s (Mohajeri, 2021).

Throughout generation of particle, the particle are in a dynamic regime since they are allowed to settle (their velocity is non-zero). However, during the penetration experiment, the slow penetration of the object and the velocity generated on the resting particle is small relative to the settling velocities, thus this regime could be considered quasi-static. Therefore, one can identify the need to use a rolling friction model which satisfies both a dynamic and an quasi-static situation. Rolling model C is identified as a suitable model for these conditions (Katterfeld et al., 2019). Ai et al. (2011) confirms the suitability of the model for angle of repose tests and Mohajeri (2021) identifies the drawbacks of rolling friction model A for penetration tests and concludes that the build-in model produces unstable results. Therefore, model C will be further used in the DEM simulations of both angle of repose and penetration models.

The rolling resistance is often employed as an alternative to modelling a realistic shape of the particles. The research of Zhou et al. (2013) identifies that the rolling resistance model used is not able to replace the particle shape effects and one cannot obtain a realistic behaviour of the bulk material. Thus, using more complex shapes cannot be eliminated from the calibration procedure.

Also in the topic of shape of particles used in DEM models and particle generation procedure, the size distribution is also important. For the purpose of replicating as close as possible the laboratory experiment, the same PSD should be implemented in the numerical model. However, the algorithm of the dynamic factory places far more smaller particles than requested in the inputted PSD, since larger particles are usually harder to be generated in free locations. Therefore, the solution is to simplify the PSD and use a normally distributed size distribution with a mean and a standard deviation which follows reasonably well the initial size distribution of particles, however with a big computational advantage since less smaller particles are needed to be generated.

Scaling techniques

Scaling is an important topic to this thesis, since it applies to both the numerical model and the experimental test. With respect to the experimental tests, a full-scale experiment of pile penetrations is costly and requires investing a significant amount of time. More common are the small scale lab tests, in which the geometry is down-scaled in order to reduce the amount material used and use a smaller sized equipment. Moreover, there are pre-established scaling laws which can be used when reducing the geometry of the system, by a factor N as shown in Table 3.1. The α factor can be set to 0 if the stiffness in the model is identical to that in the prototype, which also means that the stiffness is independent of the stress level (Wood, 2004). Is the value of α is 1, the stiffness directly scales with the stress.

Table 3.1: Scale factors for geotechnical modelling for laboratory at normal gravitational acceleration (Wood, 2004)

Quantity	Scale factor
Length	$1/N$
Density	1
Stress	$1/N$
Force	$1/N^3$
Strain	$1/N^{1-\alpha}$
Displacement	$1/N^{2-\alpha}$
Velocity	$1/N^{1-\alpha/2}$

It is also very uncommon for researchers to create a model in DEM at the same scale as the prototype. The reason behind this is mostly related to computational time, since a large number of particles is directly linked to longer computational time. In many cases, it can be expensive and unfeasible to use highest-performance Graphics Processing Units (GPUs) or multi-threading to speed up the computation process. Thus, there are other scaling techniques which can be identified as commonly employed in DEM:

- *Exact scaling* refers to scaling the geometry and the particle size by the same factor. This approach is used especially for designing a model which needs to be calibrated using a laboratory experiment. However, this method does not come with a reduced computational time, since the number of particle remains unchanged. Feng et al. (2009) elaborated on the scaling laws applied for exact scaling in DEM and identifies the same scaling laws for length and force as inserted in Table 3.1. Moreover, Feng and Owen (2014) state that the Hertz-Mindlin contact law is scale invariant for 3D spherical particles.

- *Scalping* or *Cut off* technique involves excluding small particles and replace their size fraction with a larger particle size fraction. An example of paper where this approach is implemented is Roessler and Katterfeld (2016), however by omitting the smaller fraction, the porosity of the bed material might be altered.

- *Geometry up or down scaling* considers only a scaling factor for the geometry, leaving the particles size unchanged. This technique lowers the computational time since less particles are included in the domain, however, boundary effects might be very high.

- *Coarse graining* refers to scaling the particle size, while keeping the domain size contrast. In this way, several particles can be replaced by larger particles, thus reducing the number of particles in the system. Thakur et al. (2016) elaborates on the scaling laws applied for this scaling technique to maintain mechanical and dynamical similarity.

- *Local refinement* is a technique which is commonly used in DEM, especially for the topic of penetration tests. Authors such as McDowell et al. (2012), Shi et al. (2019) and Zhao et al. (2019) allowed for smaller particles to be generated near the penetrating object. Wall effects are reduced by increasing the domain size by adding larger particles near the boundaries. However, the up-scaled particles outside the interest zone do not bring a significant computation advantage, since the speed of DEM solvers is also highly dependent on the smallest particles size used in the simulation, as shown in the time step formula in Equation 2.7.

Other parameters

The same equation used to calculate the time-step (Equation 2.7), reveals that the shear modulus has a direct influence on the computation time. In particular, a reduction of the shear modulus could be a major improvement for the computation time. It is however important to reduce the shear modulus in such a way that there is no influence on the KPIs of the models. Yan et al. (2015) shows that reducing the Young's modulus can speed up the simulations with little influence in the bulk behaviour. Angle of repose is hardly changed when using Young's modulus of the order $10^7 - 10^{11}$ Pa, as suggested by Lommen et al. (2014) and Yan et al. (2015), however lower values can give unrealistic bulk behaviour. For the penetration test, values of shear modulus over 10^8 Pa do not exhibit large difference in penetration resistance, however Lommen et al. (2014) suggest verification of this statement.

Another technique to reduce the computation time is to investigate the effect of domain reduction on the overall response of the system. This is a special case for the geometry down-scaling method, and refers to diminishing the domain dimensions only, leaving other geometries (e.g. the penetrating object) at full scale. For the angle of repose test, Roessler and Katterfeld (2018) find that a reduction in the dimension of the cylinder can be performed as long as the ratio between the diameter and the length of lifting cylinder remains constant.

3.1.4. Calibration strategy

Overview

Two main approaches are identified for DEM calibration strategy. Firstly, the most accurate is the direct measuring approach (Coetzee, 2019), in which the input micro-parameters are directly measured at particle or contact level (such as those identified in Section 3.1.1), However, this could not guarantee an accurate bulk behaviour of the material, in addition to the disadvantage of complexity of the experimental tests which need to measure properties at particulate level. An alternative approach is the bulk (reverse) calibration in which a laboratory experiment is conducted and the material's bulk property is recorded. Then, the same experiment is numerically simulated and the micro-parameters are varied until the predicted bulk behaviour matches the experimental measurements. Coetzee (2019) also specifies that the numerical model is designed at the same geometrical scale as the experimental work, such that the bulk behaviour can be more accurately compared.

This reverse calibration method is also implemented in this study and it makes use of multiple experimental results to determine bulk responses and then numerically determine the equivalent Key Performance Indicators (KPIs). In this thesis, two experimental tests are used to aid the calibration of the numerical model. The main test is the penetration test, however an additional test is the angle of repose test. By having two KPIs, the solutions can be overlapped and thus the common optimal set of input parameters can be found. Ideally, one can get to an unique set of solution if a significant amount of bulk responses are to be calibrated. However this comes with the feasibility problem, which says that it is possible no combination of independent variable that give the desired experimental bulk response.

For an easier understanding of the calibration strategy embraced in this thesis, refer to Figure 3.3. The flowchart identifies the need to first perform an investigation on the ranges for the constant and varying parameters by checking specialised literature. Then, a sensitivity analysis can be conducted to reduce the amount of unknown variables and conclude on their influence on the response variables. The next step involves a set of simulations to identity the final optimised set of input parameters, which can be referred to as the Design of Experiments (DoE) strategy. Lastly, the results are post processed, and the best set of input variables which matches the closest the experimental response is identified.

1. Literature analysis	2. Sensitivity analysis	3. DoE	4. Post-process
• *Choose constant parameters* • *Establish range for varying parameters*	• *Find the most adequate value for all the parameters* • *Create reference model*	• *Create design matrix* • *Perform the required runs*	• *Interpolate the results or create a regression analysis*
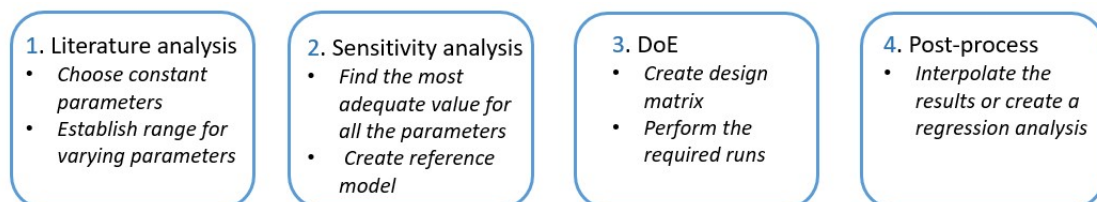
Figure 3.3: Overview calibration steps

Calibration parameters: angle of repose test

The angle of repose is the maximum slope angle of the material between a horizontal plane and the top surface of the pile formed by the dumped loose material (CARRIGY, 1970). There are numerous ways to construct a pile and calculate the angle of a free standing surface: lifting cylinder test, shear box (ledge method), trap door test or rotating drum test (Katterfeld et al., 2019). All these tests involve the measurement of the angle of repose α_{AoR}, however they do not necessarily lead to the same response value because of the different kinetic energies produced in each test. Therefore, the calibration strategy identified in this section only refers to a lifting cylinder test.

Roessler and Katterfeld (2018) and Li et al. (2017) indicate that an increase in the lifting velocity results in a smaller AoR since the particles get more activated. Li et al. (2017) investigated the relation between lifting speed $v_{AoR}(m/s)$ and particle diameter $d_{50}(mm)$. Using experimental results of a fixed-base cylinder method AoR and subsequent DEM simulations, an analytical relation for the $\alpha_{AoR}(^o)$ was found (Equation 3.3). The experimental data can be seen in Figure 3.4, which allowed for different

particles sizes and lifting velocities ($v = v_{AoR}$). For instance, given that the α_{AoR} is 35° and the d_{50} is 10 mm, then this formula identifies a lifting velocity of approximately 2 cm/s.

$$\alpha_{AoR} = 33.57 + 63.92 * v_{AoR} * ln(v_{AoR}) + 0.68 * d_{50} \qquad (3.3)$$
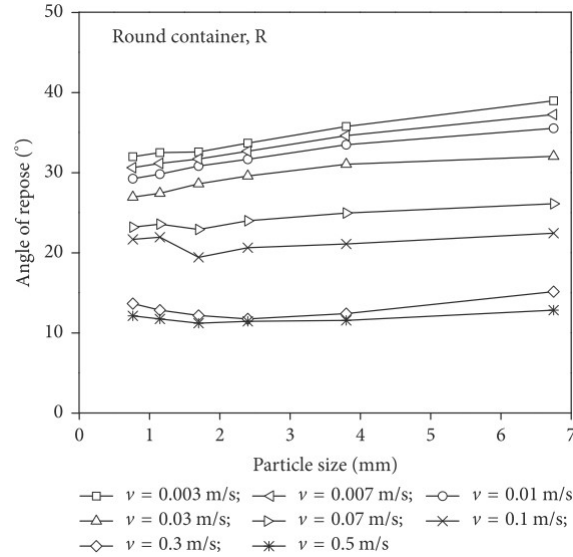
Figure 3.4: Impact particle size on angle of repose for various lifting velocities (Li et al., 2017)

Also with respect to the AoR test, other parameters which need to be calibrated are the particle particle coefficients: restitution, static and rolling friction. Figure 3.5 shows a couple of trends. It can also be seen that at higher friction coefficients, the repose angle decreases as the coefficient of restitution coefficient increases, thus making the friction and restitution coefficients cross correlated Yan et al. (2015). Therefore, restitution coefficient has little influence on the shape of discharged material and will thus be assumed as a constant variable in this thesis in order to reduce the number of parameters to be calibrated. Katterfeld et al. (2019) suggest a restitution coefficient between 0.2 and 0.4 (-). However, since in this thesis, the particles are going to be generated using pluviation method, high restitution coefficient would allow the particle to bounce higher, which is an unrealistic behaviour for a quasi-static simulation. Thus, a constant restitution coefficient of $e = 0.01$ (-) is going to be used in the DEM simulations for both particle-particle and particle-wall interaction, provided that no additional tests are performed which could give a better approximation for this parameter.
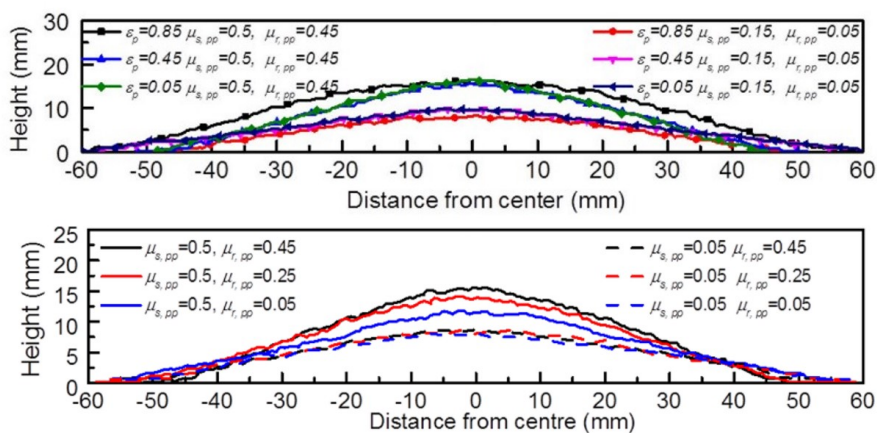
Figure 3.5: Effect of restitution coefficient and rolling friction coefficient on profile discharged material (Yan et al., 2015)

Moreover, Figure 3.5 shows that with an increase of static or rolling friction between particles, the height of the pile increases while the width decreases, resulting in an increased AoR. The interdependence of static and rolling friction on the angle of repose is also identified by Wensrich and Katterfeld (2012), which concludes that a large angle of repose can only be achieved if both these coefficients are large.

The last remark on the calibration strategy of AoR test refers to the friction between particles and the lifting cylinder which is less significant than the friction between the particles and the base surface (Roessler and Katterfeld, 2018). Therefore, for simplicity, the properties of the material modelled in DEM for the cylinder are identical to that of the bottom plate.

Calibration parameters: penetration test

Static friction coefficient between the particle and the geometry (for instance the penetrating object) can be considered as a constant variable for the Hertz-Mindlin contact model. It is calculated as the tangent of the interface friction angle, which depends on the surface roughness of the material. For a well-graded rock fill in contact with a steel pile, the friction angle can be approximated as 22° (Fine (2021) and Bosscher et al. (1988)). However, it can be acknowledged that for large angular armour rock in contact with steel material, the interface friction can significantly reduce to a value below 0.2 (-). Sitbba Rao et al. (1998). However, an input value for $\mu_{s,p-g}$ of 0.4 (-) will be further used as a constant in the DEM simulations, if this parameter cannot be measured using a specialised laboratory test.

Rolling friction for particle-geometry does not have a big influence on the tangential shear stress at steady state flow, as concluded by Simons et al. (2015) which constructed a sensitivity analysis on the calibration parameters for a ring shear test. Therefore, $\mu_{r,p-g}$ is considered to be taken as a constant with the value equal to 0.5 (-).

Key Performance Indicators

The calculation of the response (dependent) variables, also referred to as the Key Performance Indicators (KPIs) of the model, need to be further elaborated. Therefore, a description on how to compute both the angle of repose and the penetration resistance from EDEM needs to be further specified:

- **Angle of repose (AoR)**: There are several methods how to get this response variable from the DEM simulation. The first and most simplistic method is to use the 3D visualisation of the formed pile and select two extreme particles, calculating the angle between the formed line and the horizontal surface using the in-built protractor function. Other method is to export a 2D image with the pile and read the image from exported graphics file to approximate a best fit line. Both of these method lack accuracy since they are highly dependent on the selected line. A more automated and thorough method is to export the final particle positions and their respective diameters and fit a cone through the pile of particles. In this way, using the equation of a cone, the best fit surface is created to fit on top of the entire 3D pile volume. This method is chosen in this study due to its versatility, accuracy and efficiency. The Python code which determined this angle of repose is inserted in Appendix D.

- **Penetration resistance**: The force can be determined directly from EDEM and it is total force in the vertical direction on the geometry, the penetrating plate. The data is exported as force in time, and using the constant velocity of the plate, penetration depth can be easily calculated. The force can be translated into work using the trapezoidal rule, which is a technique often used in numerical analysis. It involves evaluating the area under the force curve by dividing the total area into little trapezoids. In this way the work (which is the product of force and distance) can be calculated at each penetration depth.

Strategy sensitivity analysis

What needs to be further drawn attention to is the fact that the calibration strategy involves an intermediate step, a sensitivity analysis which has the purpose to identify what is the influence of certain key parameters on the bulk behaviour of the system. The benefit of performing a sensitivity study is that it reduces the uncertainty of the model by studying qualitatively or quantitatively the model response to the change of input variables, or by analysing the interactions between variables (Wexler, 2014). The parameters involved in the sensitivity analysis have a direct relation to the computation time, thus it is convenient to decide on the most appropriate values before conducting the DoE. For instance, particle shear modulus, but also the lifting and penetration velocity are key to the computational time.

Design of Experiments

After having established the reference case, calibration of the most influential parameters can be performed during Design of Experiments (DoE). The book of Antony (2014) shows how this approach is implemented in engineering practices. DoE is a method which aims to identify the influence of one or more factors on a certain model. In other words, it allows to construct a relationship between input and output set of parameters and see which variable have most influence on the response. It also allows to determine the optimum set of input parameters which give the desired output.

Therefore, the last stage of the calibration process is to construct a design matrix, in which the independent parameters are varied in a systematic way such that an adequate combination of input parameters is to be found. In other words, a certain number of factors are chosen as most influential on the outcome and a certain number of levels is chosen accordingly. Then, the numerical model is run using these different combinations of factors and levels.

The most complex design matrix is the Full Factorial Design (FFD) since it creates all the possible combinations of all the factors and levels (see Figure 3.6 for an example for a FFD design matrix). This technique is much more favourable for calibration purpose than One Variable at a Time (OVAT) since it considers all the interactions between factors. Other methods include screening or various fractional factorial designs which can reduce the number of runs required (refer to the book of Antony (2014) for further details).

Process Parameters	Labels	Low Level	High Level
Plating time	A	4 s	12 s
Plating solution temperature	B	16°C	32°C

Trial Number	A	B	Plating Thickness				
1	4	16	116.1	116.9	112.6	118.7	114.9
2	4	32	106.7	107.5	105.9	107.1	106.5
3	12	16	116.5	115.5	119.2	114.7	118.3
4	12	32	123.2	125.1	124.5	124.0	124.7

Figure 3.6: Design matrix FFD: factors, levels, response variables (Antony, 2014)

Moreover, one can identify two types of factors which are to be used in the DoE. First and most obvious are the continuous factors which have different levels. In addition, one can identify the categorical factors, which are parameters which can be activated during the initial set-up of the model. Rolling friction can be considered a categorical parameter, since as explained before in Section 3.1.3. However, for simplicity, this separate case is considered as the lower level boundary in the design matrix of the continuous rolling friction factor. In addition, the DoE matrix considers the case of various shapes as categorical factors.

In this thesis, particle shape is a categorical independent variable since the influence of having one or

more spheres or polyhedrons on the bulk result needs to be investigated. In other words, the focus does not lay in representing accurately the shape of the crushed rock fragments, but in the interlocking between particles, which can easily be done my introduction clumps in the model. For instance, a very simple, yet efficient way to create these shapes is described in the research of Coetzee (2016) which manually creates clumps based on three representative shapes of fragments of rock: spherical, elongated and pyramid shape as shown in Figure 3.7.
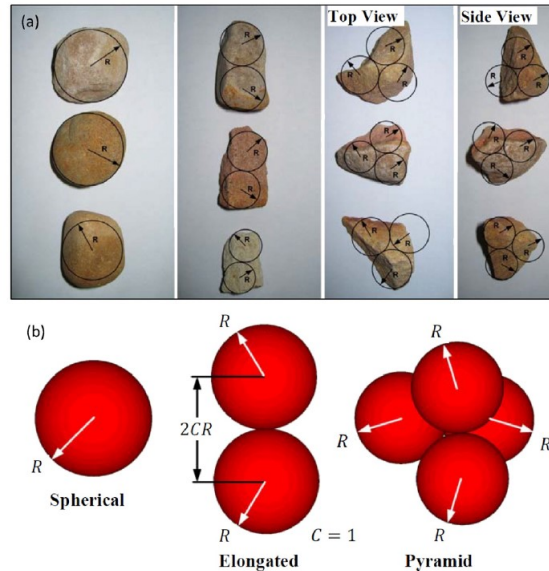
Figure 3.7: Representative rock fragments (a) and manual clump representation (b) (Coetzee, 2016)

Final remarks calibration strategy

Therefore, this section identified the strategy to set up the DEM model for a penetration test and the subsequent angle of repose test. It was shown which are the key micro-parameters influencing the bulk response, what kind of environment should be set-up, but also numerous ways one can reduce the computational time. Lastly, it was established which variables can be considered constants, and which should be further investigated since they influence the most the bulk response of the system. Lastly, the chapter identified the strategy to perform the calibration through DoE method.

3.2. Case study

The calibration plan presented in Section 3.1 is applied to an initial case study which uses a pre-exiting laboratory penetration test. The purpose of this case study is to establish the applicability and the efficiency of the previously defined calibration strategy. Therefore, this section aims to describe the experimental test and how it can be replicated in DEM by performing a sensitivity analysis with several unknown parameters.

3.2.1. Deltares laboratory experiment

This preliminary analysis uses the laboratory experiment performed by Deltares, which is a Dutch independent institute for applied research in the field of water and subsurface. The experiments were done previous to the start of this research, so the author was not involved in the set-up of the experiments. The results, as well as some characteristics of material used experiments are described below.

The laboratory test (refer to Figure 3.8) is a dry penetration test which includes confining rings filled with sand underlying granitic rock fragments. The d_{50} of the rock is 9.11 mm, and angular fragments

have sizes ranging between 4 and 12 mm (see Figure 3.9). Additional properties are inserted in Table 3.2. The dimensions of the container are included in Table 3.4. Therefore, the only ratio of mean rock size over the width of the penetrating tool investigated in this experiment is $d_{50}/w = 1.8$. The procedure involves pushing a rectangular cross-section steel plate into the granular material using a hydraulic plunger. The displacement and force required for penetration at each time step are recorded. Penetration resistance with depth is displayed in Figure 3.10 where and it can be seen that it exceeds 3 kN at 30 cm depth and the work needed for this penetration is 360 J.

Figure 3.8: Laboratory experiments of a plate penetrating in granular material (left) and angle of repose (right)
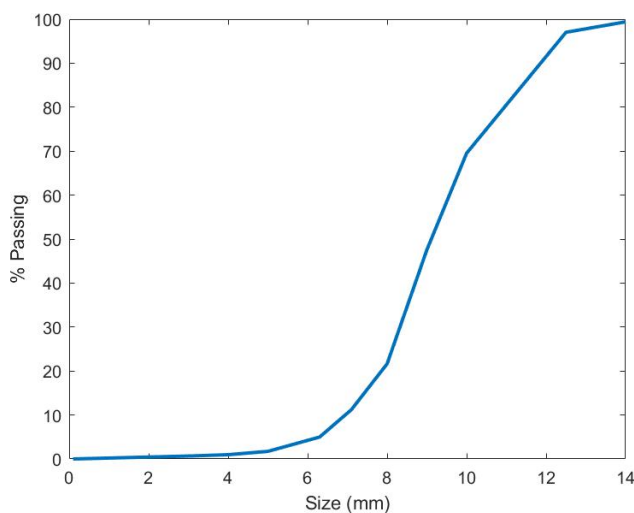
Figure 3.9: PSD of the rock fragments

Table 3.2: Material properties

Parameter	Value
Mean diameter	9.1 mm
Density (particle)	2668 kg/m^3
Density (bulk)	1371 kg/m^3
Porosity (bulk)	0.48 $(-)$

Moreover, an additional test was performed, the Angle of Repose (AoR) test (see Figure 3.8). Cylinder lifting test was chosen method to calculate the angle of repose. The laboratory set-up involves filling a cylinder with the same granular material used in the penetration test and lifting slowly the cylinder until all of the rock fragments form a stable pile on a bottom plate.

Table 3.3 provides with the output data sets, which can be referred to, for calibration purposes, as response (dependent) variables or KPIs. The angle of repose was determined using a laser scan of the pile and a standard deviation of 2 degrees was established. The penetration force at each depth can be translated into work ($J = N * m$), thus it is considered more convenient to use work as response variable for the purpose of DoE.
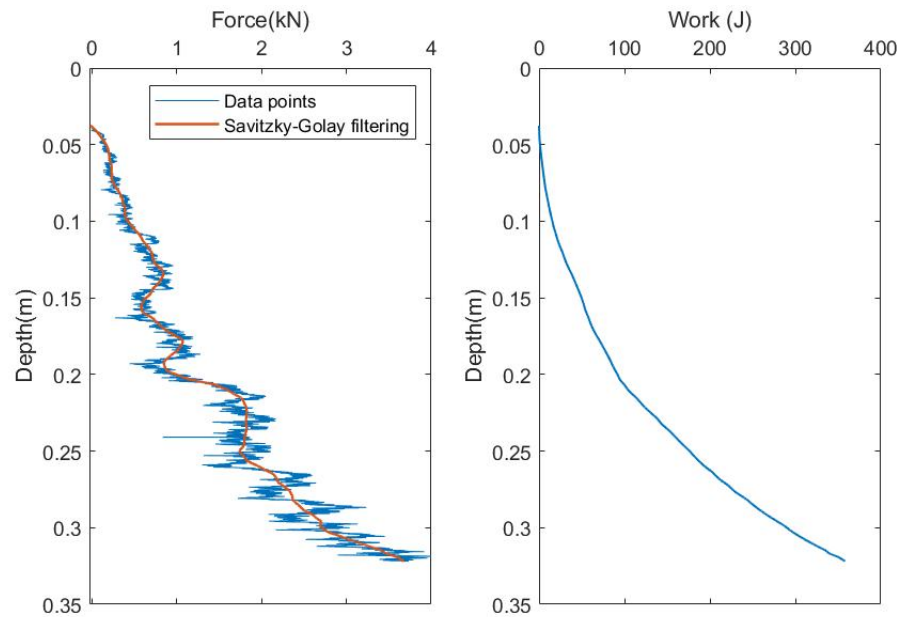
Figure 3.10: Axial resistance from Deltares laboratory experiment

Table 3.3: Output data from laboratory experiments

Output	Value
Angle of Repose (α_{AoR})	35.1 ± 2 (^{o})
Work at 0.3 m penetration (W)	360 (J)

3.2.2. DEM model set-up

The idea behind using Deltares experimental data is to replicate the same exact test in DEM in order to calibrate the rest of the unknown micro-parameters. However, this one-to-one replication of the test comes with some issues. Since the author did not actively participate in the experiment, there are certain parameters which need to be approximated, for instance the size of the rings, the lifting speed of the cylinder for the AoR test. Moreover, apart form the AoR test, no other additional test was performed with the aim to provide in depth knowledge on the micro-parameters needed for the DEM model, such as friction or restitution coefficients.

The DEM set-ups which aims to replicate the experimental penetration and AoR test is inserted in Figure 3.11. For the purpose of reducing the uncertainty of the DEM model and replicating as accurate as possible the penetration test, it is considered important to keep the original geometrical dimensions from the laboratory experiment, as indicated in Table 3.4. Nevertheless, for computational efficiency, the underlying sand layer is replaced by a hard boundary. In addition, during the sensitivity analysis, the container used in the penetration test is reduced in order to diminish the particle number required in the penetration model (reduced dimensions are also included in Table 3.4). Moreover, as shown in Section 3.1.3, the geometries involved in the lifting cylinder test can be decreased such that the response of the system is not perturbed. Refer to Table 3.4 for the reduced dimensions of the AoR test geometries used in the DEM simulation with the purpose to speed up computation time.
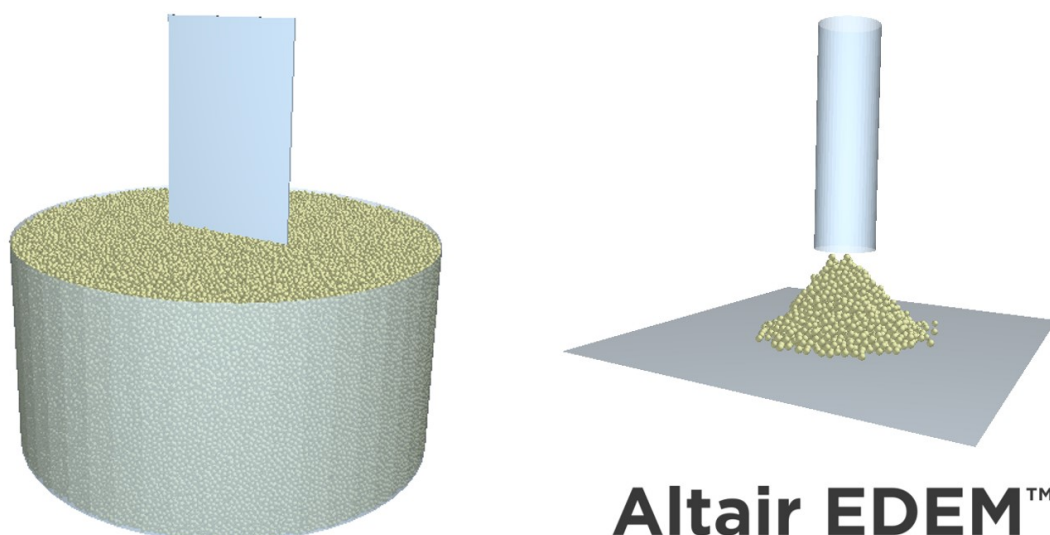
Figure 3.11: DEM test set up: penetration test (left) and AoR test (right)

Table 3.4: Experimental and Simulation Domain comparison

Characteristic	Notation	Unit	Value Experiment	Value DEM
Angle of Repose Test				
Cylinder				
Diameter	D_{AoR}	m	0.168	0.084
Height	H_{AoR}	m	0.6	0.3
Lifting velocity	v_{AoR}	m/s	NS[a]	0.03[b]
Penetration Test				
Domain				
Diameter	D	m	0.9	0.9 (0.3 [c])
Height	H	m	0.3	0.3 (0.1[c])
Penetration velocity	v	m/s	≈ 0.0012	0.008[b]
Plate				
Width	w	m	0.005	0.005
Length	l	m	0.3	0.3 (0.1[c])
Height	h	m	0.45	0.45 (0.15[c])
Ratio				
Size rock/width plate	d_{50}/w	$-$	1.82	1.82

[a] NS - Not Specified
[b] Value chosen after performing the sensitivity analysis
[c] Value used only during the sensitivity analysis

3.2.3. DEM calibration plan

As explained in Section 3.1.4, the first step in a calibration study is to construct a sensitivity study with certain variables based on a reference model. Table 3.5 gives an overview of the micro-scale parameters used to create this reference model. The choice of most of the variable was previously established in Section 3.1.4, others were chosen according to the engineering judgement. Sensitivity analysis can provide with a reasonable value for the particle shear modulus which allows a significant reduction in the required computation time, as explained in Section 3.1.3. Other parameters such as static and rolling friction coefficients between particle are to be further calibrated in order identify the best set of input variable which can provide a bulk response similar to that in the laboratory experiments.

Following the sensitivity analysis, the DoE for calibration purposes needs to be created. This should

provide with the best fit variables which can give the final calibrated set of input parameters. This however, needs to be verified and validated, only then the DEM model is completed.

Table 3.5: Constant values for the reference DEM models

Characteristic	Notation[a]	Unit	Value DEM
Particle			
Mean diameter	d_{50}	mm	9.1
Density	ρ_p	kg/m^3	2668
Shear Modulus	G_p	GPa	10^b
Poisson's Ratio	v_p	-	0.25
Geometry			
Density	ρ_g	kg/m^3	8050
Shear Modulus	G_g	GPa	80
Poisson's Ratio	v_g	-	0.27
Interaction particle-particle			
Coefficient of restitution	$e_{p,p}$	-	0.01
Coefficient of static friction	$\mu_{s,p-p}$	-	0.7
Coefficient of rolling friction	$\mu_{r,p-p}$	-	0.6
Interaction particle-geometry			
Coefficient of restitution	$e_{p,g}$	-	0.01
Coefficient of static friction	$\mu_{s,p-g}$	-	0.4
Coefficient of rolling friction	$\mu_{r,p-g}$	-	0.5

[a] Particle (p) and Geometry (g)
[b] Value chosen after performing the sensitivity analysis

3.2.4. Sensitivity analysis

Preparation

Before pursuing the actual calibration of the model parameters, a sensitivity analysis is considered essential as an intermediate step. The simulations constructed here are done only using spherical particles. Some of the parameter selection from Table 3.4 and Table 3.5 need to be varied accordingly to check the influence of input variables on the response variables. Thus, three parameters are considered during this sensitivity analysis:

- lifting velocity (v_{AoR})

- penetration velocity (v)

- shear modulus (G_p)

For this sensitivity analysis, OVAT (One Variable at a Time) method is chosen adequate since each input parameter can varied individually while while keeping the rest of the variables constant. The technique is most used to measure the influence of the parameter on the system by taking the difference of the outcome of a high and low parameter value (van Schepdael et al., 2016). Its main advantage is the little computational cost since it does not require any combination between parameters and their levels, which can also be seen as a drawback of the method, since one cannot study interactions between the parameters. Table 3.6 comes with the input properties which are to be varied in order to observe the influence of each input parameters on the bulk response of the system.

The results of this sensitivity analysis are presented as a set of graphs where each independent variables is plotted at different levels. The lifting and penetration velocity are first analysed, using a shear modulus of the particle (G_p) of 10^8 Pa. Afterwards, the shear modulus is varied simultaneously for both tests using the reference lifting (v_{AoR}) and penetration velocity (v) determined after performing the sensitivity analysis.

Table 3.6: Sensitivity Analysis: OVAT input variables

Parameter	Unit	Levels	AoR test	Penetration test
v_{AoR}	m/s	0.002, 0.01, 0.018, 0.034, 0.05	X	
v	m/s	0.0012, 0.008, 0.04		X
G_p	GPa	0.01, 0.05, 0.1, 0.5, 1, 5, 10, 50	X	X

Results lifting velocity

The conclusions of the sensitivity analysis on the lifting velocity can be expressed as follows. Since an adequate AoR confidence interval of 95% is about $\pm 2^o$, 3 repetitions for each variable at each level assures that the simulations provide an adequate range of values and that the true value can be found within this confidence interval. Figure 3.12 shows that lifting velocity can influence the AoR such that lower velocity brings higher AoR. Following the findings of Li et al. (2017), any low lifting velocity is adequate to be used as long as calibration of the micro-parameters is performed consequently. Therefore, for the reference case, a lifting velocity v_{AoR} =0.03 m/s is chosen and will be further used in the following simulations of the AoR model.
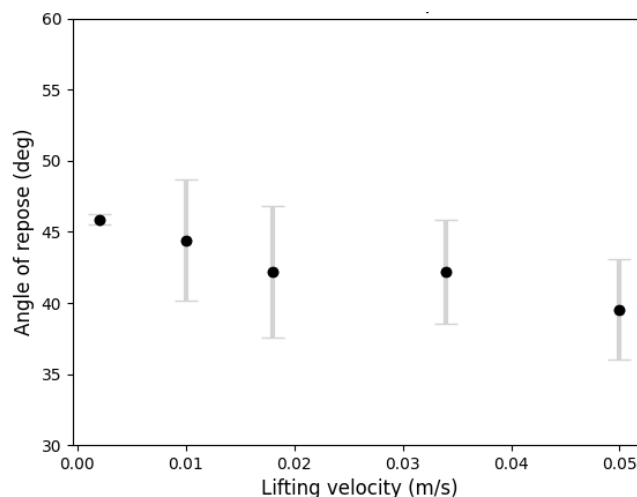
Figure 3.12: Sensitivity analysis of the influence of lifting velocity on the angle of repose (95% confidence interval shown)

Results penetration velocity

Creating a sensitivity analysis for the penetration velocity (v) is much more time consuming than for the AoR test. Thus, for the purpose of identifying the influence of shear modulus and penetration velocity parameters on the bulk response of the system, a reduced domain is considered. A reduction factor of 3 is applied to the diameter and height of the domain, and to the height and length of the plate (see Table 3.4 for the values used in DEM). The width of the plate is unchanged such that the ratio between the width of the penetrating object to the d_{50} of the rock should be kept constant.

It must also be highlighted that the penetration resistance from this sensitivity analysis cannot be compared in a quantitative way with that from the experiment since it is expected that the domain has a large influence on the penetration resistance. Furthermore, a number of 2 repetitions gives a similar 95% confidence interval as more repeated simulations. Thus, it is concluded that for further sensitivity and calibration studies, for the penetration model, only 2 simulations at each level are required for reproducibility purposes.

The laboratory experimental test used a very low velocity (approximately 0.0012 m/s) of the penetration plate. Looking at Figure 3.13 showing the results of the sensitivity analysis of the penetration velocity, it can be seen at higher velocities, the velocity distribution becomes wider because of the fact that the

number of contact points between geometry and particles becomes less. For instance, during a fast penetration, the average contact between the plate and the particles is 47 (-), while during a slower penetration the amount of contacts is 72 (-). This can be explained by the increased mobilisation of the particles as a result of faster penetration speed, so the particles get pushed further away form the plate, thus less contact points. Moreover, it can be seen that the penetration resistance increases with increasing penetration rate. This is in accordance with the concussion of Esposito et al. (2018) and with the trend-line presented by Butlanska et al. (2010b). The explanation is that with increasing penetration speed, the regime evolves from a quasi-static to a more dynamic situation, where more dynamic forces are mobilised.
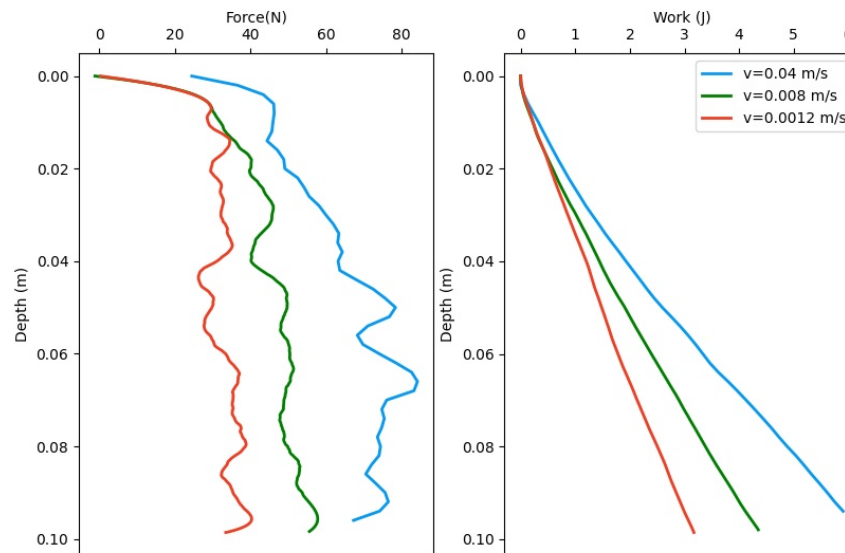
Figure 3.13: Sensitivity analysis of the influence of penetration speed on the penetration resistance

Furthermore, a low penetration speed comes with an increased computation time. For the purpose of calibration, where numerous runs are to be conducted, it is not beneficial to consider a very low penetration rate. It can acknowledged that there will be slight influence on the outcome of the penetration resistance, but this can be well compensated by calibrating the contact coefficients, as well investigating other possible shapes for the particles. Therefore, a value of $v = 0.008$ m/s is chosen to be further used as the penetration velocity for the DEM model in the case study.

Results shear modulus

After having established a reference value for the penetration and lifting speed, an investigation on the shear modulus for both tests can be made. The strategy used in this sensitivity analysis is to identify the smallest possible value for the shear modulus which can be used as input in the DEM model, such that the simulations give a similar bulk response to the experimental test. The suitability of applying this technique to scour protection rock material needs to be further elaborated. In general, a uni-axial compression test can be modelled in order to investigate the compressibility of the material. A small shear modulus indicates that the particles are soft and flexible and that a low force is required for deformation. This would not be realistic for a rock material, thus the allowed vertical strain due to compression should be below 10% in order to allow for this approximation. This approach will not be further investigated in this thesis, but attention needs to be called upon the fact that reducing the shear modulus is not a realistic approach and comes with uncertainties, however it is one of the most efficient solutions to reduce the computational time.

The results show that the shear modulus is not significant for the angle of repose test, however for

the penetration test, the parameter clearly influences the penetration resistance, as it can be seen in Figure 3.14. It can be seen that the lower the shear modulus is, the lower the penetration resistance becomes. In comparison to the results of Lommen et al. (2014), penetration resistance with depth is influenced by values higher than 10^8 Pa. It can also be recognised that for values smaller than $5 * 10^8$ Pa, there is not a realistic profile for the penetration resistance. This supports the reason why Gezgin et al. (2020) used this value for the shear modulus in their DEM penetration model.
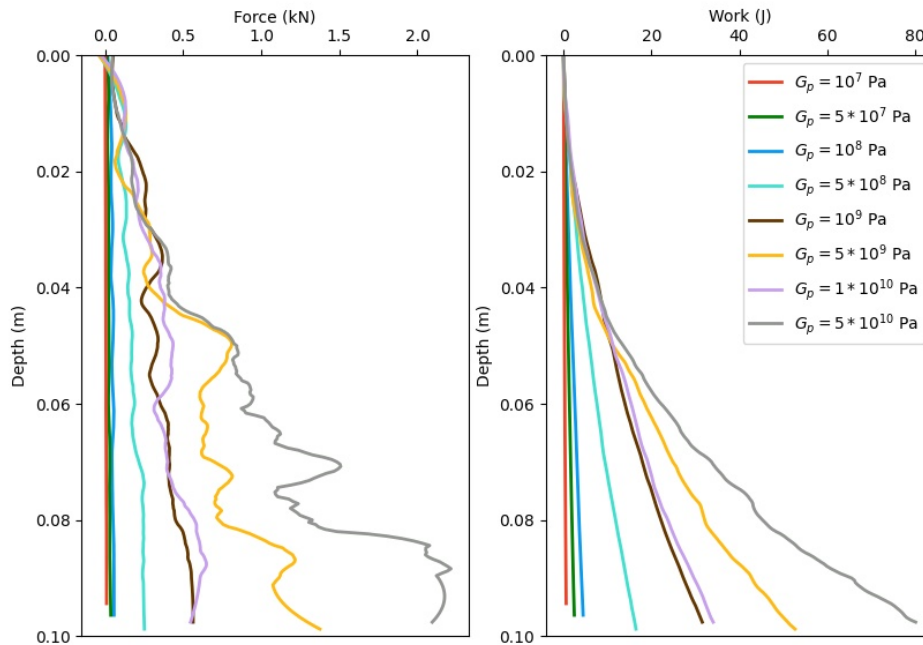
Figure 3.14: Sensitivity analysis of the influence of shear modulus on the penetration resistance

Although it can be considered that a shear modulus of $G_p = 10^9$ Pa is sufficient to give adequate results of penetration resistance, one needs to acknowledge that a concentration of high stresses is anticipated at the tip of the plate due to the interaction of the tip plate with larger particle sizes. In other words, in coarse and angular material, the resistance of the material to shearing becomes very relevant, therefore the shear modulus can significantly influence the penetration resistance. Thus, if one decides to use a lower shear modulus with the purpose to achieve lower computational time, then one should also acknowledge an underestimation of the penetration resistance with depth.

DoE plan

Following this sensitivity analysis and making use the knowledge gained after performing the calibration strategy in Section 3.1.4, two parameters from the reference model need to further calibrated, the inter-particle friction and rolling coefficients. Moreover, it was also shown that shape also plays an important role when calibrating these two variables, thus it will also be considered as a categorical factor in the DoE matrix revealed in Table 3.7.

Table 3.7: Design of experiments: calibration strategy

Shape	Parameter	Levels
Sphere & Multi-sphere & Polyhedron	$\mu_{s,p-p}$ (-)	0.1, 0.5, 0.9
Sphere	$\mu_{r,p-p}$ (-)	0.01, 0.4, 0.8

3.3. Discussion and conclusions

3.3.1. Options for research direction

The calibration of this penetration model is stopped due to several reasons. With current domain size included in Table 3.4 and using the input parameters introduced in Table 3.5, the computation time is too large. On a workstation with Intel(R) Xeon(R) with a CPU E5-1650v2@3.5GHz, and a GPU of AMD FirePro W5000 (FireGL V) graphics Adapter, the computation time for one single simulation defined by the DoE matrix takes approximately one week. This is considered impractical for the time assigned for the completion of this thesis bearing in mind that more than 40 simulations are designed for calibration purpose. Therefore alternatives are considered such that a DEM penetration model can be calibrated in the time frame allowed for this thesis:

- **Reducing the experimental domain**: This solution was also implemented during the previously conducted sensitivity analysis such that it allows for reasonable computational time. The results of the simulated penetration resistance are difficult to relate to the experimental test without an extensive investigation on the boundary effects. This method can be successfully implemented when there is high certainty of the accuracy of the input parameters. However, in this preliminary analysis, due to numerous unknown input parameters, it is considered to bring a considerable amount of uncertainty during the calibration purposes.

- **Local refinement**: This method was employed by numerous authors as exemplified in Section 2.4. This method reduce the computational time by allowing the particles further away from the penetrating tool to be up-scaled. Local refinement was described in more detail in Section 3.1.3. However, for a similar reason as option 1, this approach is considered to bring large uncertainty for calibration purpose since both the up-scaling factor and the extent of the local refinement area could have a direct effect of the KPIs of the model.

- **Design a new experimental test**: This method has the advantage that the author can design its own penetration test, perform additional test of the material in order to determine certain micro/macro parameters needed for input in the DEM model. In addition to this, experimental test can be performed using a limited domain size, various ratio of d_{50}/w, which can be used for both verification and validation purposes for the DEM model. Moreover, these experimental tests can be a valuable source of information in itself since bring the penetration profile trend line for various data-sets of combination of thickness of the penetration tool versus the size of the rock fragments.

This preliminary analysis brings certain developments which guide the author how to proceed in order to reach the scope of this research. The lessons learnt from conducting the simulations for the sensitivity analysis show a clear path towards the end objective of this research. Thus, the conclusions from applying the case study can be formulated in terms of results, but also with respect to a certain course of action for the research.

3.3.2. Conclusions preliminary analysis

There are several conclusions after performing an initial set of simulations, which are either beneficial for the computation time, or describe how a penetration test can be effectively modeled in EDEM:

1. **Shape**: For the purpose of penetration in material with large angular particles, approximation of the shape with single sphere is computationally efficient, however not a realistic solution. Static and rolling friction between spherical particles can replicate well the bulk behaviour of the real material. Nevertheless, it is essential to compare the solution of single sphere with that of various configurations of multi-spheres and polyhedrons and conclude on the effect of the shape on the penetration resistance. Moreover, it is discovered that due to the algorithm which EDEM uses

to generate the particles, using a normal distribution for particle sizes is preferred to inputting a PSD, since the factory generates more smaller particles than intended.

2. **Results sensitivity analysis**: The sensitivity analysis confirms the importance of penetration velocity on the penetration resistance. A quasi-static medium is essential and a similar velocity with that used the experiment is crucial in order to correctly calibrate the numerical model. In addition to this finding, shear modulus also influences the penetration resistance. Although it is a common practice to reduce the shear modulus in order to gain a reduction in the computational cost, this practice is not applicable for the application of a penetration test in a material composed of large particle size. Thus, it can be concluded that the shear modulus of the simulated material needs to be representative of the real shear modulus of the rock used in the experiments.

3. **Scaling**: Domain size is also found an essential aspect which has a direct influence on the response variables. Although for the AoR test the approach is verified, for the penetration test, it is found that the reducing the boundary vertical and horizontal extent can have an unknown effect on the KPI of the system. For calibration purposes, having little certainty about numerous input micro parameters, adding an extra factor of uncertainty would make the calibration process less likely to be successful without any additional sets of experimental simulations.

4. **Efficiency calibration strategy**: Regarding the calibration of micro-parameters used in EDEM, it was confirmed the adequacy of the strategy to set several parameters constant and only vary the most influential ones during DoE. For the case of penetration test, it can be concluded that the static and rolling coefficients between particle and geometry can be set as constants, and only the coefficients between particles are to be checked in order to find the corresponding set which gives the desired KPI.

Final research direction

This preliminary analysis can be concluded by highlighting the fact that the data from the penetration test from Deltares is insufficient since it only considers one single ratio of mean size of the rock to the thickness of the plate. In addition, it does not aid the calibration process of the numerical penetration model due to its high number of particles and large domain size, as concluded in this section. The advantages and disadvantages were assessed and the best approach to reach an answer for the research question in the available time devoted for conducting this research is to design a new penetration experimental test. This will not only provide with a significant data set of penetration resistance versus depth for various ratios of d_{50}/w, but also aid the calibration, validation and verification of the subsequent numerical DEM model in a reasonable amount of time.

4

Experimental model

This section aims to describe in details the process behind designing the experimental lab test set-up of the penetration test. Following the conclusions of the preliminary analysis performed in Chapter 3, the DEM calibration strategy described in Chapter 3.1 is kept in mind when designing this experiment. Thus, this chapter is composed of a description of the laboratory set-up in Section 4.1, results with the penetration resistance in Section 4.2 and a discussion and conclusion on the results in Section 4.3.

4.1. Laboratory test set-up

4.1.1. Penetration test set-up

For the design of this laboratory experiment, the author had in mind the idea to create a simple penetration test which can be the used for creating the equivalent DEM model. In other words, the idea behind creating the apparatus and the equipment is such that that it can be easily and accurately replicated using DEM. Moreover, other considerations such as time constraints and difficulty of performing the tests were also aspects taken into account when planning for the operations.

The experimental test aims to represent the industrial application of a steel pile penetrating through the scour protection. Due to space limitation and convenience, a small scale test in the laboratory was performed, similar that made by Deltares described in the previous preliminary analysis, Chapter 3. Therefore, the dimensions of the steel pile, domain and the rock armour were downsized. An open-ended cylindrical penetrating tool is found to be inapplicable to a small scale set-up composed of large rock material. As an alternative, the steel pile is represented by a vertical section of the pile, thus approximating it with a rectangular steel plate. This gives sufficient information about the vertical force needed for penetration, however it can be acknowledged that aspects such as plugging or arching described in Section 2.1.3 are impossible to capture using this rectangular plate.

Description of apparatus

The plan used to approach the design of this experimental set-up is to find already available equipment and material which can be used to perform the test. A workstation with a 20 tons hydropneumatic press is considered to be an adequate solution to push the plate into the granular material. The press can be operated pneumatically using a compressor, which allows a relatively constant downwards movement of the cylinder. A digital pressure gauge can output the penetration resistance, thus the force can be recorded for each time step (every second). No strain gauge is present in the set-up, so the penetration displacement will be calculated using image analysing processing tools, which will be explained later. The steel plate is welded to the cylinder and it imposes a vertical penetration using the

a guiding mechanism which has a low friction material in contact with the plate. The technical drawing with the components of the press can be found in Figure 4.1, while Figure 4.2 depicts the plate, the digital pressure gauge, the guiding mechanism, the pneumatic cylinder and the steel container with the rock material.
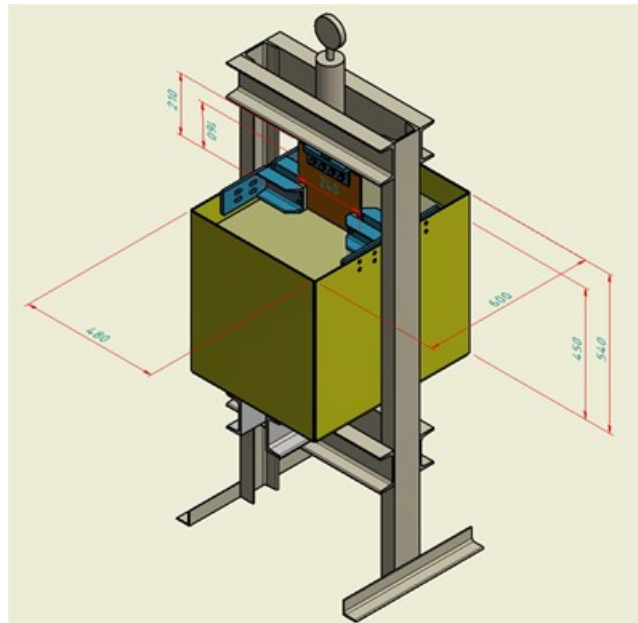
Figure 4.1: Engineering drawing of the laboratory test set-up of the hydrodynamic press, the plate and the container
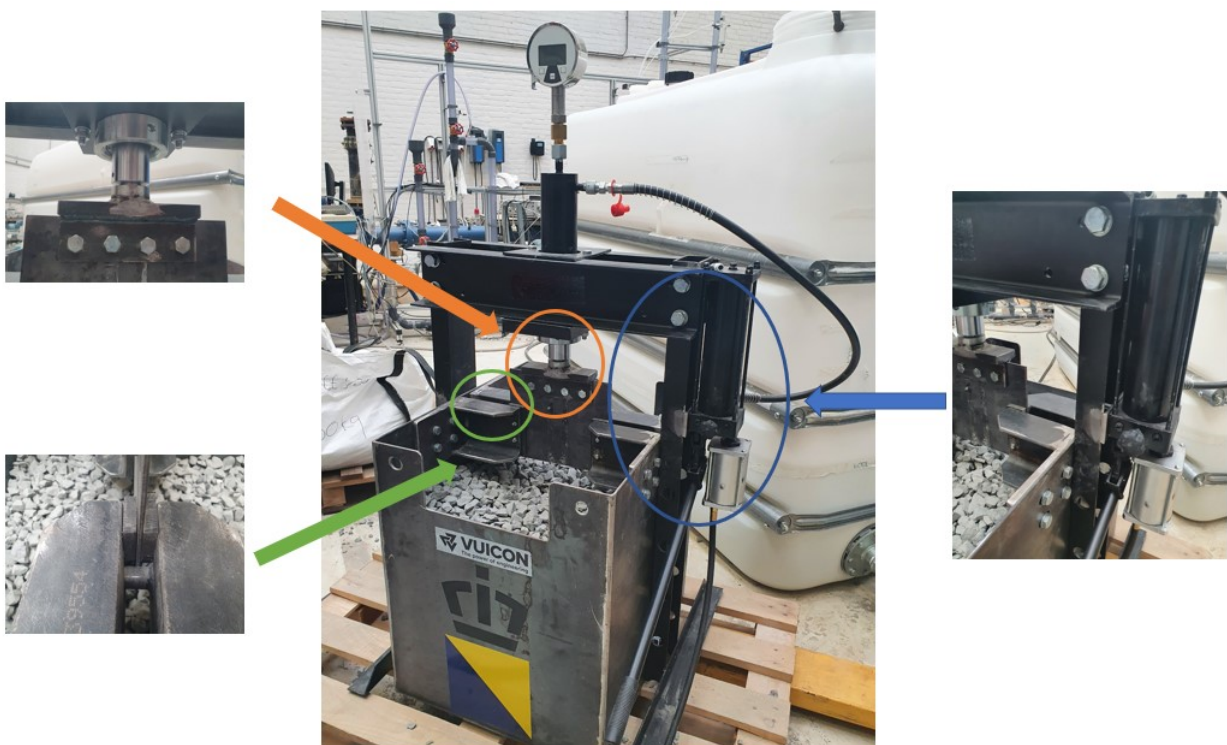
Figure 4.2: Picture of the hydrodynamic press used in the experimental lab work which shows the container filled with rock material

Scale model

Table 4.1 shows part of design process behind choosing a certain scaling factor (N) for the laboratory set-up. The scaling laws ware previously introduced in Section 3.1.3. The starting point of this plan is the availability of the material (d_{50} of 9.5, 12, 20, 30 mm), common width of the rectangular plate (every 0.5 mm) and real industrial thickness of the pile ($d_{50} * N$ is between 70 to 110 mm). As identified in Section 2.2.2, the size of the rock armour used in OWTs projects is somewhere in-between 100 and 500 mm, which gives desirable ratios of d_{50}/w of 1 to 6. In this research, the ratio of interest is between 2 to 8, such that an extreme limiting ratio is included. For the same reason, Table 4.1 only uses smaller possible width of the penetrating tool, such that the most extreme cases are considered. Lastly, another constraint of the design is the lateral extent of the press, which does not allow to use larger rock inside the container, as it will be explained later.

Table 4.1: Possible options for ratios of d_{50}/w taking into consideration the availability of material

Option no.	w (mm)	N (-)	$w * N$ (mm)	d_{50}/w			
				$d_{50}(mm)$			
				9.5	12	20	30
1	3.5	20	70	2.7	3.4	5.7	8.6
2*	4.0	20	80	2.4	3.0	5.0	7.5
3	4.5	16	72	2.1	2.7	4.4	6.7
4	5.0	16	80	1.9	2.4	4.0	6.0
5*	6.0	12	72	1.6	2.0	3.3	5.0
6	6.5	12	78	1.5	1.8	3.1	4.6
7	7.0	10	70	1.4	1.7	2.9	4.3
8	8.0	10	70	1.2	1.5	2.5	3.8

* Final design choice

Out of the 8 options presented in Table 4.1, the options which are chosen to best satisfy the indicated desired ratio d_{50}/w are options 2 and 5, since they also use different scaling factors. The most extreme case is represented by a ratio of d_{50}/w of 7.5, which is higher than the common ratio used for design in real OWTs design. Therefore, these ratios will be further investigated in this thesis.

Design of Experiments

The fragments of rocks used for this small scale lab tests are basalt and their aspect is irregular. Their high angularity makes every rock fragment very different from one another. For the same reason, an elaborate and exact PSD was difficult to construct since there were no available sieve sizes at the time of performing this experiment for this large angular rock fragments. However, for the purpose of determining the d_{50} of the rock, several samples of different shapes, texture and elongations were chosen as representative (the most commonly found shapes) and are being displayed in Figure 4.3. Therefore, the range of sizes of each set of rocks is included in Table 4.2. This represents the Design of experiments, so 8 sets of tests which are to be performed using the pneumatic press.

Table 4.2: Rock material size and plate thickness

	Set	Size
Basalt rock fragment	1	8-11mm, d_{50}=9.5 mm
	2	8-14mm, d_{50}=12 mm
	3	16-25mm, d_{50}=20 mm
	4	20-40mm, d_{50}=30 mm
Steel plate (w)	1	4 mm
	2	6 mm

Figure 4.3: Representative samples of the basalt rock fragments

Dimensions domain

Regarding the dimensions of the container, the technical drawing in Figure 4.1 shows the final design choice. As concluded from Chapter 3, one needs to find a container small enough to limit the amount of particle in the container, but also large enough to avoid as much as possible wall effects. In other words, the domain size is important when aiming to reproduce the exact same set-up in DEM without additional computational time. Thus, a trade-off between minimizing the DEM computational and reducing the wall effects needs to be made.

Section 2.4.1 pointed out that the majority of the authors defined the horizontal and vertical extent depending on the width of the penetrating tool (w). However, this thesis considers much larger particles than in previous research, thus it is proposed to have the domain extent as a function of the d_{50} of the rock. Moreover, a rectangular domain is considered more efficient when using a rectangular plate, thus the diameter of the domain D used by previous authors is now replaced by W_{dom} and L_{dom}. Therefore, Table 4.3 shows the rules applied to define the domain and the plate size. The multiplication factors used in this table make sure that that the plate penetrates a sufficient amount of particles, or that the boundary is at an adequate distance with respect to a minimum number of particles between the plate and the container wall. Moreover, the penetration depth z is constrained by the maximum stroke of the press cylinder.

Table 4.3: Domain and plate size design rules

		Rule	Value (cm)
Plate	w	see to Table 4.1	0.4 & 0.6
	l	8 * d_{50}	24
	h	1.4 * z	21
Domain	W_{dom}	20 * d_{50}	60
	L_{dom}	l + 8 * d_{50}	48
	H	z + 10 * d_{50}	45

Operational procedure

The penetration test is performed using a certain sequence of actions such that the force and the vertical displacement of the plate can be recorded. The steps for performing each repetition of the test are as follows:

1. Change rock fill material and fill up the container with material until the required level (the box is taller, however it needs to be filled until the design level). Make sure that the rocks do not touch the guiding mechanisms, that the plate is in the original position and that the bolts are tightened properly. Turn right the knob, such that pressure can build up.

2. Set up the Go-Pro camera in position to record the test. Make sure to plug the cable in the laptop and establish connection between the logging software and the digital pressure gauge.

3. Begin the test. Start first the camera recording since it has a small delay until the connection is established. Then, press in the same time start recording the force and the air compressor. The plate should now start moving downwards.

4. While the plate is penetrating, prepare on the computer to stop the penetration. Observe when the plate reaches the maximum depth using the physical ruler band placed on the plate. If this is the case, then release the air pressure by turning the knob to the left. The plate should go up now by itself.

5. When the plate is not in contact with the rock anymore, first stop the Go-Pro recording, then stop the log from the manometer. Download the force versus time data in a '.csv' format.

6. Repeat the sequence for a new test. Option to change as well the plate before filling the container.

As mentioned before, there is no specific equipment which records the penetration displacement. Thus, an alternative method was considered. Although the penetration can be also observed visually using the recorded video, a more accurate approach is to use a general purpose tracker. The code uses the Kanade Lucas Tomasi Tracker (KLT) algorithm and the computer vision toolbox of MATLAB which automatically and tracks the desired objects through the video (Muhammad, 2017). Figure 4.4 shows a picture with the penetration of the plate in the material, having one of the bolts as marker which moves in time. Knowing the frames per second of the video and establishing a reference system, the code gives the displacement per each second. By managing to synchronise the start and the end of the video recording with the data logger from the pressure gauge, then the force versus time data can be translated into force versus vertical displacement.

Figure 4.4: Video tracking tool applied for the penetration test, at the start (left), at the end (right)

4.1.2. Additional tests

A series of additional smaller tests are performed, such that they can aid the calibration of the DEM model. These procedure behind each of these tests is described in detail in this section. The tests were performed using rock material of the largest grain size ($d_{50} = 30mm$), because the same material is to be used in the reference case for the DEM model. A number of 5 tests were performed in the laboratory using already available equipment:

1. **5 liter cylinder test**: measures bulk density of the material. The test involves a steel container which is weighted before and after getting filled with the rock material, see Figure 4.5. The bulk density container is according to ISO 17828 and its volume is approximately 5 liters and it allows for the calculation of density as being the change in mass divided by the constant volume of the cylinder.

2. **Graduated water cylinder** : measures particle density. The procedure of this test is to fill up a cylinder with water and then add rocks. The change in mass divided by the volume change can be approximated as the particle density.

Figure 4.5: Bulk density container filled with rock material (left) and gradated water cylinder (right)

3. **Drop test**: measures bounce height, from which the restitution coefficient (e) can be calculated as the square root of the ratio bounced height over the height from which the rock is dropped. The procedure is that from the same height (60 cm), individual rock fragments are dropped and the bounce height is measured using a camera placed at the bottom. Since the impact is very short and fast, then the frames per second of each video needs to be high. During post process, the video is then slowed down, and using a ruler, the bounce height is approximated. Figure 4.6 shows two cases investigated, a drop test on a steel plate, from which the coefficient of restitution between particle and geometry ($e_{p,g}$) can be determined and a drop test on a pile of rocks which gives the coefficient of restitution between particles ($e_{p,p}$) .

Figure 4.6: Drop test on a plate (left), on a pile of rocks (right)

4. **Inclined surface tester**: measures the friction between particle and steel plate $\mu_{s,p-g}$. This test is performed by having the steel plate which is set and secured on a reclining surface and rock fragments placed on top slide. This happens when the plate reaches a certain inclination level, from which the tangent is calculated and the friction coefficient is approximated. Figure 4.7 shows the set-up of this test.

5. **Shear box and lifting cylinder test**: measure the angle of repose (α_{AoR}). This parameter is measured using two different procedures and the outcome is compared and discussed in a later section. First approach makes use of a shear of box, also referred to as a ledge test. The geometry involves a box in which one of the walls can be opened. The rocks are places inside the box and the door is opened, allowing the rocks to exit the box and forming a inclined shear surface. This can be considered the angle of repose of the material, as shown on the left picture in Figure 4.8. Moreover, the material which exits the box is weighted. Second method is the same as the one used by Deltares as descried in Chapter 3.2.1. A steel cylinder is filled with material, manually lifted with a approximately 1cm/s, allowing a pile of material to form on a horizontal surface. The AoR can be approximated from this pile, as shown on the right picture in Figure 4.8.

Figure 4.7: Inclined surface tester, side view (left) and top view (right)

Figure 4.8: Angle of repose tests: shear box with opened door (left) and lifted cylinder pile of material (right)

4.2. Results experiment

Penetration test

The results of the penetration test can be summarized in two graphs which plot the penetration pressure recorded by the manometer. The pressured are recorded in bars (see Appendix A for the detailed results), but for convenience they are translated into force by knowing the area of the cylinder which pushes the plate into the rock material (6 cm in diameter). The pressure is recorded using the procedure explained in the previous section, and then the average force is approximated for each case. Figures 4.9 and 4.10 show the average penetration resistance for each of the 4 sets presented in Table 4.2, in which the displayed force was measured using 5 repetitions for each thickness of the penetration tool which gives a satisfactory 95% confidence interval.

Apart from the graphical display of the force results, the experimental tests give the work required for which the plate penetrates the material. This response variable will be very useful for the purpose of DEM calibration. Since work is calculated as the product of force and distance, it considers the evolution of the penetration forces over time, rather than looking at the force at a discrete moment in time. The work at 0.14 m depth is presented for all 8 sets of tests in Table 4.4.

Penetration resistance w=6 mm
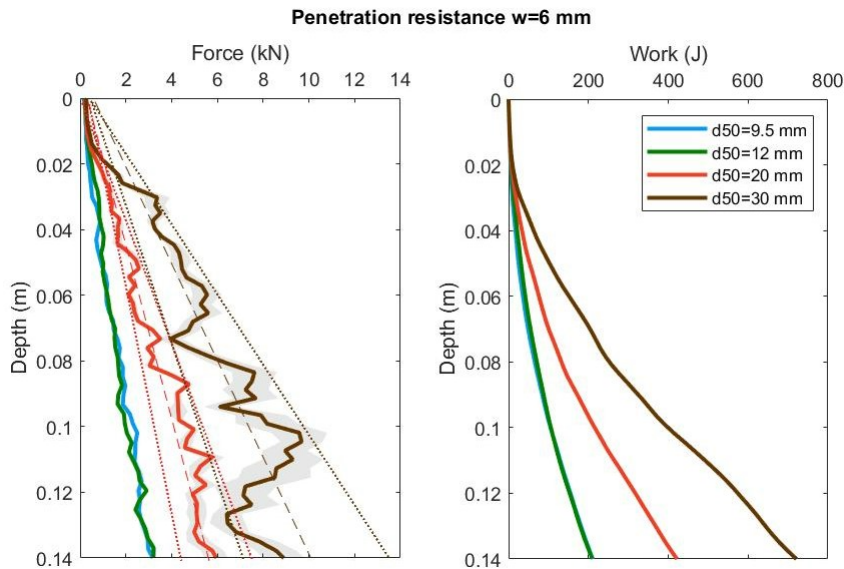
Figure 4.9: Penetration resistance for the case of plate width of $w = 6mm$

Penetration resistance w=4 mm
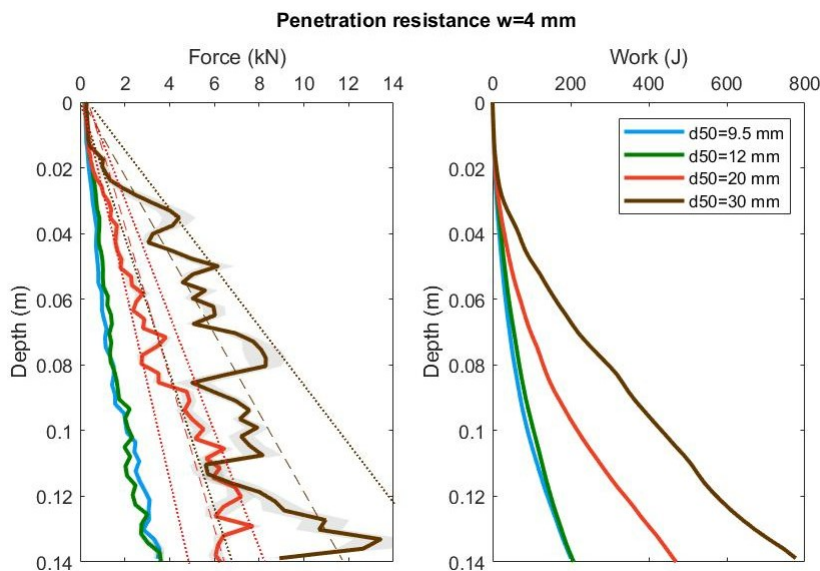
Figure 4.10: Penetration resistance for the case of plate width of $w = 4mm$

Table 4.4: Penetration work (J) calculated at 0.14 m depth in terms of d_{50} and w

	d_{50}=9.5 mm	d_{50}=12 mm	d_{50}=20 mm	d_{50}=30 mm
w=6 mm	211	209	425	726
w=4 mm	201	207	475	776

During the test, the rock fragments are displacing, however, the formed heave cannot be measured using reference points due to the non-apparent displacement of particle in the vertical direction. Fortunately, a technical equipment, the Intel® RealSense™ depth camera D435, allowed for the recording of the top surface elevation before and after the plate penetration. This camera uses a depth sensor to record the distance to an object with a range between 0.3 and 3 m, which is ideal for the purpose of this test set-up. The results are displayed in Figure 4.11, where the point cloud before and after the penetration is displayed. Keeping in mind that both the vertical and horizontal axis represent the location (in m), it can be seen that the particles near point A are pushed down with approximately 2 cm, and the heave next to point B is less than 1 cm.
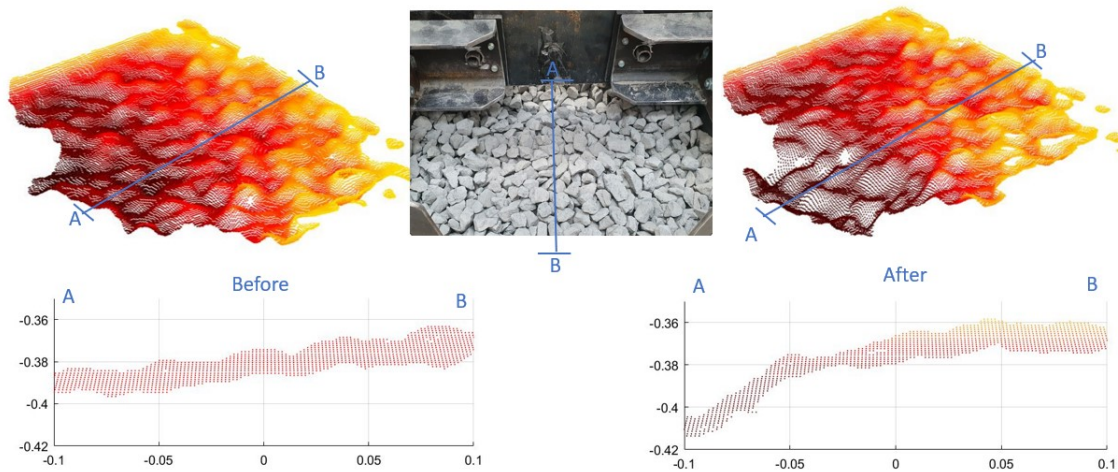
Figure 4.11: Cross-section through half of the container showing the initial surface profile of the rocks and the final elevation profile at the maximum penetration depth

Additional tests

Moreover, the results of the additional experimental tests can be found in Table 4.5. The complete set of experimental data can be found in Appendix B. These test are in essence simple tests, but can provide a valuable insight into the behaviour and properties of the material (for instance the micro-parameters required for the DEM calibration). Table 4.5 identifies the value for the bulk and particle density, coefficient of restitution between particle and between particles and geometry, as well as quantifies the static friction between particle and geometry. The porosity can be calculated as 51% using the bulk and particle densities. In addition, these additional tests give the approximated angle of repose of the material using two tests, the shear box and the lifting cylinder. A discussion on the results, reliability and accuracy of each of the test is inserted in Section 4.3.

Table 4.5: Results additional calibration tests

Parameter[a]	Notation[a]	Unit	Mean value	Confidence
Bulk density	ρ_{bulk}	kg/m^3	1500	40
Particle density	ρ_p	kg/m^3	3068	130
Coefficient of restitution p,g	$e_{p,g}$	-	0.15	0.015
Coefficient of restitution p,p	$e_{p,p}$	-	0.07	0.007
Coefficient of static friction	$\mu_{s,p,g}$	-	0.61	0.06
AoR (shear box)	α_{AoR}	deg	55.7	1.8
AoR (cylinder)	α_{AoR}	deg	35.1	2.8

[a] Particle (p) and Geometry (g)

4.3. Discussion and conclusion

4.3.1. Penetration test

The penetration test proved to be very useful for the purpose of providing an insight into the mechanisms and the limitations of the test. The small scale set-up aims to replicate a large scale set-up composed of a pile penetrating the armour rock layer for OWTs foundations. The properties of the steel plate are the same as those used for the monopiles, which makes the environment less conservative, since the forces are lower in this laboratory test. Therefore, any problems observed during the test can have large consequences in a real life scenarios. Therefore, several aspects needs to be mentioned about the outcome of the experimental test.

Plate buckle

A very important observation was made after performing the test with the thinnest plate and the largest rock size ($d_50 = 30mm$ and $w = 4mm$). The rectangular plate buckled during the test with approximately 5 mm deformation. The bend can be seen in Figure 4.12. There is no bending observed for the thicker plate. To be noted that the plate which buckled was not further used in other test set-ups and that the same thickness plate did not buckle with smaller rock sizes. Buckling indicates that the high stresses on the plate exceeded the strength of the plate and deformed it.

To explain this phenomena, a small calculation was made. The buckling load was calculated by simplifying the geometry to having a free end since the plate penetrates in the rock material as a free end. In this way, lateral resistance is neglected and the material resistance is considered equal to the applied force recorded by the manometer. Thus, using Euler's critical load formula shown in Equation 4.1 and the fact that the second moment of area can be calculated as $I = \frac{lz^3}{12}$, then a buckling load f_{crit} of 23.44 kN can be reached. By comparing the maximum load ever experienced during the test, 21.7 kN, these results are comparable in terms of the order of magnitude, which explains why the plate buckled during the most extreme load case.

Figure 4.12: Buckled plate during the most extreme loading case (left), abrasion marks on the plate (middle), breakage of rocks (right)

$$f_{crit} = \frac{\pi^2 EI}{4z^2}$$ (4.1)

Table 4.6: Parameters used in the Euler's critical load formula

Parameter	Notation	Units	Value
Young's Modulus steel	E_g	GPa	190
Second moment of area	I_g	mm^4	1280
Penetration depth	z	m	0.16
Length plate	l	m	0.24

Plate wear

In addition, scratches and wearing of the plates are observed for both plate thicknesses, as it can be identified in Figure 4.12. A small calculation was done using the theory of Brinell scale (Moore and Booth, 2015), in which a load (P) is applied to a steel ball (diameter of indenter is d_1) which leaves a circular indention (diameter of indention is d_2) on a horizontal surface. The hardness number (HB) can be calculated using the formula in Equation 4.2. By approximating the HB of the steel with 150 (-) (ASM, 2021) and considering the d_1 as being the penetration depth z and the diameter of the indention d_2 as the size of the wear zone (approximately 2 mm), then the applied load which causes the scratches is 4.6 kN. The forces recorded during any of the tests are higher than this force, thus this results can explain the heavy wear near the tip of the plate.

$$HB = \frac{P}{\frac{\pi d_2}{2} * (d_1 - \sqrt{d_1^2 - d_2^2})}$$ (4.2)

Particle breakage

Other observations which needs to be discussed refers to the breakage of rocks during the tests which consisted of the largest d_{50}. During penetration of the plates (any of the two widths), at larger depth, the set-up starts shaking due to high forces needed for the plate to break through the rock fragments. In other words, instead of pushing and displacing downwards the rocks next to the plate, it was observed that crushing of the rocks happens. In the event that the plate encounters a large rock, which is orientated perpendicular to the plate, the rock gets split into pieces, instead of being pushed to either side of the plate. This can also explain the little heave observed at the surface, since the porosity near and under the plate reduces as more smaller particles can fill in the voids.

The breakage was observed in the gap made by the plate after retraction as shown in Figure 4.12. The picture also depicts the proof of breakage since thin long rock pieces in the longitudinal direction can be observed at the bottom of the gap formed due to insertion of the plate. Lastly, it is worth mentioning that some breakage of smaller particles was observed as well, however this material can be displaced laterally much easier, thus less breakage was observed.

Moreover, a small calculation was made on the peak strength of the rocks. The interaction between the plate and the rocks can be approximated with a point load test. The formula to calculate the point load strength index test is included in Equation 4.3 (ISRM, 1985). Provided that during the most extreme case, forces P between 2 and 10 kN were experienced, and that the $d_{50} = 30mm$ normalised to a spherical rock sample with a diameter of 50 mm, then the calculated point load index $I_{s,50}$ is between 1.7 and 10.5 MPa. No point load testing was done for the sample used in this research, thus results of point load tests on basaltic rocks are taken from literature. For instance, Endait and Juneja (2014) shows that for a dry test, the recorded point load index is between 3.8 and 9 MPa. The calculated $I_{s,50}$ index falls in this range and brings an analytical reason why breakage of particles was experienced during the experimental tests.

$$I_{s,50} = \left(\frac{d_{50}}{50}\right)^{0.45} \frac{P}{d_{50}^2} \qquad (4.3)$$
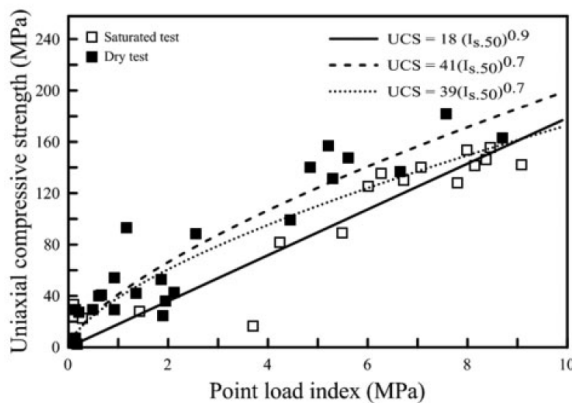
Figure 4.13: Point Load Index for basalt rock (Endait and Juneja, 2014)

Penetration resistance

The results of the actual penetration test needs to be further discussed. The graphs provided in Figures 4.9 and 4.10 show that the penetration resistance increases with increasing depth and with increasing size of the rock material. The confidence interval and the fluctuations of the graph is higher when larger rocks are used. This can be explained by the increasing amount of breakage described before: when encountering a rock, the force increases until it reaches the ultimate compressive strength of the rocks, the moment when it breaks and then the force reduces. The alternative to breaking is reorientation of the rocks while the plate penetrates which can also explain the fluctuating force. Moreover, one needs to emphasise that the size of the rock particle is the diving factor for the recorded force values, rather than the width of plate. The difference between two widths in the same material is relatively small

and can be governed by the variability of the material. However, the values of penetration resistance recorded for the biggest particle sizes are significantly larger than for the smaller sized particles.

In addition to this, one can conclude on the penetration force trend line from the experiments based on the ratios of d_{50}/w. Table 4.7 and Figure 4.14 display the results from both penetrating tools together and show that the force and the work required for penetration is generally higher with a larger ratio. The case with $d_{50}/w = 5$ is considered for both widths of the plate and the results show that at the same ratio, the larger width plate does 1.5 times more work than the thinner plate, which is an expected outcome.

Table 4.7: Penetration work (J) calculated at 0.14 m depth in terms of ratios d_{50}/w

d_{50}/w	1.6	2.0	2.4	3.0	3.3	5.0	7.5
Work (J)	211	209	201	207	425	475 or 726	776
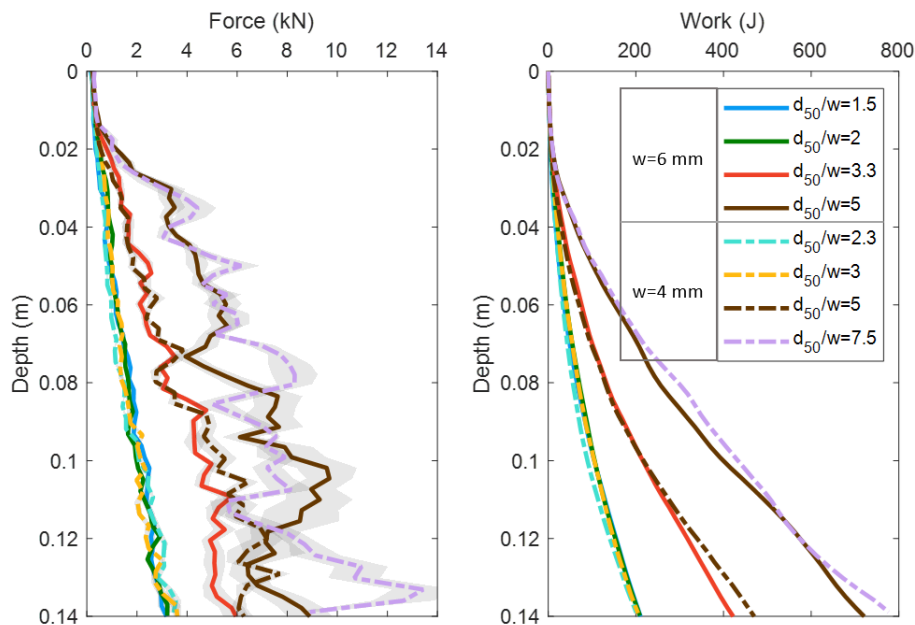
Figure 4.14: Results laboratory test displayed in terms of the ratio d_{50}/w

The results presented in Table 4.7 can be further interpreted such that a limiting ratio is established. Figure 4.15 plots the work values and shows that there is a transition between a lower and an upper regime of work. It is clear that the work increases rapidly when the ratio $d_{50/w}$ exceeds the value of 3 (-). Although a trend line can be constructed for the larger ratios, the penetration resistance is rather constant for ratios below 3. A non-linear dependency be thus concluded for the relation between the force and the ratio d_{50}/w. Therefore, by plotting the results in terms of their penetration resistance at maximum depth, one can identify the limiting factor which indicates that after this stage, the penetration is hindered and more force is required for penetration.
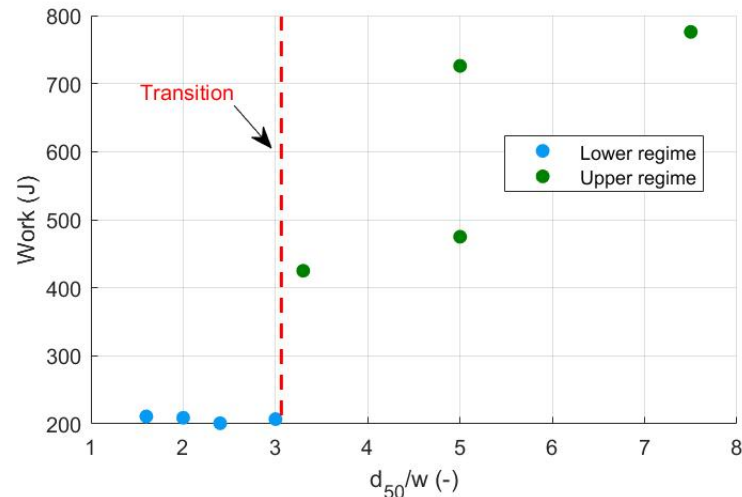
Figure 4.15: Fitted curve through the experimental results

4.3.2. Additional calibration tests

The results of the additional test can also be further interpreted, such that one can conclude on the accuracy, reliability with the purpose to use them to get the DEM model calibrated. A discussion and conclusions for each of the additional tests are as follows:

- The **bulk density** gives a porosity of the material of approximately 0.5 (-), with a range between 0.46 to 0.54 (-). This is similar to the bulk density and porosity measured using the material described in Section 3.2.1 for the preliminary analysis. However, in the previous analysis, it is unknown how the bulk density was calculated. For this test, a cylinder with the dimensions described in Section 4.1.2 was used. It can be observed that using the larger rock sizes, the quantity of material might be insufficient to reveal a realistic value for the voids between the rocks. In other words, the wall effect on the packing could be significant, however hard to estimate using this test procedure. Therefore, the bulk density test set-up and results shall used with precaution in the DEM calibration process.

- The **particle density** is calculated using the procedure described in Section 4.1 which gives a higher density value that the one used in preliminary analysis. The reason behind this is the fact that the material used for these experiments is basalt in contrast to granite as used in the previous research. Basalt is an extrusive rock which has a higher specific gravity due to the presence of mafic minerals, with heavy elements such as iron and magnesium (Jersey, 1997). The test however gives a reasonable value for the particle density, thus it can be used as a constant input for DEM calibration.

- **Coefficient of restitution** is determined experimentally using the drop test, which gives a relatively accurate indication of the value which can be used as input in the DEM model. Using numerous repetitions (up to 50 times) and using a camera which record the drop at higher frames per second, it is possible to approximate the bounce height of the rocks. It is clear that the rock bounces more on the steel surfaces, while when interacting with other rock material, the collision barely allows the rocks to bounce back. This experiment shows that the assumed value used for the preliminary analysis is correct, the coefficient of restitution needs to be low for this type of material, thus the results form this test can be used as constants in DEM calibration.

- The inclined surface tester gives reasonable values for the **static friction** between particles and plate. The test is considered successful since the rock fragments do not start rolling when the surface is inclined, but only slide, allowing for the static friction to be isolated from the rolling friction. The inclined surface tester could not approximate the static friction between two rock

particles, since there was no rock fragments sufficiently flat and large enough to act as a fixed surface from which another rock fragments can slide on top of it.

- The shear box or ledge test is a common calibration test performed to calculate the **AoR**, however, for the type of material used in this experimental test, it is found to be less appropriate. The box dimensions are relatively small in comparison to the size of the material used inside. In addition, there is a lot of friction between the particle and the boundary walls, such that when the door is opened, the material cannot escape without a light shake of the box. When using smaller size material, a common behaviour is that the material forms a steeper angle of repose next to the walls and then in the middle it flows easier, thus reducing the angle of the slope. This observation cannot be made for the rock material used in this test set up, since the boundaries are too close together relative to the d_{50} of the rock. Therefore, it can be concluded that the shear box is an inappropriate test to calculate the AoR of the chosen material.

- Lifting cylinder method is the same method which was used in the preliminary analysis. A major difference between the pile of material in Figure 3.8 and in Figure 4.8 is the quantity of material used. Even though the material type, the quantity and the size of the fragments are slightly different, the **AoR** is determined to be as well approximately 35 ^{o}. This is a lower value than expected for angular ingenuous rock material since Beakawi Al-Hashemi and Baghabra Al-Amoudi (2018) identify that the range for the AoR of crushed rock should be between 35 and 45 ^{o}. The large d_{50} in comparison to the scale of the model is not ideal to identify the AoR of the material, however, since a similar outcome was identified when using a larger domain (during the preliminary analysis), the experimental test is considered to provide adequate results and can be thus used for the purpose of DEM calibration.

.

<div style="text-align: right;">

5

</div>

<div style="text-align: right;">

Numerical model

</div>

In this chapter, the Discrete Element Method model of a penetration test in granular medium is presented. First, the calibration of the input parameters is described in Section 5.1. Then, the results of the Design of Experiments are inserted in Section 5.2. A discussion on how well the model is calibrated, verified and validated is included in Section 5.3. Lastly, a conclusion in Section 5.4 is drawn on the suitability of the calibration strategy for the design of the penetration test model involving a coarse granular medium.

5.1. Calibration analysis preparation

This section aims to create an overview on the approach behind conducting the Design of Experiments (DoE) for the calibration of a penetration test. Several lessons have been learned from performing the preliminary analysis (Chapter 3), but also from conducting the laboratory experiment (Chapter 4). For instance, the penetration of a plate into a granular medium is a good approximation for the full-scale model composed of a pile penetrating the rock armour layer. The self-weight penetration of the monopile can be also approximated with a constant velocity downwards motion which can then be implemented as the kinematics in the DEM model.

5.1.1. Plan of action

For calibration purposes, it is essential to keep as many parameters similar to the experiment. It is acknowledged that a trade-off between computation time and the similarity between the two models needs to be made, so some of the input parameters can be modified to a certain extent. However, it is wise to use the experimental results of some of the parameters presented in Section 4.2 also in the DEM model such that the source of uncertainty can be minimised. Therefore, the geometry, the particle sizes and the kinematics in the experimental test will be replicated in the DEM model. Nevertheless, it needs to be emphasised that the numerical model is just an approximation and a simplification of the real laboratory experimental set-up. So, aspects such as discontinuous plate penetration, irregular and random shape of the rock particles, crushing of the material but also buckling of the plate are not replicated in the DEM model.

Therefore, the DEM calibration in this thesis uses a multi-objective optimisation strategy, where more than one criteria have to be fulfilled simultaneously. In this case, due to the complexity of the problem, the penetration test could be insufficient to find a single set of parameters ($X = x_i, ..., x_N$) which would give a satisfactory calibrated solution ($X^* = x_i^*, ..., x_N^*$). If that is the case, then the angle of repose test can be used to find the definitive solution, by allowing the comparison of the bulk behaviour in two DEM

models ($Y^* = y_1^*, ..., y_N^*$) with behaviour from two laboratory experiments ($Y = y_1, ..., y_N$). Moreover, an additional test, the bulk density may be used as a validation of the suitability of this optimised set of parameters. This multi-optimisation process can be visualised using the flowchart in Figure 5.1.

Therefore, the plan of action consists of performing a DoE in order to calibrate the input parameters of the DEM penetration model. Therefore, only one of the 8 case studies performed in the laboratory (see Table 4.2) is used as the reference case for calibration purposes. For computational reasons, the largest rock size, $d_{50} = 30mm$, is used for the particle size and the width of the penetrating plate is chosen as $w = 6mm$.
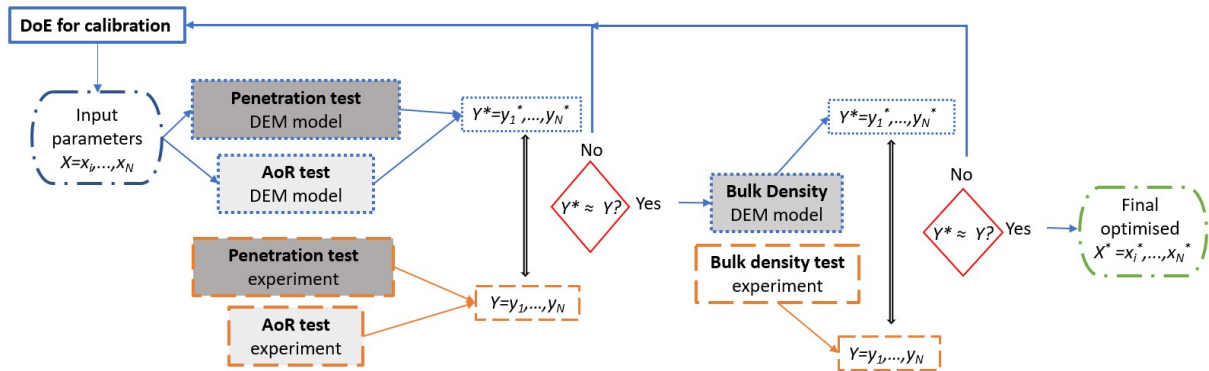
Figure 5.1: Flowchart showing the DEM multi-objective calibration process

5.1.2. DEM penetration test set-up

Similar to the experimental test set-up, this penetration test uses a rectangular container where the rock particles can be generated. Moreover, a rectangular plate slowly penetrates with a constant speed into the granular material. The DEM penetration model set-up and penetration process can be visualised in Figure 5.2.

From the preliminary analysis, one on the main conclusions of the study was that it is important to keep the same domain as in the experimental model, otherwise the results of the penetration test from both the experimental and the numerical model cannot be quantitatively compared. Therefore, this DEM penetration model uses the same definition of distance to the boundary walls and dimensions of the geometries as previously inserted in Section 4.1.1.
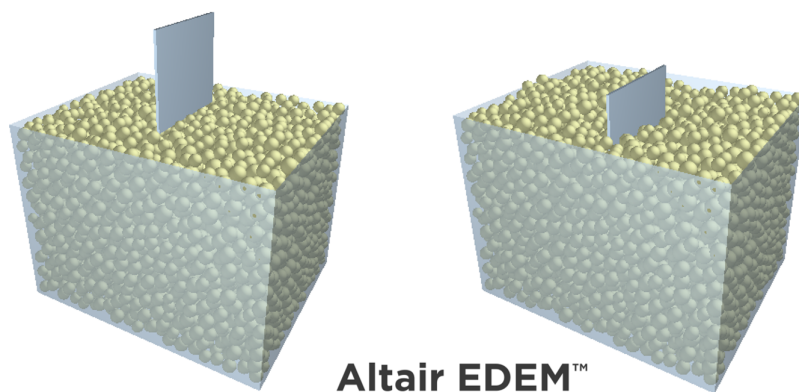
Figure 5.2: DEM penetration test set-up showing the initial conditions (left) and final stage (right)

Moreover, also in the topic of test set-up, the penetration velocity needs to be mentioned. Preliminary analysis showed that the penetration resistance is dependent on the penetration velocity. Therefore, in order to use the results from an experimental test, the plate needs to be pushed down at the same rate. Fortunately, the pneumatic press in the experimental test allowed for a more constant penetration that

manually using the hydraulics of the press. Consequently, the penetration velocity in the simulation is taken as the average penetration velocity in the experiment, which is equal to $v = 2.5mm/s$.

5.1.3. Additional DEM model

The second additional test which can be modelled in DEM to aid the calibration process is the angle of repose test. The AoR is an important parameter which can be used as KPI since it characterises the flow capabilities of the material. As previously explained in Section 3.2.1, different tests for the angle of repose can be performed, and their outcome differs because of the different kinetic energies produced in each test.

For the experimental test, two different tests were conducted and the results were included in Section 4.2. For the purpose of this calibration analysis, only one test is considered, and the choice of the lifting cylinder test was made by recognising two important drawbacks of the shear box test:

- As discussed in Section 4.3, the shear box shows clear wall effects during the experiment because of the small ratio between the d_{50} of the rock and the dimensions of the box. Moreover, it was observed that the material would not flow outside without a light shake, kinematic which can be also modelled in DEM. However, the amount of force required to make the particle displace and flow freely is hard to estimate, which could become a significant source of error in the calibration process.

- When performing an initial set of DEM simulations with this shear box model, it is observed that when choosing high static and rolling friction between particles, the particles do not exit the box, but rather form a very steep (almost vertical) slope when the door is opened, as it can be seen in Figure 5.3. Thus, the wall effects are also well captured in DEM model since due to the interaction of particles with the geometry, there is limited free fall outside the container. Nonetheless, for the purpose of comparing the response variable (α_{AoR}), this test is inappropriate for DEM modelling since no slope can be calculated for the remaining material in the box.
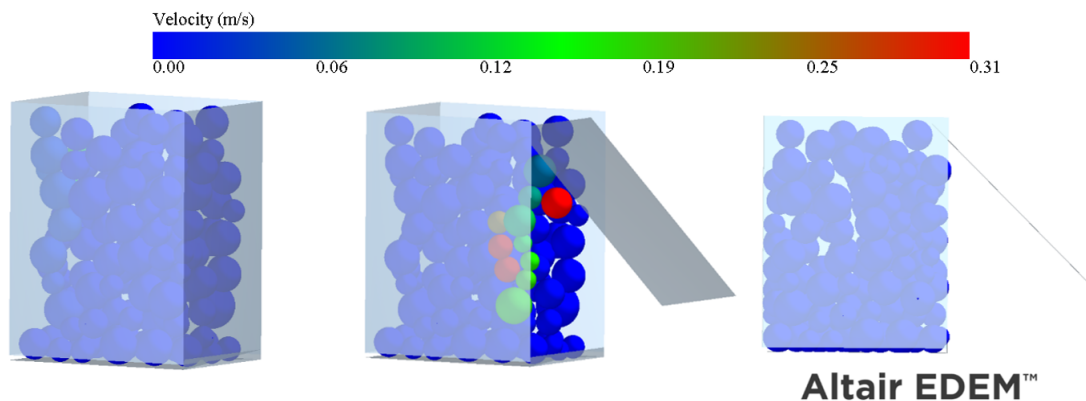
Figure 5.3: DEM shear box model showing: initial fill of the box (left), particles exiting after the door is opened (middle), side-view with the particles remaining in the box at the end of the test (right)

Thus, the additional test which provides with the necessary AoR to be used for calibration process is the lifting a cylinder, a test in which material is allowed to form a pile on a horizontal surface by lifting upwards a cylinder at a constant rate. The dimensions of the cylinder are the same as in the experimental test (see Section 4.1.2). The preliminary analysis showed the dependence of the lifting speed on the response variable, thus the same speed from the experimental test is used in this DEM model ($v_{AoR} = 0.01m/s$). The method used to generate the α_{AoR} is the same was previously defined in Section 3.1.4 and later implemented in the case study during the preliminary analysis.

In addition to the response variable the angle of repose α_{AoR}, the bulk density can also be one of KPIs of the system. Fortunately, the same cylinder was used for the purpose of establishing the porosity of

the material. Thus, the bulk porosity in the DEM model can be checked after the particles are generated (before starting to lift of the cylinder), so it is not necessary to create a separate DEM model. Thus, if required, the lifting cylinder test model can provide with 2 KPIs, the AoR and the voidage.

5.1.4. Particle definition and generation

The shape of the particles is a topic previously emphasised in Section 3.1.4. The DoE matrix previously constructed for the preliminary analysis in Table 3.7 uses different shapes of the particles such that the influence of the shape on the penetration resistance can be compared. This calibration approach was never completed due to previously mentioned considerations, however using this new set-up, it is possible to perform simulations with different shapes of particles.

Thus, 4 shapes are to be examined in this research. Figure 5.4 shows the sphere which has the $d_{50} = 2 * R$ of the material used in the laboratory experiments. The other shapes are designed using volume equivalence approach. This technique was preferred because the equivalent radius approach could not be applied to tetrahedral. The polyhedrons are thus created by considering the radius of a base circle (R) from which the height (H) of the 4th vertex is created. Tetrahedral is considered as the most simple, but also the most representative polyhedral shape for the rock fragments presented in Figure 4.3. In addition, 2-sphere is chosen to see the influence of increasing the particle complexity without increasing too much the computation time, while 4-sphere is chosen to resemble the most the shape of tetrahedrons.
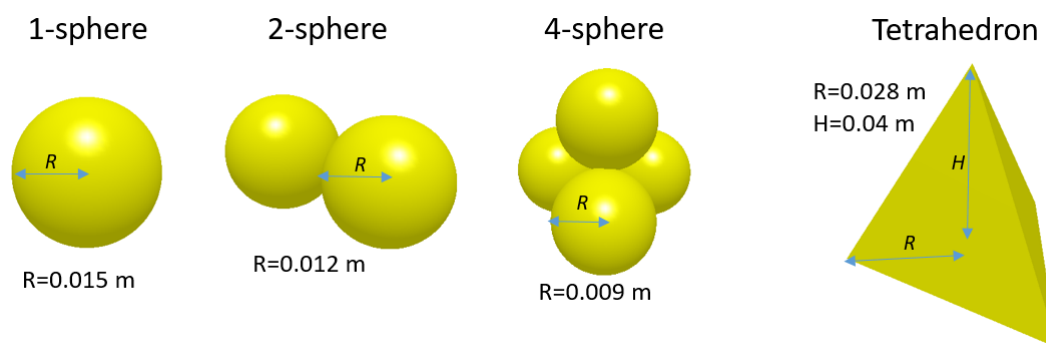
Figure 5.4: Shapes of particles used in penetration and AoR DEM models, the radius R is calculated for the reference case with $d_{50} = 30mm$

Depending on the input parameters and the shape of the particles, the container can be filled with various amount of particles. Therefore, it is wise to use the same technique to generate the particle such it can be consistently followed in all the models performed for the purpose of DoE. A dynamic factory (first introduced in Section 3.1.3) is considered the most applicable generation method for the particles, since it can control rigorously the amount and the rate of particles which are generated by the factory.

The procedure is such that first, the maximum mass of particles which can be generated in the container is identified for each case scenario. Then, the generation rate is set such that all that mass can be generated within 2 seconds, after which no particles are further produced by the factory. The factory generates particles with sizes which follow a normal distribution with standard deviation of 0.2. Next, the particles are allowed to settle until the kinetic energy of the material is significantly reduced.

Moreover, it is observed that the timestep needs to be small during the particle generation due to their higher kinetic energy. It is concluded that for a penetration tests, a constant 20% timestep gives stable results and the behaviour of the particle is realistic. In addition, unstable simulations are made when generating the particles with this time-step when enabling the GPU simulator engine. Thus, the solution found is to use the CPU capabilities during particle generation (e.g. until 2 s), then enable the GPU for faster calculation.

5.1.5. Material properties

For both the penetration test but also for the AoR test, the material used for these DEM simulations needs to be specified. Table 5.1 shows the DEM parameters which are to be further used. In terms of material used for the geometry, the common properties of steel are used, which are the same values as previously used the preliminary analysis. However, the choice of material properties for the rock bed used in the numerical model needs to be further elaborated. The origin of the particle and interaction properties values displayed in Table 5.1 is as follows:

- **Experimental laboratory test**: As presented in Chapter 4, additional tests were performed with the purpose to aid the calibration of the DEM model. In particular, the tests provided with a representative value for particle density ρ_p, restitution coefficient between particles $e_{p,p}$ and between particle and geometry $e_{p,g}$, as well as coefficient of static friction between particle and geometry $\mu_{p,g}$.

- **Literature analysis**: The majority of the values which are considered constant are taken from specialised literature (see Section 3.1). These values were also used in the preliminary analysis and they refer to the properties of the geometry, such as density ρ_g, shear modulus G_g, Poisson's ratios ν_p, and μ_g and the coefficient of rolling friction between particles and geometry $\mu_{r,p-g}$

- **Sensitivity study**: Preliminary analysis identified the importance of the shear modulus between the particles on the KPIs of the system but also on the computational time. Therefore it is found that the G_p can be reduced to a certain extent without significant implications on the response variable. Thus, a value of $1GPa$ is considered a good trade-off between the response of the system and the computational time, thus it will be further used as the particle shear modulus in every penetration test model. However, it needs to be acknowledged that the penetration resistance may be slightly underestimated, as concluded after performing the sensitivity analysis in Section 3.2.

Table 5.1: DOE parameters: input constants and independent variables

Characteristic	Notation[a]	Unit	Value DEM
Particle			
Density	ρ_p	kg/m^3	3068
Shear Modulus	G_p	GPa	1
Poisson's Ratio	ν_p	-	0.25
Geometry			
Density	ρ_g	kg/m^3	8050
Shear Modulus	G_g	GPa	80
Poisson's Ratio	ν_g	-	0.27
Interaction particle-particle			
Coefficient of restitution	$e_{p,p}$	-	0.15
Coefficient of static friction	$\mu_{s,p-p}$	-	0.1,0.5,0.9
Coefficient of rolling friction	$\mu_{r,p-p}$	-	0.01,0.4,0.8
Interaction particle-geometry			
Coefficient of restitution	$e_{p,g}$	-	0.07
Coefficient of static friction	$\mu_{s,p-g}$	-	0.6
Coefficient of rolling friction	$\mu_{r,p-g}$	-	0.5

[a] Particle (p) and Geometry (g)

5.1.6. DoE design

Section 5.1.5 explained the decision behind choosing most of the parameters in Table 5.1. However, there are two variable which are to be further calibrated, the static and rolling friction between particles ($\mu_{s,p-p}$ and $\mu_{r,p-p}$). The same DoE matrix as previously presented in Table 3.7 during the preliminary analysis is to be used in this calibration study, however one needs to check whether the rolling friction influences in any way the response variables also in the case of non-spherical particles.

Thus, for both multi-spheres and polyhedrons particles, a Full Factorial Design (FFD) (introduced in Section 3.1.4) is conducted. The shape of the particle becomes a categorical factor and the static and rolling friction make for two continuous factors with 3 levels. Therefore, DoE matrix can be written as shown in Table 5.2 and it is applied to all shapes, the 1-sphere, 2-sphere, 4-sphere and tetrahedron. The DoE is conducted for both tests, the penetration and the AoR test and the response variables can be added as supplementary columns to Table 5.2.

Table 5.2: DOE design matrix for all particle shapes

	Order DoE	$\mu_{s,p-p}$ (-)	$\mu_{r,p-p}$ (-)
	1	0.1	0.01
	2	0.1	0.4
	3	0.1	0.8
Spheres & Multi-spheres	4	0.5	0.01
& Polyhedrons	5	0.5	0.4
	6	0.5	0.8
	7	0.9	0.01
	8	0.9	0.4
	9	0.9	0.8

5.2. Results calibration analysis

The DEM simulations performed in this chapter were done using EDEM 2021 version of the software which allows for polyhedrons and GPU integration. As one of the conclusion of the preliminary analysis, the computer capabilities are very important when performing DEM simulations, so a more powerful computer was used for providing the main results of this thesis. In particular, a workstation with Intel(R) Xeon(R) W-2275 CPU @ 3.3GHz(28 CPUs) with a memory of 16 GB RAM is used which also has a Graphical Interface Unit (GPU) NVIDIA Quadro GV100, a professional-grade video card specialised for the field of design and visualisation, such as 3D modelling and animation.

In EDEM, the polyhedrons require the use of a GPU with CUDA cores, however the use of GPU for multi-spheres does not necessary lead to a speed-up of the computational time. According to EDEM (2021a), only after 10k particles, the GPU becomes effective for single and multi-sphere. This aspect was also checked during this research and it was confirmed that indeed only when using particles over 100k, one can see a considerable speed-up of computation time (somewhere in the order 5x less than running only using a CPU only). One needs to mention here that the amount of processors cores is also very important and that this allows the CPU based computations to be also very fast.

For instance, the simulation time of a penetration test is 62 s and the chosen timestep is 20%. Then, for 4 sizes of particles (single-sphere) generated with a normal standard deviation of 0.2, then the computation time is as included in Table 5.3. The case with 15k particles did not create a significant speed-up if GPU option is activated, however closer to the benchmark 100k, then the use of GPU becomes extremely relevant.

Table 5.3: DEM computation time of a penetration test model

d_{50}	30 mm	20 mm	12 mm	9.5mm
No. particles	5k	15k	70k	144k
Computation time	3h	7h	15h	27h
Processing Unit	CPU	CPU	CPU & GPU	CPU & GPU

Penetration test

The results of the DoE conducted for calibration purposes are included in this section. For the penetration test, the penetration resistance is recorded at each time step, making it possible to plot the resistance versus penetration depth for each combination of factors in the DoE (order DoE refers to the order presented in Table 5.2). For instance, for the 8th case in the DoE, penetration force and the work required can be plotted for all 4 particle shapes investigated in this research as shown in Figure 5.5, where all the input parameters are the same apart from the shape of particles. It is clear from the plot that the force required for the plate to penetrate a material made out of spherical particles in much larger than for more complex shapes. This aspect will be later investigated during the discussion section. All the other plots which include the penetration resistance at each different case of DoE are included in Appendix C for reference.
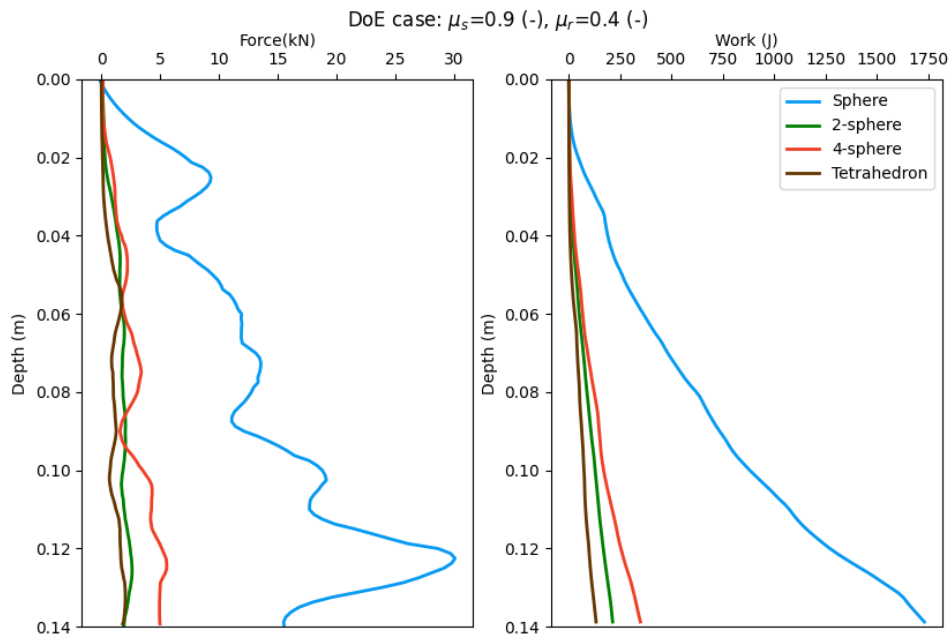
Figure 5.5: Penetration resistance comparison different shapes for DoE case 8

Figure 5.6 shows in a concise way all the results of the penetration test at each entry of the DoE in terms of the work needed for penetration at 0.14 m. Each simulation is run twice for each new set of input parameters and their average is included here. The exact numerical results and the percentage error to each case is included in Appendix C. Also shown in graph presented in Figure 5.6, it can be clearly seen that the only case which is close to the experimental work value (726 J) is the one for 1-spheres. This lack of correlation for other shapes will be discussed in Section 5.3.
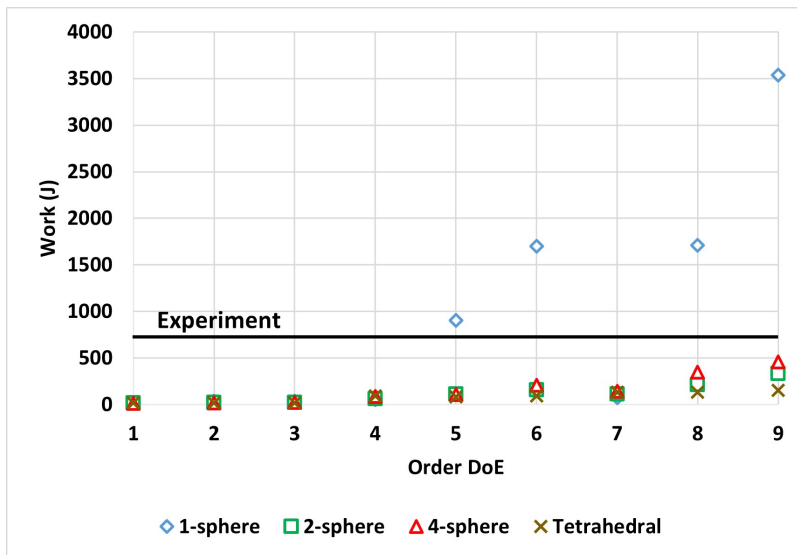
Figure 5.6: Results DoE for the penetration test

Additional test

As previously explained, an additional test was performed, the lifting cylinder test which provides with the value for the angle of repose as a second KPI. The same exact combination of input parameters are used in this test and the order of DoE is the same one as inserted in Table 5.2. The results of the AoR test is also presented in the form of a singular graph, as inserted in Figure 5.7. The angle from the experiments (35^0) is reached in some cases. In comparison to the results of the penetration test, the percentage error to the target value is smaller in many cases at every single categorical variable. The exact numerical values for this DoE are included in Appendix C as well.
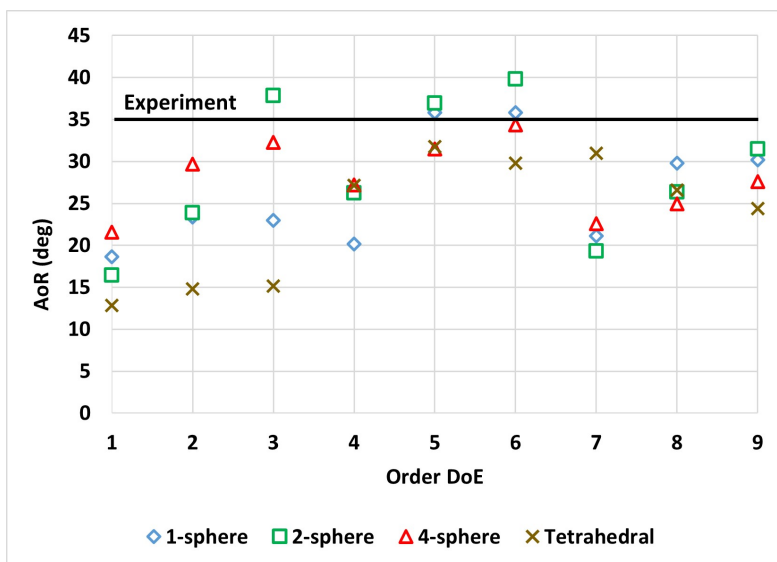
Figure 5.7: Results DoE for the angle of repose test

5.3. Discussion on the results of the DoE analysis

5.3.1. DoE results

The results presented in Figure 5.6 need to be further discussed since it is clear that in the case of multi-sphere and tetrahedrons, the magnitude of the force and work does not reach the experimental value. Although an increasing trend of higher force is recorded when the static and rolling friction are increased, the simulation results do not show a strong correlation with the experimental results. The reason behind this lack of correlation is to be further investigated in Section 5.3.2.

With respect to the results of the angle of repose test, one would expect that by increasing the static and rolling friction, the AoR would increase with it. However, the results identify that the highest response is not found while inputting the largest value of static and rolling friction, as previously depicted in Figure 5.7. Moreover, as concluded before in Section 4.3, the lifting cylinder method gives less accurate results since the ratio of the particle size to the scale of the cylinder is very small. In other words, in order to have a more evident angle of the pile, the amount of particles for the reference case should have been much larger. In addition to this, the measurement of the angle becomes difficult when no clear slope of the pile is formed. For this reason, the method of the fitting cone is used for the results of the DEM model, however, this technique considers the d_{50} of the particles, which, especially for the tetrahedrons, it is hard to estimate due to their irregular shape, see Figure 5.8. Both of the measures, the AoR from the experiment and from the DEM model are subject to inaccuracies, thus this additional test needs to be cautiously used during decision making stage of the calibration process.
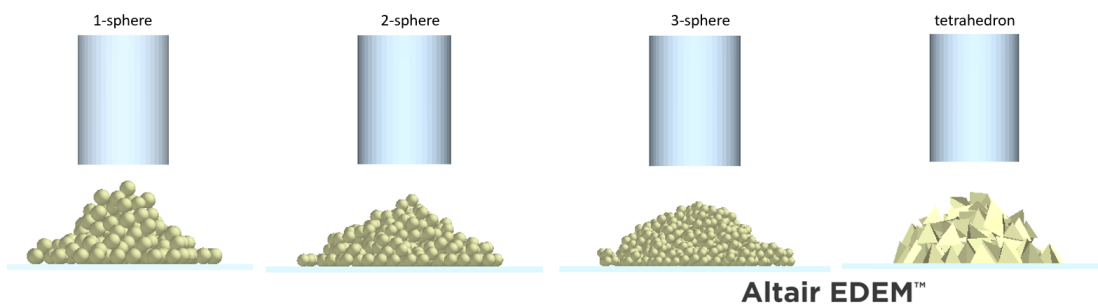
Figure 5.8: DOE case 8: AoR test with different shapes of particles

The results of the DoE simulations are plotted such that one can combine the results form the penetration test with the AoR and find the the optimised set of input parameters which give the desired response variable, as shown in Figure 5.9. For the reference case with $d_{50} = 30$mm and the width of the plate of $w = 6mm$, contour plots are created for all the shapes by plotting the work using cubic interpolation and the AoR by linearly interpolating the results.

The experimental results give a work at 0.14 m depth of 726 J and an AoR of approximately 35°. This combination can be achieved only for spherical particles since the results of the 2-sphere, 4-sphere and tetrahedrons cases give too low of a penetration resistance. Subsequently, focusing on the results of spherical particles, the first contour plot in Figure 5.9 indicates that there is a possible combination of the input parameters which could give the desired response variable. DoE entry 5 results correlate reasonably close to the expected bulk response provided by the experimental tests, therefore, no further interpolation between the DEM results is considered necessary. The final optimised calibration set of parameters for the spherical particles which is used for further verification and validation is:

$$\mu_{s_p,p} = 0.5 \ \& \ \mu_{r_p,p} = 0.4$$

Figure 5.9: Colour plot with the results from the DoE presented in the form of work at 0.14 m depth and AoR

5.3.2. Investigation on the results of non-spherical shapes

As discussed in the previous section, the results involving non-spherical particle shape show lower penetration resistance than expected. This section aims to investigate the possible causes of this outcome by investigating the inner workings of DEM algorithm and the micro behaviour between the particle during the penetration test.

The first aspect to discuss is the importance of particle size in calculating the displacement and velocities in DEM. This ultimately governs the forces which are calculated at each time step. Therefore, the first possible explanation for lower calculated forces for the multi-sphere and polyhedrons is based on how the particle were generated. As mentioned before, equivalent volume method is used to create the size of the non-spherical particles, such that the tetrahedrons can also be equivalently created. However, this method implies that the actual diameter of the particle is slightly different from the original spherical one. This slight difference in d_{50} of the particle is thus the first argument for which the calculated forces in the penetration model are lower.

Moreover, another explanation which could indicate why the calibrated set of input parameters is not appropriate to be used for more complex shapes reinstates that during the sensitivity analysis in Section 3.2, it was established that shear modulus can be reduced to a value of $1GPa$ without having a large influence on the penetration resistance. However, this analysis used spherical particles, so the conclusion might not be applicable to particles such as tetrahedrons. The tetrahedrons are interacting differently from the spherical particles, so a more extensive analysis into the coordination number, porosity of the material, overlap and stresses could also explain the difference in results.

Coordination number

The coordination number represents the total number of contacts per particle. Thus, this parameters can be used in any DEM model to quantify the particle accumulation. From Table 5.4, the coordination number increases with the complexity of the particle shape. This can be explained for instance in multi-sphere, since there are more options for two particles to create a contact point as they are composed of multiple spheres which can each be a contact point. With respect to the tetrahedral shape, a variety of contact points can be mentioned, for instance face to face, face to edge, edge to edge which can explain why the coordination number of tetrahedrons is higher than for multi-spheres. Moreover, Figure 5.10 shows the average coordination number in the whole domain, which is relatively constant throughout the penetration, with a slight decrease in time regardless of the shape of the particles. This is because the coordination number does not include the contacts between the particle and the geometry, thus the more the plate penetrates, the more the particles start to interact with the plate and not between each other.

Table 5.4: Comparison entry 8 of the DoE matrix for various parameters

Parameter	Sphere	2-sphere	4-sphere	Tetrahedron
(Cylinder test) Porosity (%)	45.8	50.4	53.5	54.5
(Penetration test) Porosity (%)	45.9	46.7	52.7	53.1
(Average) Coordination number (-)	3.3	4.1	4.4	4.8
(Average) Overlap (%)	0.18	0.04	0.05	0.24

Porosity

Furthermore, one needs to relate this coordination number to the overall behaviour of the material of the material during the penetration test by looking at the bulk porosity under the plate (not the entire domain is considered due to the formation of the gap as shown in Figure 5.13 which decreases the overall porosity). Using the same configuration of input parameters, a material composed of tetrahedral particles or 4-spheres has more voids than one with spheres, see Figure 5.10. This is counter-intuitive since increasing the particle shape complexity should decrease the voids between particles. However, this can be justified by the factory generation algorithm used by EDEM. Even though the same PSD is inputted, the algorithm finds it easier to fill in empty spaces during the generation stage with smaller size perfect spherical particles, rather than with more complex shapes. If tetrahedrons are taken for example, the factory would not be able to fit a angular shape in a empty space since it requires rotating the shape to find the direction which fits perfectly the empty space. This has to be done is a certain amounts of tries to place each particles, otherwise if no possibility is found, the factory moves to another timestep. Thus, less smaller particles are generated due to this overrun of trials, so more voids are created, which increases the overall porosity of the material.

Particle overlap

Last graph in Figure 5.10 indicates the evolution of the average overlap in the penetration test during the entire penetration of the plate in the granular material. As explained during Section 2.3, EDEM uses a soft-sphere method which allows for small overlaps between particles, from which the magnitudes of the forces acting on particles are calculated. The overlap distance is presented here as a percentage of the particle radius. In terms of magnitude of the overlap, Cleary (2010) identified that the 0.1–0.5% are required to ensure that the flow behaviour is not dependent on the stiffness of the particles. Therefore, a value over 0.5% would indicate an excessive compressibility of the particles, which could be unrealistic.

In the chosen DoE example results, it can be seen that the sphere overlap increases in time, although the fluctuations are very large. On the other hand, the multi-sphere particles have a limited overlap which is less than the indicated acceptable range. The little overlap of the multi-spheres could explain the results of low penetration force recorded at the interacting with the penetrating plate. On the other hand, tetrahedrons overlap the most. The high overlap of tetrahedrons and the low forces recorded in

this material can be explained by acknowledging that the overlap volume between spheres should be actually compared to that of polyhedrons and not the overlap distance. The overlap of polyhedron is called depth penetration, since their vertexes and edges get in contact during interaction. The higher overlap between tetrahedrons can be explained due to the method of creation of these particles, which is the equivalent volume method. Thus, when two tetrahedrons come into contact, their vertex needs to penetrate further into the other particle for the same equivalent overlap volume.
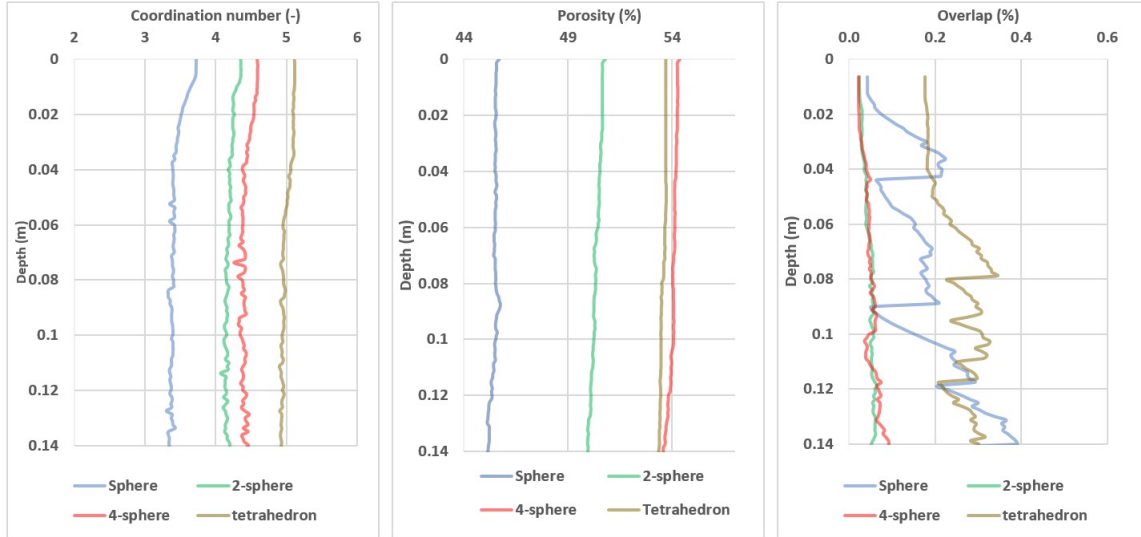
Figure 5.10: DoE case 8: Coordination number (left), porosity (middle) and overlap (right)

Particle stresses

One can also look into the stresses on the particles at the bottom of the plate. A small volume is considered under the tip of the pile at the maximum penetration depth for comparison. The choice of this region is based on having enough particles in the horizontal and vertical direction, such that a picture of the stresses can be created (in other words, at least 3 spheres are considered left, right and under the bottom of the plate).

Contour plots are created using the values of the Von Mises stresses recorded at final time (a 3D plot with the coordinates the location of particles points is rotated such that one looks at a horizontal plane), as shown in 5.12. The x-axis and y-axis identify the location of the plate (the black rectangle) with respect to the position of stress concentrations. Von Misses stresses are calculated using the formula in Equation 5.1, which uses the definition of the stress tensor in Figure 5.11.

$$\sigma_{VonMises} = \sqrt{\frac{1}{2}[(\sigma_{xx} - \sigma_{yy})^2 + (\sigma_{yy} - \sigma_{zz})^2 + (\sigma_{zz} - \sigma_{xx})^2 + 6(\sigma_{yz}^2 + \sigma_{zx}^2 + \sigma_{xy}^2)]} \qquad (5.1)$$

From Figure 5.12, it can be seen that the maximum stresses for spheres reach a value of 2 up to 10 times the values for multi-sphere and tetrahedrons. This higher stress regime is the explanation why for the spheres, higher penetration forces are recorded. Moreover, the location of the stress accumulation is significant. For spheres and multi-spheres, the stress accumulates closer to the pile (under or just immediately under next to the pile), however, in tetrahedrons it is further away from the pile penetration trajectory. This low tetrahedral particle stresses below the tip of the pile (approximately 50 kPa) is a source of the lower recorded penetration forces of the plate.
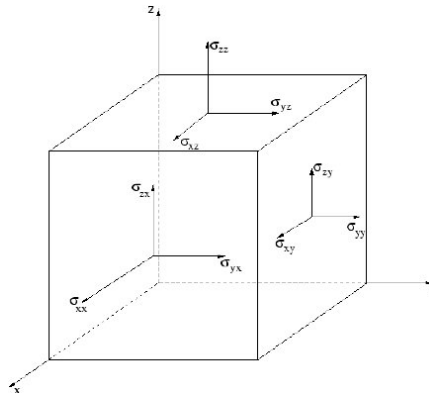
Figure 5.11: Stress tensor definition (Nermoen, 2010)
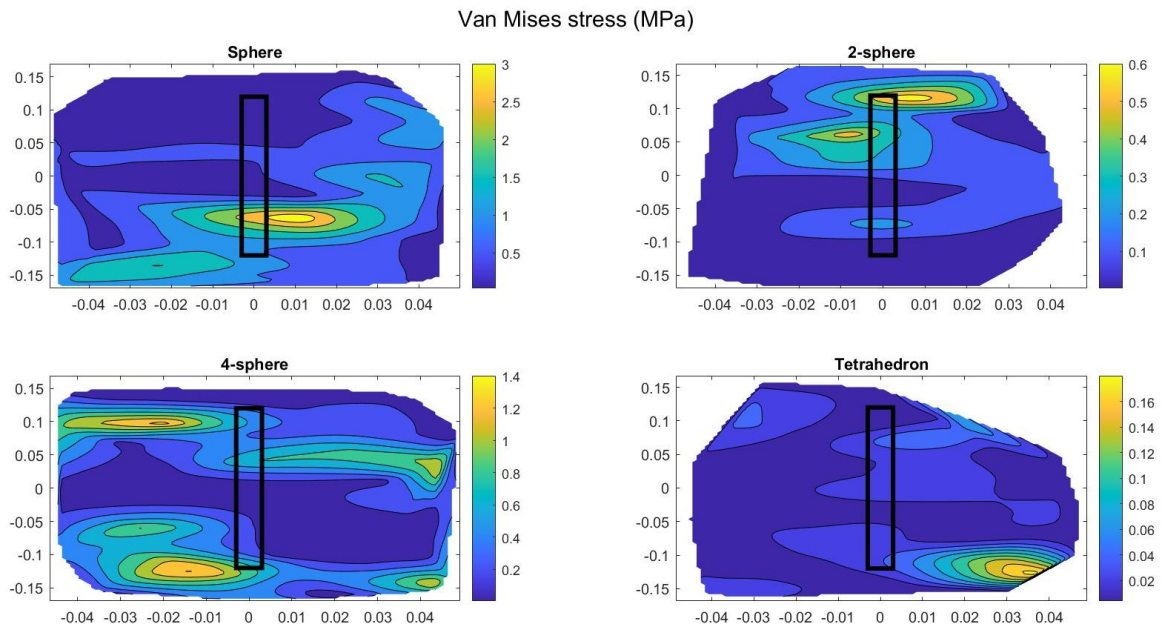
Figure 5.12: DoE case 8: Top view of particles von Mises stress under the plate (black rectangle) at the maximum penetration depth

Particle displacement

Lastly, one can compare the bulk behaviour of the particles in the DEM model by looking at the displacement of the particle during penetration in the experimental test. A gap is formed due to plate penetration as shown in Figure 5.13. The cross-section of the experimental domain was created using a depth camera as explained in Section 4.2. Next, the cross-sections of DEM model domain at the same scale is inserted next to it, by aligning the top line, which is the original almost horizontal material bed. The bottom line with the maximum penetration for the experimental case can be thus compared to the vertical gap extent in DEM for various particle shapes. Spherical particles reveal the most accurately the small heave observed during the experiment, however this upward movement of the particles could also be a consequence of the potential side wall effects.

These cross-sections also show that although the particles are created using an equivalent volume approach, side wall effects are stronger for spherical particles, since effectively their diameter is larger. Moreover, the vertical gap formed by inserting the plate into the material composed of tetrahedrons is clearly smaller than for the experimental profile, which could raise the question whether the tetrahedron revels a realistic bulk behaviour of the particle. However these profiles are subject to the variability of the material, including different packing and orientations in both DEM and experimental models.
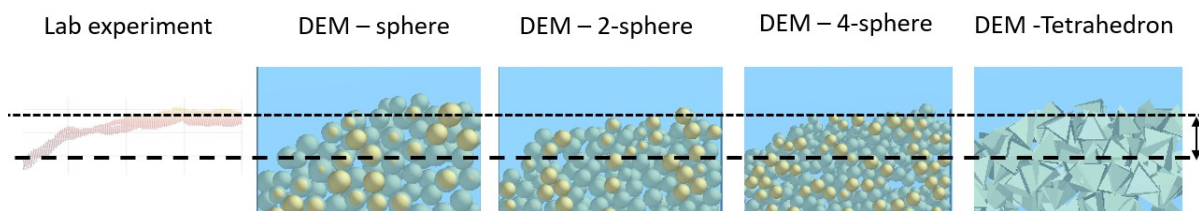
Figure 5.13: Vertical extent of the gap formed due to plate ($w = 6mm$) penetration in a material with $d_{50} = 30mm$

5.3.3. Verification and validation of the model

Having a well-calibrated DEM model is not completed without two additional steps, which are verification and validation. Therefore, this section aims to include the results of some additional simulations and discuss if the produced calibrated input parameters can be verified and validated. Table 5.5 indicates the configurations for the verification and validation cases explored in this section. Additional simulations which use a different set of input parameters than the final optimised calibrated set presented in Section 5.3.1 are included for reference in Appendix E.

Table 5.5: Verification and validation input configurations

	d_{50} (mm)	w (mm)	d_{50}/w (-)
Reference (calibration)	30	6	5
Verification	30	4	7.5
Validation option 1	30	18.8, 15, 12.5, 10, 9.1	1.6, 2, 2.4, 3, 3.3
Validation option 2	9.5, 12, 20	6, 4	1.6, 2, 2.4, 3, 3.3, 5

Verification of model

As outlined in the flowchart in Figure 5.1, what has been done so far is matching the results of the DoE with the experimental data. However, one can use the experimental results for comparison for the bulk density test such that an additional KPI can be checked. In this way the model gets verified by independent test results. The entry of Table 5.6 referring to a $d_{50} = 30mm$ shows that the porosity of the material in the same cylinder used for the AoR is 52.5%, which is reasonably close to the value of $50 \pm 4\%$ found after the experimental test. Therefore the first step in the verification stage is completed and the optimised set of input parameters can be thus verified. The rest of the entries of Table 5.6 are to be used later for validation purposes.

Table 5.6: DEM validation results of the calibrated model: AoR and bulk density tests

d_{50} (mm)	9.5	12	20	30
AoR (deg)	40.1	38.1	37.3	35.1
(Bulk) Porosity (%)	47.9	48.9	50.1	52.5

The other method to verify the calibrated data set is to use another independent penetration test results and compare with the output of the DEM model. For the application of the research, verification is considered keeping the same size of the rock and varying the plate thickness, as indicated in Table 5.5. Therefore, using the calibrated set of input parameters, these can be verified in a model using the largest rock size ($d_{50} = 30mm$) and allowing the penetration of a thinner plate ($w = 4mm$). For a graphical representation of this validation stage, the reference and the validation case and included in Figure 5.14. Although the DEM model is overestimating the penetration resistance, the magnitude of the force and work developed until reaching a depth of 0.14 m is reasonably similar. It can also be seen that the DEM penetration force fluctuates more than the laboratory results which could be due to the amount of particles which come into contact with the plate at each time step (from which the interaction forces between the plate and the particles get calculated).
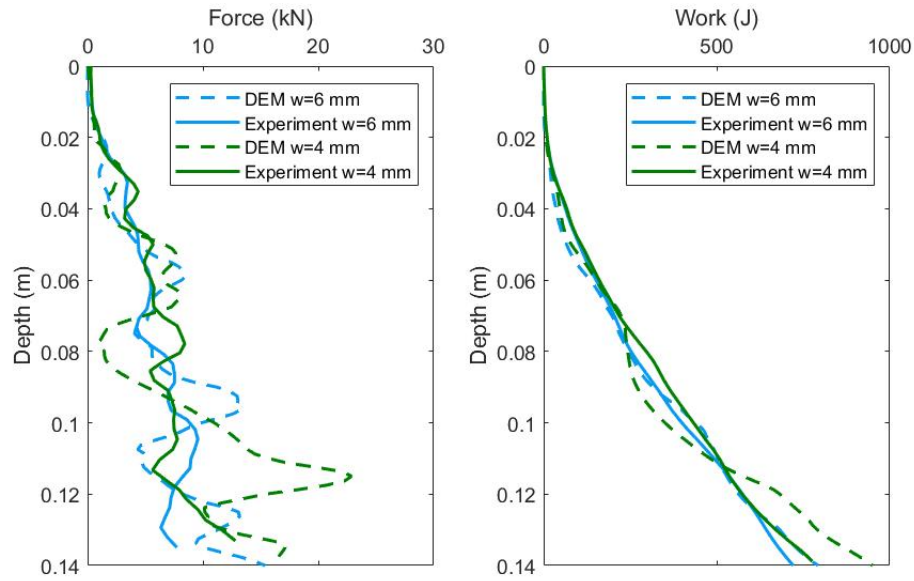
Figure 5.14: Verification of the calibrated input parameters by comparing DEM with experimental results ($d_{50} = 30mm$)

Validation - AoR model

The AoR can be compared with the experimental data for different rock sizes. Figure 5.15 shows that a linear trend line can be plotted through all 4 data points originating from the DEM simulations. Both the experimental data and the DEM results show an increasing trend for the AoR with a decrease in particle size, which is contradictory with the findings of Li et al. (2017). The detailed experimental results for the AoR for all rock sizes are included in Appendix B. Figure 3.4 showed that for particles below 7 mm, a direct proportionality between the particle size and the AoR is recorded. However, in the current research, much larger sized particles are used, which are also particularly angular, thus the measurement of the slope is more difficult and prone to error. This difference in measurement could explain the difference in trends with the previous research.
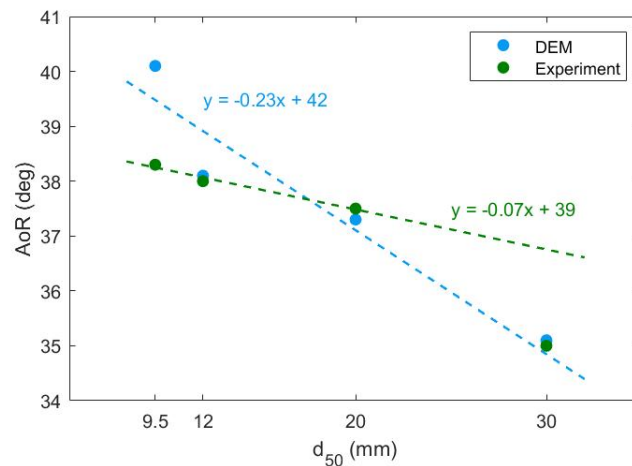
Figure 5.15: Comparison AoR from DEM with the experimental results

Additionally, Figure 5.15 identifies that the experimental data shows a less steep trend line which can be plotted through the AoR results of the smaller rock sizes, in comparison to the trend line of the DEM results. As concluded from Chapter 4, the angle of repose for the larger particle sizes was underestimated due to the imprecise measurement of the angle of the pile, so it is considered more appropriate

to leave this point out of the trend line. Moreover, the calibrated set of input parameters used in this AoR test show very close match with the experimental data for $d_{50} = 12, 20$ and $30\ mm$ and even for the smallest diameter particles, the difference in the results is 2 degrees, which is an acceptable range for this type of test. Therefore, showing good correlation with experimental results of the AoR test, it can be concluded that the model can be validated using this additional test.

Validation - Penetration test

With respect to methods of validation using additional penetration tests performed in the laboratory, different scenarios are going to be investigated, since it involves designing DEM simulations for different ratios of the size of the particles and width of the plate, as previously shown in Table 5.5. There are two options in which one can obtain these ratios, first option being to keep the same particle size and only increase the width of the penetration tool. As a second option, one can vary both the width of the penetrating tool and the particle sizes, reaching the exact same ratios as those used in the experimental case.

Validation - Penetration test option 1

First option of validation is conducted such that additional simulations are performed by keeping the optimised set of input parameters, the size and the spherical shape of the particles, while varying the width of the penetrating tool. The results are inserted in Figure 5.16. The results do not show an increasing trend of the penetration work with higher ratio of the d_{50}/w as shown by the experimental tests. This suggests the fact that DEM cannot capture accurately the difference in penetrating force when the width of the penetrating tool is very small in comparison to the mean size of the rocks. Therefore, this implies that the penetration mechanism is highly dependent on the rock size, and less influenced by the width of the penetrating tool.
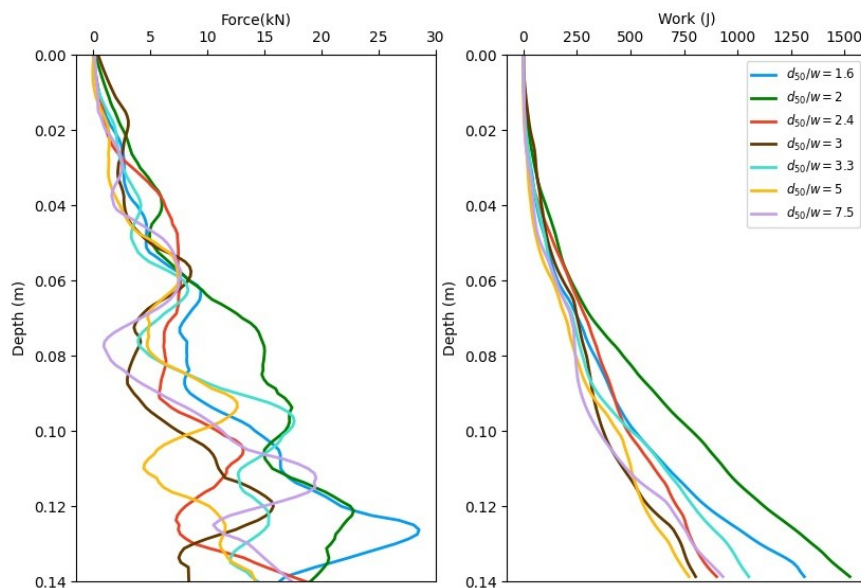
Figure 5.16: Validation (option 1) of the DEM calibrated model with the experimental results for $d_{50} = 30mm$

The results of validation 1 can be explained by looking at the normal force during the penetration. Figure 5.17 shows a graph with the evolution of the average normal forces developed between particles for two extreme cases, a very thick and a very thin plate. It can be seen that the normal forces trend lines are similar in a qualitative way. When showing the evolution of chain forces over depth (at 0.4, 0.9 and 0.14 m), then it can be observed that the thicker plate develops overall higher normal forces and that the produced chain force network is developed deeper, indicating a possible influence of the bottom boundary. This can explain why there are higher penetration forces recorded on the thicker plate than

predicted, since by changing the thickness of the plate, the confinement given by the domain becomes more relevant.
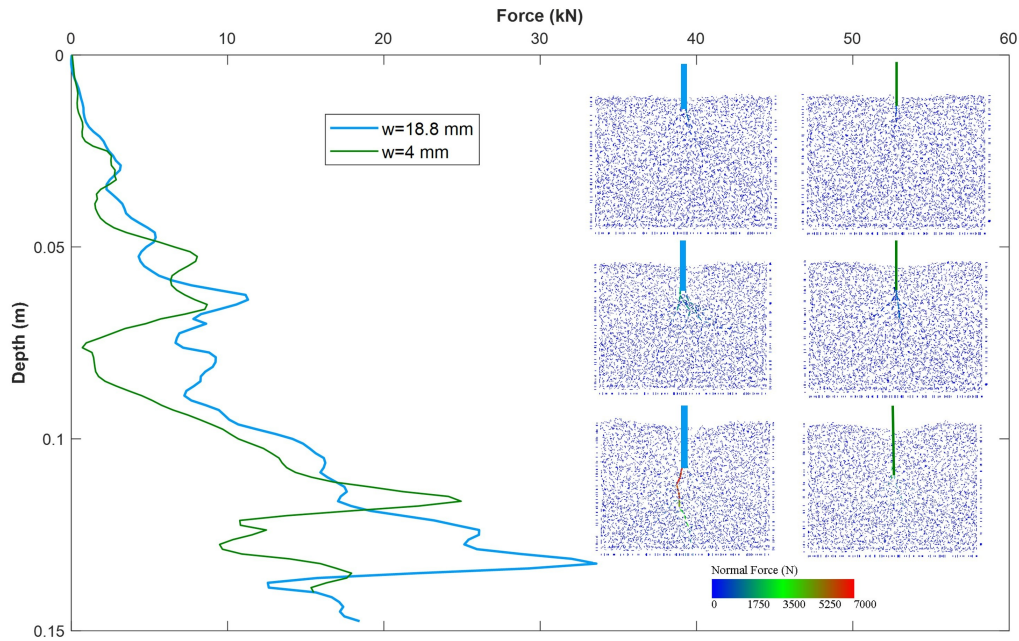
Figure 5.17: Average normal force and chain forces for thicker plate (left) and thinner plate (right) at 0.04, 0.9 and 0.14 m depth

In addition to the chain force network, compressive force between particles can also provide an explanation for the results of validation option 1. The compressive force refers to the sum of contact normal forces between the particles. The results of validation option 1 can be explained by comparing the evolution of magnitude of compressive forces in the area next to the plate. The volume is chosen as shown in Figure 5.18. It can be seen from the graph presented in the same figure, that the compressive force increase with time, however, the more the plate penetrates in the material, the compressive forces decrease for both plate thicknesses.
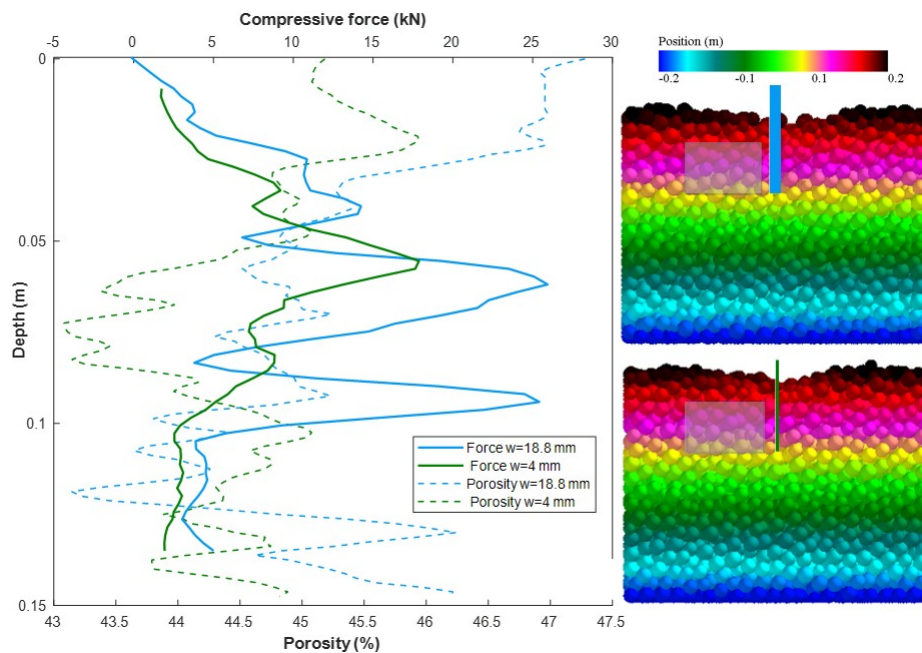
Figure 5.18: Compressive force experienced next to the penetrating plate

Furthermore, the graph in Figure 5.18 reveals a similar mechanism to the friction fatigue phenomena, which was previously introduced in Section 2.1. It can be seen that there is a certain point during the penetration when the stress level behind the tip is reduced. Although the focus so far was laid on the total penetration resistance which is composed of both the shaft friction and tip friction, by analysing the forces between the particles in the vicinity of the penetrating plate, one can observe that the shaft resistance of the plate is reduced with deeper penetration. In addition, the relaxation phase is captured also by looking at the porosity evolution also displayed in the graph in Figure 5.18. The porosity decreases in the specified volume as the soil is more compressed under the tip of the plate, however, with further penetration, the porosity gets larger.

Validation - Penetration test option 2

Second validation option refers to varying the rock size and the width of the plate such that the same ratios d_{50}/w are to be modelled. Table 5.7 indicates the work value for the reference case ($w = 6mm$ and $d_{50} = 30mm$), the verification case ($w = 4mm$ and $d_{50} = 30mm$) and validation option 2 simulations in which the mean size of the rock and the width of the plate are both varied.

Table 5.7: DEM results of penetration work (in J) calculated at 0.14 m depth in spherical particles for multiple combinations of particle size and width of the penetrating tool (validation option 2)

	d_{50}=9.5 mm	d_{50}=12 mm	d_{50}=20 mm	d_{50}=30 mm
w=6 mm	11	13	352	773*
w=4 mm	10	12	348	932**

* Calibrated reference case
** Verification case
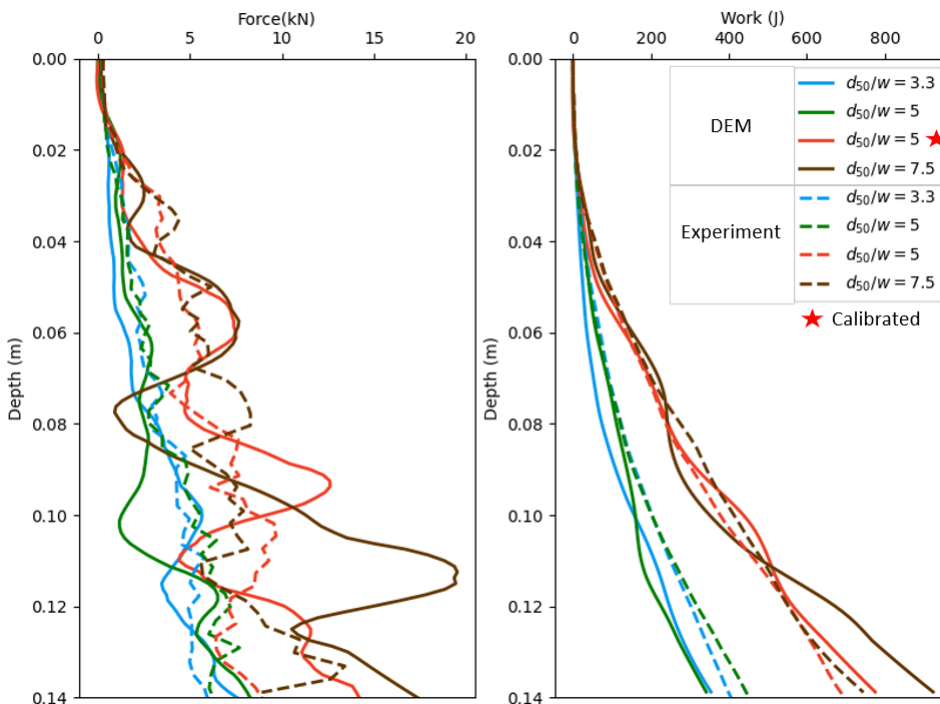
Figure 5.19: Verification and validation option 2 of the DEM with experimental results for d_{50}= 20 & 30 mm

A very important finding refers to the penetration resistance for the case of $d_{50} = 20$ and $30mm$, which can be visualised against the results from the laboratory experiment in Figure 5.19. One can identify an increasing trend of penetration resistance when the particles size is increasing. The work produced by a $w = 4mm$ plate in a material with particles of diameter $d_{50} = 20mm$ is approximately 352 J, which is close to the value 425 J reached during the laboratory experiment, however the exact values cannot

be matched perfectly. Therefore, it can be concluded that the optimised set of input parameters is well validated by this set of laboratory results, which indicates that the created DEM model is able to effectively capture the macro behaviour of the system for the larger rock sizes.

Validation option 2 lack of correlation for smaller particles ($d_{50} = 9.5$ $d_{50} = 12$ mm) as shown in Table 5.7 was investigated by looking into possible input parameters which can have a direct influence on the response of the system. Three option have been identified and are predicted to increase the penetration resistance: increasing the particles shear modulus, restricting particle rotation and narrowing the PSD. However, only the case with restricted rotation allowed for an increase in penetration resistance. In this case, the $\mu_{r-p,p}$ is set to 0.01 (-) and the angular velocity of particles is capped. From Figure 5.20, it can be seen that using the optimised set on input parameters, the validation 2 trend line is underestimating the experimental resistance. However, by restricting the rotation, the force become higher and it can improve the correlation with the experimental results.
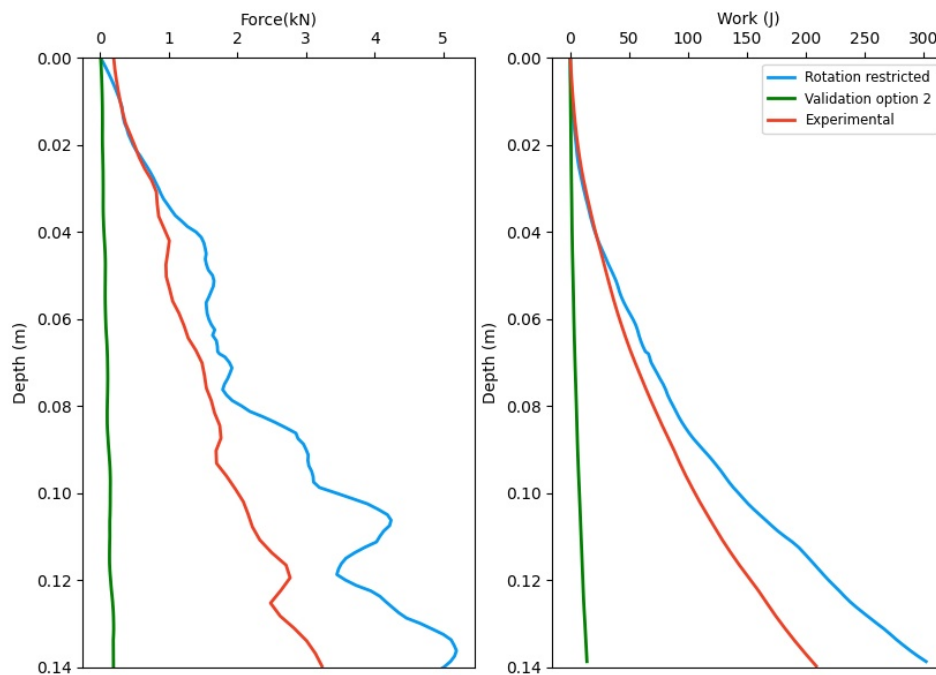
Figure 5.20: Improvement of validation option 2 for d_{50}= 12 mm and $w = $ 6mm

5.4. Conclusion

The calibration strategy identified in Section 3.1 was successfully implemented in this chapter and by performing a DoE, it was shown that it is possible to find an optimised set of variables which give a similar response to that from the experiments. Among the novelties of this research, polyhedrons were also used for shape of particles involved in the penetration test. The results of the penetration resistance provided by the DOE for calibration purposes in a material made of non-spherical particles (multi-spheres and tetrahedrons) do not show a strong correlation with the experimental forces. Therefore, the defined calibration strategy can only be applied to the spherical particles. Although spheres lack the complexity of real particles shapes, they can replicate very accurately the bulk behaviour of the real material used in the laboratory, with the added benefit of a very low computation time. Thus, it is considered that spheres are sufficient to create a DEM model in which penetration resistance needs to be recorded.

The results from the DEM simulations of the AoR test are in agreement with the outcome of the experimental test. The same conclusion can be drawn which reinstates that the choice of experimental set-up for the angle of repose is not appropriate when using a material composed of very large diameter particles. Moreover, verification of the DEM model was accomplished using the bulk density experimental results, but also validation using the results for the AoR for smaller diameter rocks. Both DEM simulation and experimental tests identify a decreasing trend of the AoR with higher size of rocks, which can be attributed to an inaccurate measurement of the slope of the pile, but also on the reduced amount of material using in the test.

The results of the additional experimental penetration tests (different rock size and width of the plate) were used for both verification and validation. Figure 5.21 shows the experimental data and the DEM results plotted in terms of the work needed for penetration until the maximum depth. The graph identifies a limitation of the DEM model, which is not able to capture the bulk behavior when the rock size is kept constant and only the width of the plate was varied (validation option 1). The reason behind this lays in the normal forces between particles in the case of thicker plate which develop a force chain network where the boundaries effects become more prominent. However, partial validation was successfully achieved when changing both the rock size and the width of the plate (validation option 2). An underestimation of the penetration resistance for lower ratios by a scale factor is attributed to an incapability of the DEM model to capture the bulk behaviour using the optimised set of input parameters. It is shown that by restriction rotation between particles, better correlation with the experimental penetration resistance can be achieved also for lower ratio d_{50}/w.
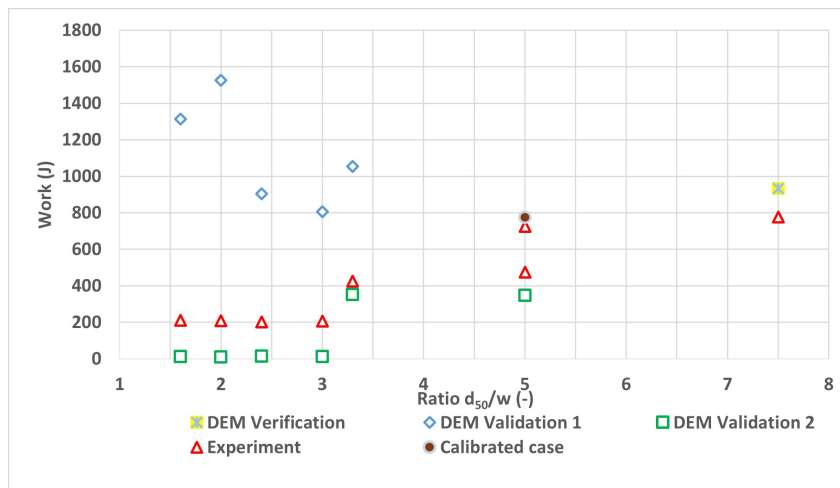
Figure 5.21: Comparison results of the DEM model versus the experimental penetration test)

Figure 5.21 also identifies a sharp transition in the required penetration force when the ratio d_{50}/w exceeds the value of 3 for both the experimental and DEM results. A non-linear dependence of the penetration resistance on the ratio d_{50}/w is captured by the DEM results validation option 2, thus this is considered as the final DEM simulations output which replicate the best the experimental penetration test. Therefore, one can identify a lower regime when the penetration force is low and constant, and an upper regime with an increasing trend for penetration resistance for larger rocks. The lower regime of the DEM results underestimates the experimental penetration resistance and for this reason it can be concluded that the optimised set of input parameters is not applicable to this lower regime, thus a separate calibration procedure is required.

<div style="text-align: right; font-size: 3em;">6</div>

Conclusion and Recommendations

This chapter describes in Section 6.1 the achievements of this research in the context of industry demands but also with respect to current scientific interests. Then, the most important conclusions of the research are highlighted in Section 6.2 by addressing the research and sub-research questions using the results form this research. Lastly, the chapter ends with recommendation for future work in Section 6.3.

6.1. Research gain

In terms of the benefits for the industry, this research brings a valuable insight into the mechanism of a penetration test. The offshore industrial problem refers to driving the monopile through a pre-installed scour protection layer. The problem consists of assessing the resistance to penetration of a relatively thin object, such as the wall of the monopile, into a material composed of rocks of large dimensions. This research uses a down-scaled model to simulate the scenario by making use of both an experimental set-up and a numerical model. Although there are numerous pre-existing papers on the pile-soil interaction, there is little knowledge available on the dependency of the penetration resistance on a material which has the characteristics of the rock armour. Hence, this research identifies how the penetration resistance varies when investigating several ranges for the size of the armour rocks and thickness of the penetrating tool.

From an academic perspective, this research aims to fill in the gap of multiple aspects which are less commonly investigated during the design of a DEM penetration test model:

- constructing a model in which the size of the particles is larger than the width of the penetrating tool

- calibrating a model by replicating as close as possible an experimental test

- using a multi-objective optimisation strategy in which several key performance indicators provided by the laboratory tests are compared with the response of the model

- carrying out a design of experiments strategy with a full factorial design to optimise the input parameters

- investigating the effect of shape of particles by constructing equivalent multi-spheres and tetra-hedrons for the material particles

- performing verification and validation of the optimised input parameters based on additional laboratory test results

<div style="text-align: center;">92</div>

6.2. Conclusions

The main findings with regards to the research and sub-research questions are addressed below:

Research question: *What are the limiting factors behind the self-weight penetration and subsequent driving of a monopile through the scour protection layer with regards to finding a relation between the mean size of the scour protection armour rock and the thickness of the wall of the monopile ($d_{50/w}$)?*.

- The results from both the experimental test and the DEM numerical model identify a sharp transition in the penetration resistance for ratios d_{50}/w higher than 3, as shown in Figure 6.1. In other words, when a plate penetrates the coarse material, the force profile over depth is rather constant for ratios d_{50}/w below 3, however, after this threshold, one can observe a sudden increase in the penetration resistance output values. This non-linear dependence of work on the ratio d_{50}/w suggests a division into two different regimes, a lower and higher regime of penetration force. Although the DEM results for the lower regime are underestimating the penetration resistance observed during the experimental testing by a scale factor, it is concluded that a different set of input parameters is required for calibration of the parameters in this low regime. Nevertheless, the DEM lower regime identifies also a reduced and rather constant penetration work, which is a similar behaviour with that from the experimental tests.
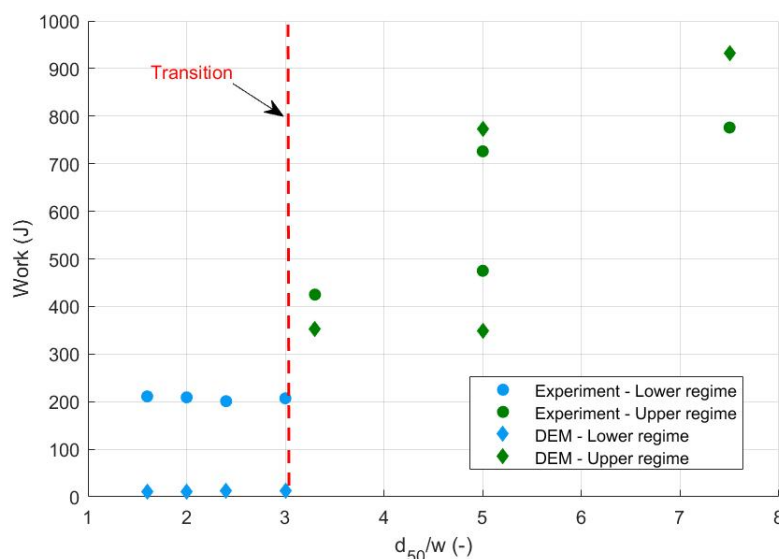
Figure 6.1: Experimental and DEM results of work at maximum penetration depth at different ratios d_{50}/w

- Therefore, the ratio of d_{50}/w of 3 (-) is the limiting factor identified by this research, from which the driving of the pile can get hindered. The same ratio is suggested to be applied to a full scale model of a pile penetrating the rock armour layer, with some additional remarks. The scour protection layer has no lateral confinement, thus the possible lateral displacement of the rocks would allow for a reduced penetration force required to drive the pile. The pile material is similar to that used in the model, however the stresses experienced at the tip of the pile are predicted to be much higher than in the model. Thus, the presented limited ratio is a conservative estimate when applied to the full-scale scenario. What is also worth mentioning is that using the same results and applying them to an up-scaled scenario is a challenge on its own. It is hard to predict the influence of the scaling laws and the lack of complexity usually experienced during the offshore installation event.

Sub-research question: *How does the penetration resistance change with depth with respect its dependence on the characteristics the rock armour?*

- From the tests performed, it can be seen that when using a larger sized rocks, the force required to push the plate into the coarse material significantly increases. Quantitatively speaking, when the rock diameter is doubled, the penetration resistance is also approximately twofold. However, for smaller rock particles, the penetration resistance is low and rather constant, and the conclusion which is drawn here is that the penetration resistance is highly influenced by the size of the rocks.

- Using the DEM software, it was shown that other characteristics such as particle density, elastic properties, but also packing highly influences the penetration resistance. In particular, higher density and larger shear modulus leads to a more difficult plate penetration. A reduction of the particle shear modulus leads to a lower computational time, however it might lead to an unrealistic bulk elastic deformation of the particle in the material. Moreover, the factory used for particle generation has an impact on their packing, which then has a direct influence on the penetration resistance recorded on the plate.

- Another aspect investigated in this thesis refers to the shape of the particles used in the numerical model for the rock material. The conclusions of the study indicates that the calibrations strategy employed for the spherical particles is inapplicable for more complex shapes (for instance multi-sphere and tetrahedrons). However, using spherical particles as a simplification for the complex angular shape of the rocks is efficient in terms of computational time and allowed for an accurate calibration, verification and validation of the DEM model.

- The strength of the rock is also identified as a key influence factor for the penetration mechanism, since especially at larger rock sizes, crushing under the tip of the plate is observed during the experimental testing, which decreases the penetration force required to insert the plate. It was also shown that using a simple correlation with a point load test, the force encountered during the tests at the tip of the pile exceeded the strength of the rocks, thus breakage is predicted to occur also in an up-scaled scenario. However, emphasis has to be laid on the different lateral and vertical constraints in the real offshore application, when the rocks may be instead laterally displaced due to their lack of confinement, or vertically by mixing with the material in the subsoil.

Sub-research question: *What is the effect of changing the wall thickness of the monopile on the driving resistance of the monopile through the armour layer?*

- When changing the penetrating tool thickness, an important mechanism is noticed during the laboratory work which shows buckling of the plate during the most extreme case (largest rocks and smallest width of the plate). Keeping in mind that the properties of the plate were not down-scaled during the test, it is conservative to suggest that buckling of the tip of the pile in a real offshore up-scaled application may be experienced in this case.

- When using the same rock size and different plate thicknesses, a similar experimental trend for the penetration resistance is recorded, thus the results are inconclusive due to the large variability of the material. Thus, with the tested ranges of d_{50} and w, the penetration resistance is much more dependent on the rock size than on the thickness of the plate. A similar conclusion is reached when performing DEM simulations for validation of the experimental results. For instance, designing the plate three times thicker than used in the experiment resulted in a similar trend line of the penetration resistance over depth.

6.3. Recommendations

Several recommendations arise from the findings and the conclusions of this thesis. These can be used as a starting point from future research on the topic, but also as possible modifications to the approach used in this research.

1. When designing experiments which make use of coarse large rock material, the use of specialised set-ups and equipment to determine parameters such as angle of repose, bulk density, particle density, etc., is highly recommended (for instance a test designed for soil-like material is not applicable for rock fragments). In this way, the wall effects can be minimised and parameters of interest can be more accurately measured.

2. The preliminary analysis performed in this thesis suggests that the design of the experimental test (geometries, number of particles, kinematics and domain) should be made such that the large computational time of the equivalent DEM model should be kept in mind. In addition, another recommendation refers to making use of latest hardware to boost computational speed (for instance a large number of CPU cores or a high performance GPU), instead of performing simplifications to the DEM model, which introduces errors and inaccuracies.

3. Another recommendation arises from an observation made during the experimental tests. Since crushing of the particles during penetration was observed, then future work should investigate the effect of bonding and breakage of particles on the recorded penetration force. It is believed that for a coarse angular material as the one used in the laboratory test, crushing and breakage of the rocks may highly impact the penetration force recorded. Thus, it is considered necessary for future work to improve the replication of the observed phenomena during the laboratory work.

4. A more comprehensive investigation into how to perform the calibration of non-spherical particles is required. Aspects such as the rolling friction model, shape equivalence construction and input parameters should be further looked into when designing simulations composed of multi-sphere and tetrahedron particles. In other words, a specialised calibration procedure should be identified for non-spherical particles such that better correlation with the bulk behaviour from laboratory tests can be achieved. An additional recommendation is to include a more random and complex polyhedral shape for the particles, which in this research was not possible using EDEM 2021.

5. Further DEM modelling is required to establish an additional optimised set of calibration parameters for the lower regime of penetration resistance for ratios d_{50}/w smaller than 3 (-). An additional DoE needs to be performed such that an improved correlation between the bulk behaviour of the material in DEM with that from the experimental testing can be found.

6. Additional tests are required in order to further explore the dependence of the penetration force on the size of the particles and the thickness of the penetrating tool (more ratios d_{50}/w). In particular, for the experimental work, more extreme case studies (large rock size and reduced width of the plate) should be investigated to confirm the buckling phenomena. In addition, a saturated penetration should be performed in the laboratory by also coupling DEM and CFD such that one can check the influence of a submerged test on the bulk behaviour of the material. A reduced or an increased domain can also be explored to further investigate boundary effects. Layering with material composed of different rock sizes is suggested to be explored in order to replicate a scenario with an underlying filter layer or a soil-bed. Additionally, adding a hammer-like dynamic kinematics for the insertion for the plate should be investigated and modelled in DEM. Lastly, a large scale, more complex prototype is required to fully investigate the effect of scaling laws used in this research, but also the influence of simplifications used in the tests performed in this research.

References

Abou-Chakra, H., Baxter, J., and Tüzün, U. (2004). Three-dimensional particle shape descriptors for computer simulation of non-spherical particulate assemblies. *Advanced Powder Technology*, 15(1):63–77.

Ahmed, S., Harkness, J., Le Pen, L., Powrie, W., and Zervos, A. (2016). Numerical modelling of railway ballast at the particle scale. *International Journal for Numerical and Analytical Methods in Geomechanics*, 40(5):713–737.

Ai, J., Chen, J.-F., Rotter, J. M., and Ooi, J. Y. (2011). Assessment of rolling resistance models in discrete element simulations. *Powder Technology*, 206(3):269–282.

Albert, R., Pfeifer, M. A., Barabási, A. L., and Schiffer, P. (1999). Slow drag in a granular medium. *Physical Review Letters*, 82(1):205–208.

Alder, B. J. and Wainwright, T. E. (1957). Phase transition for a hard sphere system. *The Journal of Chemical Physics*, 27(5):1208–1209.

Almuni, M., Dauwe, T., Moorkens, I., Saarikivi, R. J., and Tomescu, M. (2020). Renewable energy in Europe — 2020 recent growth and knock-on effects. Technical report, European Environmental Agency.

Antony, J. (2014). *Design of Experiments for Engineers and Scientists Second Edition*. Elsevier.

Arroyo, M., Butlanska, J., Gens, A., Calvetti, F., and Jamiolkowski, M. (2011). Cone penetration tests in a virtual calibration chamber. *Geotechnique*, 61(6):525–531.

ASM (2021). Material Data Sheet.

Beakawi Al-Hashemi, H. M. and Baghabra Al-Amoudi, O. S. (2018). A review on the angle of repose of granular materials. *Powder Technology*, 330:397–417.

Bolton, M. D., Gui, M. W., Garnier, J., Corte, J. F., Bagge, G., Laue, J., and Renzi, R. (1999). Centrifuge cone penetration tests in sand. *Geotechnique*, 49(4):543–552.

Boskalis (2016a). Offshore Wind farm Monopile Installation Veja Mate.

Boskalis (2016b). Veja Mate Offshore Wind Farm Project Sheet.

Bosscher, P. J., ASCE, A. M., and Ortiz, C. (1988). Frictional Properties between sand and various construction materials. *Geotechnical Engineering*, 113(9):1035–1039.

Breul, P., Benz, M., Gourvès, R., and Saussine, G. (2009). Penetration test modelling in a coarse granular medium. *AIP Conference Proceedings*, 1145(173).

Brucy, F., Meunier, J., and Nauroy, J. F. (1991). Behavior of pile plug in sandy soils during and after driving. *Proceedings of the Annual Offshore Technology Conference*, (1):145–154.

Bullard, J. W. and Garboczi, E. J. (2013). Defining shape measures for 3D star-shaped particles: Sphericity, roundness, and dimensions. *Powder Technology*, 249:241–252.

Butlanska, J., Arroyo, M., and Gens, A. (2009). Homogeneity and symmetry in DEM models of cone penetration. *AIP Conference Proceedings*, 1145(January 2014):425–428.

Butlanska, J., Arroyo, M., and Gens, A. (2010a). Size effects on a virtual calibration chamber. *7th European Conference on Numerical Methods in Geotechnical Engineering*, (May 2014):213–218.

Butlanska, J., Arroyo, M., and Gens, A. (2010b). Virtual Calibration Chamber CPT on Ticino sand. *2nd International Symposium on Cone Penetration Testing*, (September 2014):217–224.

Butlanska, J., Arroyo, M., Gens, A., and O'Sullivan, C. (2014). Multi-scale analysis of cone penetration test (CPT) in a virtual calibration chamber. *Canadian Geotechnical Journal*, 51(1):51–66.

Byrne, B. W. and Houlsby, G. T. (2003). Foundations for offshore wind turbines. *Philosophical Transactions of the Royal Society A: Mathematical, Physical and Engineering Sciences*, 361(1813):2909–2930.

CARRIGY, M. A. (1970). Experiments on the Angles of Repose of Granular Materials. *Sedimentology*, 14(3-4):147–158.

Chung, Y. C. and Ooi, J. Y. (2006). Confined Compression and Rod Penetration of a Dense Granular Medium: Discrete Element Modelling and Validation. In *Springer Proceedings in Physics*, pages 223–239. Springer Berlin Heidelberg.

Ciantia, M. O., O'Sullivan, C., and Jardine, R. J. (2019). Pile penetration in crushable soils : Insights from micromechanical modelling. *Proceedings of the XVII ECSMGE-2019*, (September):298–317.

CIRIA, CUR, and CETMEF (2007). *The Rock Manual. The use of rock in hydraulic engineering*. London, 2nd edition.

Cleary, P. W. (2010). DEM prediction of industrial and geophysical particle flows. *Particuology*, 8(2):106–118.

Coetzee, C. J. (2016). Calibration of the discrete element method and the effect of particle shape. *Powder Technology*, 297:50–70.

Coetzee, C. J. (2019). Particle upscaling: Calibration and validation of the discrete element method. *Powder Technology*, 344:487–503.

Cundall, P. A. and Strack, O. D. (1979). A discrete numerical model for granular assemblies. *Geotechnique*, 29(1):47–65.

Damiani, R., Dykes, K., and Scott, G. (2016). A comparison study of offshore wind support structures with monopiles and jackets for U.S. waters. *Journal of Physics: Conference Series*, 753(9).

Das, N. (2007). *Modeling Three-Dimensional Shape of Sand Grain Using Discrete Element Method*. PhD thesis, University of South Florida.

Deiros, I., Voivret, C., Combe, G., and Emeriault, F. (2016). Quantifying Degradation of Railway Ballast Using Numerical Simulations of Micro-deval Test and In-situ Conditions. *Procedia Engineering*, 143(Ictg):1016–1023.

DeJong, J. T., Jaeger, R. A., Boulanger, R. W., Randolph, M. F., and Wahl, D. A. (2013). Variable penetration rate cone testing for characterization of intermediate soils. *Geotechnical and Geophysical Site Characterization 4 - Proceedings of the 4th International Conference on Site Characterization 4, ISC-4*, 1(April 2016):25–42.

Deltares (2017). Scour and Scour Mitigation. Technical report.

DNV (2010). Design of Offshore Wind Turbine Structures. Standard, Det Norske Veritas.

Doherty, P. and Gavin, K. (2012). Laterally loaded monopole design for offshore wind farms. *Proceedings of Institution of Civil Engineers: Energy*, 165(1):7–17.

Duan, N., Cheng, Y. P., and Liu, J. W. (2018). DEM analysis of pile installation effect: comparing a bored and a driven pile. *Granular Matter*, 20(3):1–16.

EDEM (2018). *User Guide*. DEM Solutions, Edinburgh.

EDEM (2021a). 10 Common Questions about EDEM GPU Answered - Altair Community.

EDEM (2021b). *Altair Engineering*.

Eliáš, J. (2014). Simulation of railway ballast using crushable polyhedral particles. *Powder Technology*, 264:458–465.

Endait, M. and Juneja, A. (2014). New correlations between uniaxial compressive strength and point load strength of basalt. *International Journal of Geotechnical Engineering*, 9:1939787914Y.000.

Esposito, R. G., Velloso, R. Q., Jr, E. d. A. V., and Danziger, B. R. (2018). Multi-scale sensitivity analysis of pile installation using DEM. *Computational Particle Mechanics*, 5(3):375–386.

Falagush, O., McDowell, G. R., and Yu, H.-S. (2015). Discrete Element Modeling of Cone Penetration Tests Incorporating Particle Shape and Crushing. *International Journal of Geomechanics*, 15(6):04015003.

Favier, J., Abbaspour-Fard, M., Kremmer, M., and Raji, A. (1999). Shape representation of axisymmetrical, non-spherical particles in discrete element simulation using multi-element model particles. *Engineering Computations*, 16(4):467–480.

Feng, Y., Blumenfeld, R., and Liu, C. (2019). Support of modified Archimedes' law theory in granular media. *Soft Matter*, 15(14):3008–3017.

Feng, Y. T., Han, K., Owen, D. R., and Loughran, J. (2009). On upscaling of discrete element models: Similarity principles. *Engineering Computations (Swansea, Wales)*, 26(6):599–609.

Feng, Y. T. and Owen, D. R. (2014). Discrete element modelling of large scale particle systems—I: exact scaling laws. *Computational Particle Mechanics*, 1(2):159–168.

Fine (2021). Table of Ultimate Friction Factors for Dissimilar Materials (according to NAVFAC standards).

Garcia, G (2012). Design and Calculus of the Foundation Structure of an Offshore Monopile Wind Turbine. Technical report, Universitat Politecnica de Catalunya.

Gavin, K. (2020). Lecture notes - axial resistance of piles in sand. Technical University of Delft.

Gezgin, A. T., Soltanbeigi, B., and Cinicioglu, O. (2020). Discrete-element modelling of pile penetration to reveal influence of soil characteristics. *Proceedings of the Institution of Civil Engineers - Geotechnical Engineering*, pages 1–42.

GL (2012). Guideline for the Certification of Offshore Wind Turbines. Technical report, Germanischer Lloyd Industrial Services GmbH, Hamburg.

Guo, Y., Zhao, C., Markine, V., Jing, G., and Zhai, W. (2020). Calibration for discrete element modelling of railway ballast: A review. *Transportation Geotechnics*, 23(January):100341.

Helmons, R. L. and Miedema, S. A. (2007). Cutting through hard rock-like materials, a review of the process. *18th World Dredging Congress 2007, WODCON 2007*, (January):966–979.

Hoffmans, G. and Verheij, H. (1997). *Scour manual*. A.A.Balkema, Rotterdam.

Höhner, D., Wirtz, S., and Scherer, V. (2014). A study on the influence of particle shape and shape approximation on particle mechanics in a rotating drum using the discrete element method. *Powder Technology*, 253:256–265.

Huang, A. B., Ma, M. Y., and Lee, J. S. (1992). A micromechanical study of penetration tests in granular material. *Studies in Applied Mechanics*, 31(C):173–181.

Huang, H. and Tutumluer, E. (2011). Discrete Element Modeling for fouled railroad ballast. *Construction and Building Materials*, 25(8):3306–3312.

Igoe, D., Doherty, P., and Gavin, K. (2010). The development and testing of an instrumented open-ended model pile. *Geotechnical Testing Journal*, 33(1).

Igwemezie, V., Mehmanparast, A., and Kolios, A. (2019). Current trend in offshore wind energy sector and material requirements for fatigue resistance improvement in large wind turbine support structures – A review. *Renewable and Sustainable Energy Reviews*, 101(October 2016):181–196.

ISRM (1985). Suggested method for determinifn point load strength. *International Journal fof Rock Menchanics and Mining Sciences and Geomechanical Abstract*, 22(2):51–60.

Itasca (2019). Data Files for "Rolling Resistance Linear Contact Model: Repose Angle" Problem — PFC 6.0 documentation.

Iwashita, K. and Oda, M. (1998). Rolling resistance at contacts in simulation of shear band development by dem. *Journal of Engineering Mechanics*, 124(3):285–292.

Janda, A. and Ooi, J. Y. (2016). DEM modeling of cone penetration and unconfined compression in cohesive solids. *Powder Technology*, 293:60–68.

Jardine, R. J., Lehane, B. M., and Everton, S. J. (1993). Friction Coefficients for piles in sands and silts. *Offshore Site Investigation and Foundation Behaviour*, 28:661–667.

Jersey, U. (1997). Ask GeoMan.

Ji, S., Sun, S., and Yan, Y. (2017). Discrete element modeling of dynamic behaviors of railway ballast under cyclic loading with dilated polyhedra. *International Journal for Numerical and Analytical Methods in Geomechanics*, 41(2):180–197.

Jiang, M., Dai, Y., Cui, L., Shen, Z., and Wang, X. (2014). Investigating mechanism of inclined CPT in granular ground using DEM. *Granular Matter*, 16(5):785–796.

Jiang, M. J., Yu, H. S., and Harris, D. (2006). Discrete element modelling of deep penetration in granular soils. *International Journal for Numerical and Analytical Methods in Geomechanics*, 30(4):335–361.

Jin, W. and Zhou, J. (2010). A Coupled Micro-Macro Method for Pile Penetration Analysis. *GeoShanghai International Conference*, (200):234–239.

Jing, L. and Stephansson, O. (2007). *Fundamentals of Discrete Element Methods for Rock Engineering*, volume 85. Elsevier Science.

Katterfeld, A., Coetzee, C., Donohue, T., Fottner, J., Grima, A., Ramirez Gomez, A., Ilic, D., Kačianauskas, R., Necas, J., Schott, D., Williams, K., and Zegzulka, J. (2019). Calibration of DEM Parameters for Cohesionless Bulk Materials under Rapid Flow Conditions and Low Consolidation.

Kou, Y.-S., Achmus, M., and Kao, C.-S. (2008). Practical design considerations of monopiles with respect to scour. Technical report.

Kruggel-Emden, H., Rickelt, S., Wirtz, S., and Scherer, V. (2008). A study on the validity of the multi-sphere Discrete Element Method. *Powder Technology*, 188(2):153–165.

Kumara, J. J., Kikuchi, Y., Kurashina, T., and Yajima, T. (2016). Effects of inner sleeves on the inner frictional resistance of open-ended piles driven into sand. *Frontiers of Structural and Civil Engineering*, 10(4):499–505.

Laryea, S., Safari Baghsorkhi, M., Ferellec, J. F., McDowell, G. R., and Chen, C. (2014). Comparison of performance of concrete and steel sleepers using experimental and discrete element methods. *Transportation Geotechnics*, 1(4):225–240.

Leblanc, C. (2009). *Design of Offshore Wind Turbine Support Structures: Selected topics in the field of geotechnical engineering*. PhD thesis, Aalborg University.

Lee, J. and Salgado, R. (1999). Determination of pile base resistance in sands. *Journal of Geotechnical and Geoenvironemntal engineering*, 125(8):673–683.

Lee, S. (2014). *Developments in large scale discrete element simulations with polyhedral particles*. PhD thesis, University of Illinois.

Lehane, B. M., Jardine, R. J., Bond, A. J., and Frank, R. (1994). Mechanisms of shaft friction in sand from instrumented pile tests. *Journal of Geotechnical Engineering*, 120(8):1450–1452.

Li, L., Wu, W., Hesham El Naggar, M., Mei, G., and Liang, R. (2019). DEM analysis of the sand plug behavior during the installation process of open-ended pile. *Computers and Geotechnics*, 109(September 2018):23–33.

Li, T., Peng, Y., Zhu, Z., Yu, Z., and Yin, Z. (2017). Effect of the Lifting Velocity and Container Shape on Angle of Repose of Iron Ore Particles. *Advances in Materials Science and Engineering*, 2017.

Lin, J. and Wu, W. (2012). Numerical study of miniature penetrometer in granular material by discrete element method. *Philosophical Magazine*, 92(28-30):3474–3482.

Liu, S. and Wang, J. (2016). Depth-independent cone penetration mechanism by a discrete element method (DEM)-based stress normalization approach. *Canadian Geotechnical Journal*, 53(5):871–883.

Lobo-Guerrero, S. and Vallejo, L. E. (2005). DEM analysis of crushing around driven piles in granular materials. *Geotechnique*, 55(8):617–623.

Lobo-Guerrero, S., Vallejo, L. E., and Vesga, L. F. (2006). Visualization of Crushing Evolution in Granular Materials under Compression Using DEM. *International Journal of Geomechanics*, 6(3):195–200.

Lommen, S., Schott, D., and Lodewijks, G. (2014). DEM speedup: Stiffness effects on behavior of bulk material. *Particuology*, 12(1):107–112.

Macaro, G., Utili, S., and Martin, C. M. (2021). DEM simulations of transverse pipe–soil interaction on sand. *Géotechnique*, (3):189–204.

Matutano, C., Negro, V., López-Gutiérrez, J. S., and Esteban, M. D. (2013). Scour prediction and scour protections in offshore wind farms. *Renewable Energy*, 57:358–365.

McDowell, G. R., Falagush, O., and Yu, H. S. (2012). A particle refinement method for simulating DEM of cone penetration testing in granular materials. *Geotechnique Letters*, 2(7-9):141–147.

McDowell, G. R. and Li, H. (2016). Discrete element modelling of scaled railway ballast under triaxial conditions. *Granular Matter*, 18(3).

Melville, B. and Sutherland, A. (1998). Design method for local scour at bridge piers. *Journal of Hydraulic Engineering*, 144(10):1210–26.

Miyai, S., Kobayakawa, M., Tsuji, T., and Tanaka, T. (2019). Influence of particle size on vertical plate penetration into dense cohesionless granular materials (large-scale DEM simulation using real particle size). *Granular Matter*, 21(4):1–21.

Mohajeri, M. J. (2021). *Grabs and Cohesive Bulk Solids. Virtual prototyping using a validated co-simulation*. PhD thesis, TU Delft.

Moore, P. and Booth, G. (2015). *Mechanical testing of welds*.

Mostafa, Y. E. (2012). Effect of Local and Global Scour on Lateral Response of Single Piles in Different Soil Conditions. *Engineering*, 04(06):297–306.

Muhammad, U. H. (2017). Phys track Experimenter's Reference Manual.

Nassauer, B. and Kuna, M. (2013). Contact forces of polyhedral particles in discrete element method. *Granular Matter*, 15(3):349–355.

Nermoen, A. (2010). *Some effects of gas-induced fluidization in dry granular media*. PhD thesis.

O'Sullivan, C. (2011a). Particle-Based Discrete Element Modeling: Geomechanics Perspective. *International Journal of Geomechanics*, 11(6):449–464.

O'Sullivan, C. (2011b). *Particulate Discrete Element Modelling: Geomechanics Perspective*, volume 4. Spon Press.

Peng, D. and Hanley, K. J. (2019). Contact detection between convex polyhedra and superquadrics in discrete element codes. *Powder Technology*, 356:11–20.

Peng, Z., Xu, X., Lu, K., and Hou, M. (2009). Depth dependence of vertical plunging force in granular medium. *Physical Review E - Statistical, Nonlinear, and Soft Matter Physics*, 80(2).

Pisanò, F. (2020). Lecture notes - offshore geotechnical engineering. Technical University of Delft.

Qian, Y., Lee, S., Tutumluer, E., Hashash, Y., Mishra, D., and Ghaboussi, J. (2013). Simulating ballast shear strength from large-scale triaxial tests. *Transportation Research Record*, (2374):126–135.

Randolph, M. and Gourvernec, S. (2011). *Offshore Geotechnical Engineering*. Taylor & Francis.

Roessler, T. and Katterfeld, A. (2016). Scalability of angle of repose tests for the calibration of DEM parameters. *ICBMH 2016 - 12th International Conference on Bulk Materials Storage, Handling and Transportation, Proceedings*, (November):201–211.

Roessler, T. and Katterfeld, A. (2018). Scaling of the angle of repose test and its influence on the calibration of DEM parameters using upscaled particles. *Powder Technology*, 330:58–66.

Schneider, J. A., Xu, X., and Lehane, B. M. (2008). Database Assessment of CPT-Based Design Methods for Axial Capacity of Driven Piles in Siliceous Sands. *Journal of Geotechnical and Geoenvironmental Engineering*, 134(9):1227–1244.

Shi, D., Yang, Y., Deng, Y., and Xue, J. (2019). DEM modelling of screw pile penetration in loose granular assemblies considering the effect of drilling velocity ratio. *Granular Matter*, 21(3):1–16.

Shoda, D., Kawabata, T., Uchida, K., Atsunori, N., and Motoyama, H. (2009). Distinct Element Analysis for Group Piles Subjected to Vertical Loading. In *Proceedings of the Nineteenth International Offshore and Polar Engineering Conference*, volume 125, Osaka.

Simons, T. A., Weiler, R., Strege, S., Bensmann, S., Schilling, M., and Kwade, A. (2015). A ring shear tester as calibration experiment for DEM simulations in agitated mixers - A sensitivity study. *Procedia Engineering*, 102:741–748.

Sitbba Rao, K. S., Allam, M. M., and Robinson, R. G. (1998). Interfacial friction between sands and solid surfaces. *Proceedings of the Institution of Civil Engineers: Geotechnical Engineering*, 131(2):75–82.

Soltanbeigi, B., Podlozhnyuk, A., Ooi, J. Y., Kloss, C., and Papanicolopulos, S. A. (2017). Comparison of multi-sphere and superquadric particle representation for modelling shearing and flow characteristics of granular assemblies. *EPJ Web of Conferences*, 140:4–7.

Suhr, B. and Six, K. (2020). Simple particle shapes for DEM simulations of railway ballast: influence of shape descriptors on packing behaviour. *Granular Matter*, 22(2):1–17.

Sumer, B., Frefsoe, J., and Christiansen, N. (1992). Scour around vertical pile in waves. *Journal of Waterway Port Coastal Ocean Engineering*, 118(1):15–31.

Sumer, B. M., Christiansen, N., and Fredsøe, J. (1997). The horseshoe vortex and vortex shedding around a vertical wall-mounted cylinder exposed to waves. *Journal of Fluid Mechanics*, 332(February):41–70.

Szarf, K., Combe, G., and Villard, P. (2011). Polygons vs. clumps of discs: A numerical study of the influence of grain shape on the mechanical behaviour of granular materials. *Powder Technology*, 208(2):279–288.

Tanaka, H., Momozu, M., Oida, A., and Yamazaki, M. (2000). Simulation of soil deformation and resistance at bar penetration by the Distinct Element Method. *Journal of Terramechanics*, 37(1):41–56.

Thakur, S. C., Ooi, J. Y., and Ahmadian, H. (2016). Scaling of discrete element model parameters for cohesionless and cohesive solid. *Powder Technology*, 293:130–137.

Tran, Q. A., Chevalier, B., and Breul, P. (2013). DEM modeling of penetration test in static and dynamic conditions. *AIP Conference Proceedings*, 1542(June):225–228.

van Schepdael, A., Carlier, A., and Geris, L. (2016). Sensitivity analysis by design of experiments.

Wang, J., Qin, S., Jin, S., and Wu, J. (2015). Estimation methods review and analysis of offshore extreme wind speeds and wind energy resources. *Renewable and Sustainable Energy Reviews*, 42:26–42.

Wensrich, C. M. and Katterfeld, A. (2012). Rolling friction as a technique for modelling particle shape in DEM. *Powder Technology*, 217(January 2011):409–417.

Wexler, P. (2014). *Encyclopedia of Toxicology* . Academic Press, 3-rd edition edition.

Whitehouse, R. J., Harris, J. M., Sutherland, J., and Rees, J. (2011). The nature of scour development and scour protection at offshore windfarm foundations. *Marine Pollution Bulletin*, 62(1):73–88.

Wood, D. M. (2004). *Geotechnical Modelling*. CRC Press.

Yan, Z., Wilkinson, S. K., Stitt, E. H., and Marigo, M. (2015). Discrete element modelling (DEM) input parameters: understanding their impact on model predictions using statistical analysis. *Computational Particle Mechanics*, 2(3):283–299.

Zanke, U. C., Hsu, T. W., Roland, A., Link, O., and Diab, R. (2011). Equilibrium scour depths around piles in noncohesive sediments under currents and waves. *Coastal Engineering*, 58(10):986–991.

Zhang, Q., Jia, C., Yu, J., and Zhou, J. (2021). Multisphere Representation of Convex Polyhedral Particles for DEM Simulation. *Advances in Civil Engineering*, 2021:1–8.

Zhang, X., Zhai, W., and Zhao, C. (2017). DEM Analysis of Ballast Breakage Under Train Loads and Its Effect on Mechanical Behaviour of Railway Track. In *Proceedings of the 7th International Conference on Discrete Element Methods*, volume 188, pages v–vi.

Zhang, Z. and Wang, Y. H. (2014). 3D DEM simulation of a centrifuge model pile test. *Numerical Methods in Geotechnical Engineering - Proceedings of the 8th European Conference on Numerical Methods in Geotechnical Engineering, NUMGE 2014*, 1(June 2014):433–438.

Zhao, H., Zhang, J., Qiu, P., and Ji, S. (2019). Hierarchical Modeling Method for DEM Simulation and Its Application in Soil–Pile–Cap Interaction and Impact Case. *International Journal of Geomechanics*, 19(7):04019076.

Zheng, C. W., Li, C. Y., Pan, J., Liu, M. Y., and Xia, L. L. (2016). An overview of global ocean wind energy resource evaluations. *Renewable and Sustainable Energy Reviews*, 53(667):1240–1251.

Zhou, B., Huang, R., Wang, H., and Wang, J. (2013). DEM investigation of particle anti-rotation effects on the micromechanical response of granular materials. *Granular Matter*, 15(3):315–326.

Zhou, T., Hu, B., Wang, X., and Yan, B. (2012). Discrete element method analysis of mechanical properties of railway ballast during tamping process under different amplitude. *Applied Mechanics and Materials*, 233:224–227.

Zhu, H. P., Zhou, Z. Y., Yang, R. Y., and Yu, A. B. (2008). Discrete particle simulation of particulate systems: A review of major applications and findings. *Chemical Engineering Science*, 63(23):5728–5770.

Zhu, T. (2016). Some useful numbers on the engineering properties of material (geologic and otherwise).

A
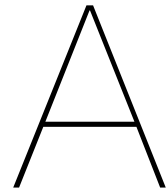
Results experimental penetration test

Appendix A comes with the data set used to create the average resistance for each case study. From the 5 repetitions included in each graph, a 95% confidence interval can be created. The pressure presented here is recorded by the manometer and can be translated into force by multiplying with the area of the cylinder (6 cm in diameter). Therefore, Figure A.1 shows the results from the 2 smaller diameter rocks while Figure A.2 reveals the penetration resistance of the 2 larger rock sizes. The diameter of the rocks is indicated by the d_{50} and the width of the penetrating plate is w.
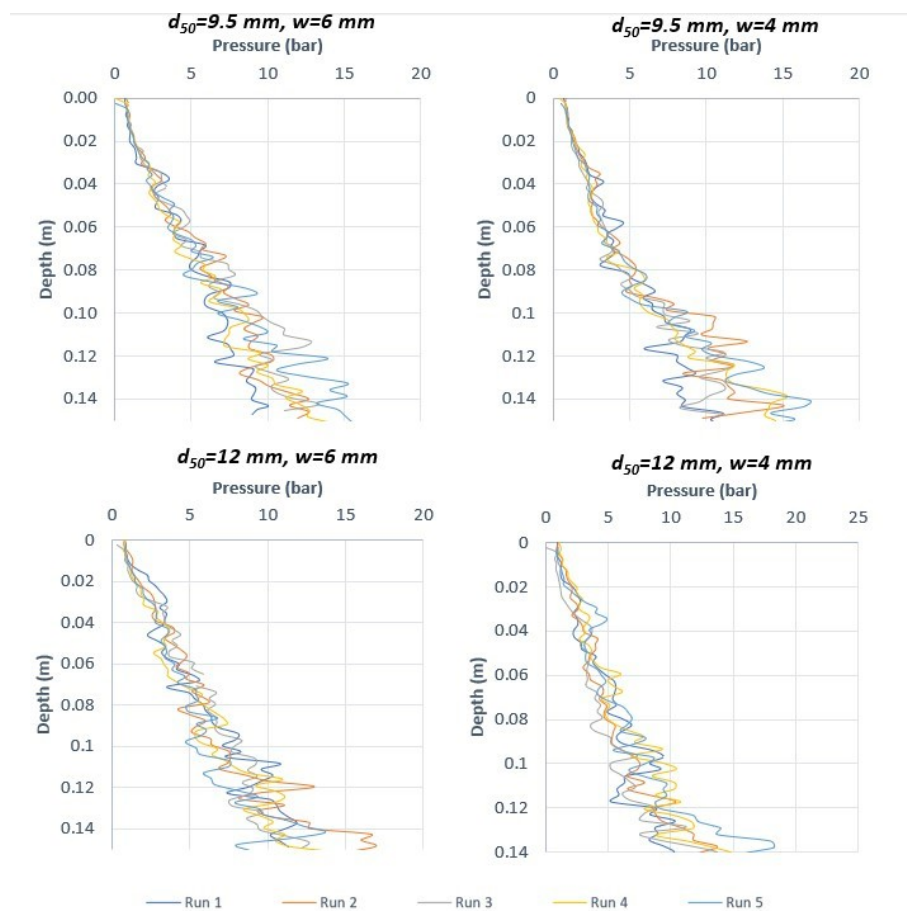
Figure A.1: Penetration test results experimental test (1/2)
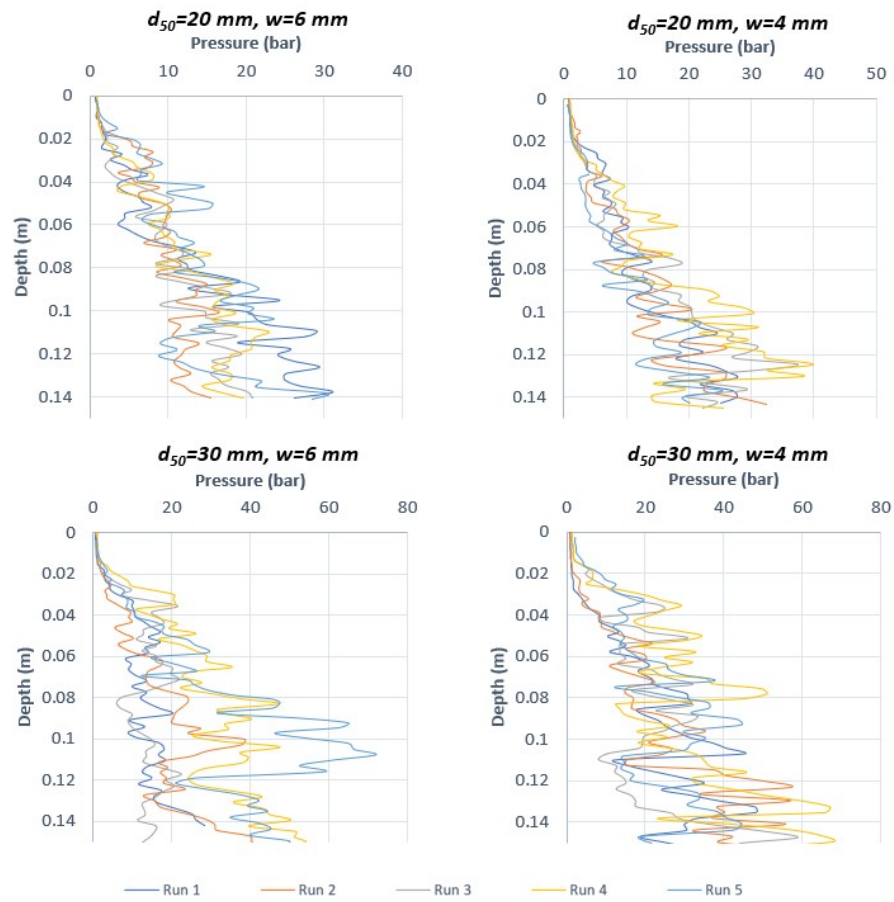
Figure A.2: Penetration test results experimental test (2/2)

B

Results additional experimental tests

Appendix B includes the results of the additional calibration tests performed in the laboratory. These results are used to aim the calibration of the DEM model. The tests performed give an approximation of the bulk density (ρ_{bulk}), the particle density (ρ_p), the coefficient of restitution between particles ($e_{p,p}$) and between particles and geometry ($e_{p,g}$), the static friction coefficient between particles and geometry ($\mu_{p,g}$) and the angle of repose (α_{AoR}) calculated using two different methods, the ledge test and the lifting cylinder test. Table B.2 indicates the results of the lifting cylinder test to determine the AoR for each material types used in the experiments for the DoE.

Table B.1: Results additional calibration tests $d_{50} = 30mm$

Notation [a]	Unit	Measured values
ρ_{bulk}	kg/m^3	1510, 1530, 1450
ρ_p	kg/m^3	3145, 3091, 3108, 3323, 3146, 2976, 3114, 3066, 3003, 2712
$e_{p,g}$	-	0.22, 0.26, 0.18, 0.18, 0.13, 0.18, 0.18, 0.18, 0.09, 0.09, 0.09, 0.18, 0.13, 0.13, 0.18, 0.22, 0.09, 0.09, 0.13, 0.13, 0.22, 0.26, 0.18, 0.09, 0.18
$e_{p,p}$	-	0.05, 0.04, 0.06, 0.09, 0.09, 0.06, 0.04, 0.09, 0.06, 0.04, 0.06, 0.05, 0.06, 0.09, 0.06, 0.04, 0.11, 0.04, 0.09, 0.04, 0.09, 0.05, 0.04, 0.04, 0.05
$\mu_{s,p,g}$	-	0.58, 0.70, 0.56, 0.63, 0.67, 0.66, 0.64, 0.60, 0.73, 0.75, 0.51, 0.50, 0.57, 0.68, 0.58, 0.57, 0.53, 0.54, 0.57, 0.66, 0.61, 0.61, 0.70, 0.61, 0.60
α_{AoR} (ledge test)	deg	52.27, 55.11, 56.88, 58.38, 56.19
Mass (ledge test)	kg	4.15, 3.25, 2.85, 4.0, 3.7
α_{AoR} (cylinder)	deg	set 1: 31,36.3, 41, 43.8, 39.5 set 2: 37, 27, 37.2, 37, 35.9 set 3: 25, 29.3, 38.4, 39.6, 36.7 set 4: 28.8, 43.2, 50.7, 34.1, 35.6 set 5: 39, 54, 29, 41.3, 45.9

[a] Particle (p) and Geometry (g)

Table B.2: Results additional validation tests: lifting cylinder AoR

d_{50}	AoR (deg)
9.5 mm	set 1: 33, 42, 39, 36, 35
	set 2: 42, 36, 42, 38, 43
	set 3: 37, 42, 37, 36, 36
12 mm	set 1: 40, 36.3, 34, 39.8, 36.3
	set 2: 37.7, 36.2, 35.5, 39.2, 41.5
	set 3: 38.7, 40.5, 36, 37.3, 40.7
20 mm	set 1: 35.1, 42, 41.6, 32.5, 36.8
	set 2: 34.2, 32, 42, 37, 35
	set 3: 38.1, 47, 41.3, 34, 34

C
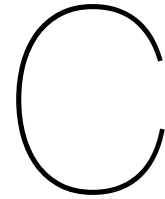
Results DEM calibration

This appendix presents the results of the DoE for calibration purposes of the DEM models. Table C.1 shows the results of the penetration test displayed in terms of work at 0.14 m penetration depth. The error is calculated according to Equation C.1, where the experimental value for the work is 726 J. The choice of variables included in the order of DoE is inserted in Table 5.2. A smaller error indicates that the response of that model is closer to the experimental determined value. Moreover, Table C.2 includes the results with the angle of repose, which modelled in a separate DEM model. The error is calculated in the same manner, but the experimental value in this case is 35 ^{o}. Lastly, Figures C.1, C.2, C.3 and C.4 include the graphs with the penetration resistance and work for each particle shape case of the DoE, plotted against the experimental results.

Table C.1: DEM results: DoE matrix for the penetration test (work is calculated at 0.14 m penetration depth)

Order DoE	1-sphere		2-sphere		4-sphere		Tetrahedron	
	DEM	% Error	DEM	% Error	DEM	% Error	DEM	% Error
1	24	97	16	98	13	98	17	98
2	36	95	20	97	18	98	17	98
3	35	95	22	97	23	97	15	98
4	54	93	62	92	86	88	94	87
5	901	22	113	84	106	85	83	89
6	1697	134	157	78	206	72	92	87
7	74	90	110	85	142	80	132	82
8	1709	135	213	71	348	52	133	82
9	3535	387	335	54	460	37	152	79

$$\%Error = \frac{value_{DEM} - value_{experiment}}{value_{experiment}} \qquad (C.1)$$

Table C.2: DEM results: DoE matrix for the AoR test (lifting cylinder test)

Order DoE	1-sphere		2-sphere		4-sphere		Tetrahedron	
	DEM	% Error	DEM	% Error	DEM	% Error	DEM	% Error
1	19	47	16	53	22	38	13	63
2	23	33	24	32	30	15	15	58
3	23	34	38	8	32	8	15	57
4	20	42	26	25	27	22	27	23
5	36	2	37	5	31	10	32	9
6	36	2	40	14	34	2	30	15
7	21	40	19	45	23	36	31	12
8	30	15	26	25	25	29	27	24
9	30	14	31	10	28	21	24	30
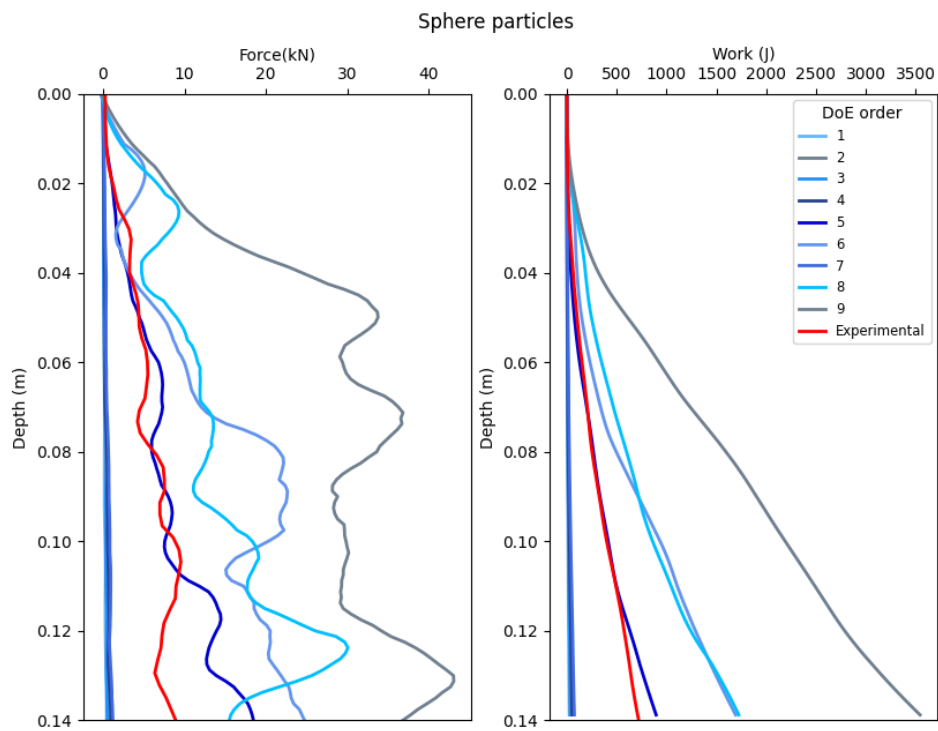
Figure C.1: Penetration resistance in spherical particles
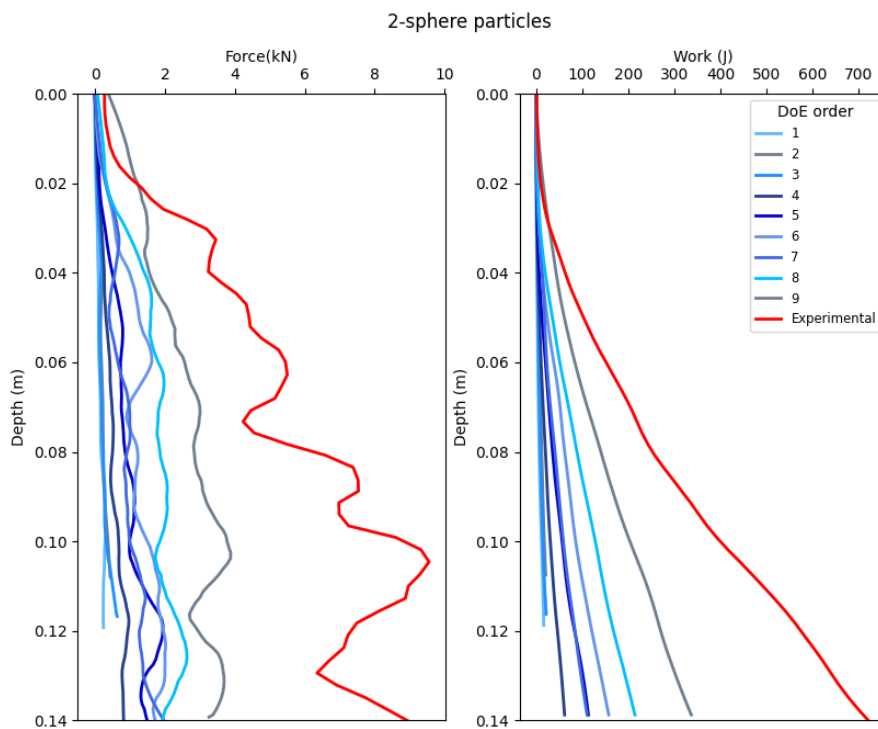
Figure C.2: Penetration resistance in 2-sphere particles
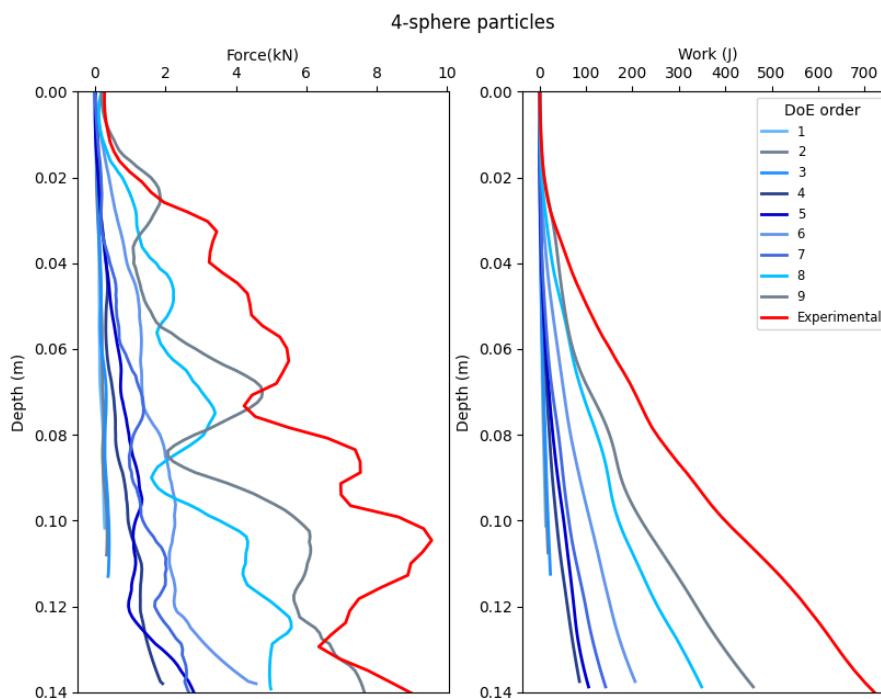
Figure C.3: Penetration resistance in 4-sphere particles
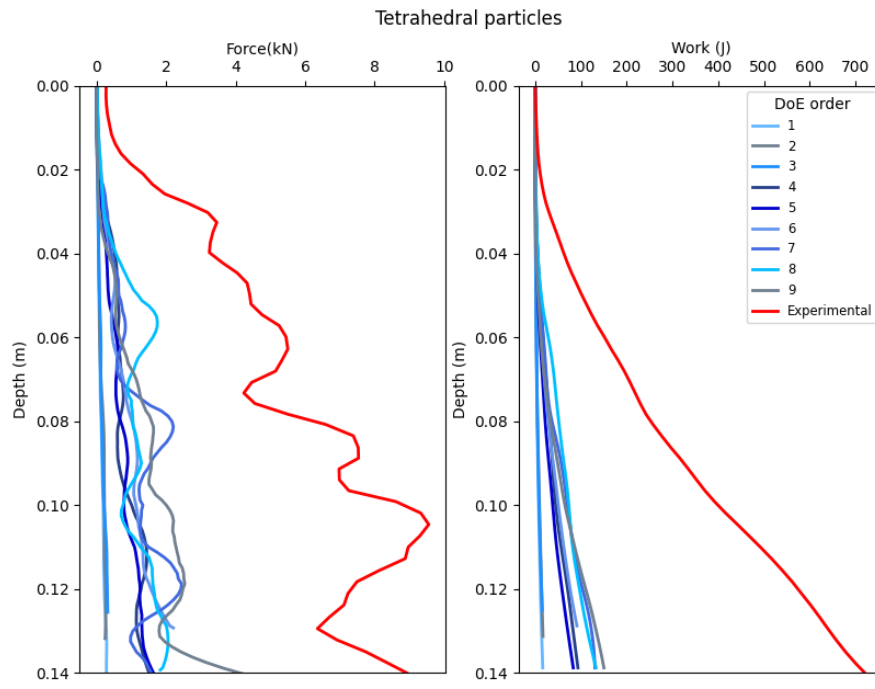
Figure C.4: Penetration resistance in tetrahedral particles

D
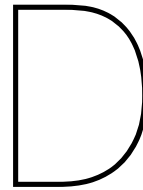
Codes

Listing D.1: Python code to determine the angle of repose of a pile of particles (adapted after Itasca (2019))

```python
# -*- coding: utf-8 -*-
"""
Created on Tue Apr 20 14:56:45 2021

@author: Teodora Barbuntoiu
"""

import numpy as np
from scipy.spatial.kdtree import KDTree
from scipy import optimize
from scipy import stats
import csv
from matplotlib import pyplot as plt

#Function which calulates the equation of a cone
def cone_eq(data,a,b):
    return a*(1-np.sqrt(data[:,0]**2+data[:,1]**2)/
                      (a*np.tan((90.0-b)*np.pi/180.0)))

#Function which finds the most extreme (highest) particles in the pile
def locally_extreme_points(coords, data, neighbourhood,
                           lookfor = 'max', p_norm = 2.):
    '''
    -->inputs:
    coords: A 2D array (n_points, n_dims) with point locations
    data: A vector (n_points, ) with point values
    neighbourhood: The size of the neighbourhood in which to search.
    lookfor: Either 'max', or 'min'
    p_norm:  Measuring distance (e.g. 1=Manhattan, 2=Euclidian)

    -->returns:
    filtered_coords: The coordinates of locally extreme points
    filtered_data: The values of these points
    '''

    extreme_fcn = {'min': np.min, 'max': np.max}[lookfor]
    kdtree = KDTree(coords)
    neighbours = kdtree.query_ball_tree(kdtree,
                                        r=neighbourhood, p = p_norm)
    i_am_extreme = [data[i]==extreme_fcn(data[n])
```

```
41                             for i, n in enumerate(neighbours)]
42      extrema, = np.nonzero(i_am_extreme) # This line just saves time on indexing
43      return extrema,coords[extrema], data[extrema]
44
45  #Function which fits a cone though the top of the pile and gives the confidence interval of 9
46  def fit_cone(AoR,CI, list_file_name):
47      '''
48      -->inputs:
49      list_file_name: List with the cvs files to input
50
51      -->returns:
52      t_fit: The repose angle
53      ci:    The student-t 95% confidence interval
54      '''
55
56      #intialize variables
57      data=[]
58      x=y=z=np.zeros((0))
59
60      # start loop for each csv file to process
61      for file in list_file_name:
62          with open(file) as csvfile:
63              readCSV = list(csv.reader(csvfile, delimiter=','))
64              x = np. array(readCSV[-5]) # x-position (final timestep)
65              y = np.array(readCSV[-4]) # y-position (final timestep)
66              z = np.array(readCSV[-3]) # z-position (final timestep)
67              d = np.array(readCSV[-2]) # diameter (final timestep)
68
69              x=np.delete(x, 0)
70              y=np.delete(y, 0)
71              z=np.delete(z, 0)
72              d=np.delete(d, 0)
73              x=np.array([float(numeric_string) for numeric_string in x])
74              y=np.array([float(numeric_string) for numeric_string in y])
75              z=np.array([float(numeric_string) for numeric_string in z])
76              d=np.array([float(numeric_string) for numeric_string in d])
77
78
79              rmin=np.min(d)/2
80              rmax=np.max(d)/2
81              ravg= 0.5*(rmin+rmax)
82              zmax=z+d/2
83
84              coords = np.vstack((x, y)).T
85
86
87              #Run function to calulate extreme values
88              extrema, newcoords,val = locally_extreme_points(coords, z,
89                                                 2.0*ravg,
90                                                 lookfor = 'max',
91                                                 p_norm = 1.)
92
93              xc = x[extrema]
94              yc = y[extrema]
95              zc = zmax[extrema]
96
97              cC = np.amax(zc)
98              mask_up = (cC - 2.0*rmax) > zc
99              mask_lo =  zc > (2.0*rmax)
100             xm = xc[mask_up ]
101             ym = yc[mask_up ]
```

```python
102                 zm = zc[mask_up ]
103                 data = np.vstack((xm, ym)).T
104
105                 p0 = [cC,40.0] # initial guess for optimization (AoR=40 deg)
106
107                 # Fit a cone on the local extrema and use scipy.optimize.curve_fit to estimate the con
108                 params, pcov = optimize.curve_fit(cone_eq, data, zm, p0)
109
110                 # student-t value for the dof and confidence level
111                 n = len(zm)          # number of data points
112                 p = len(params)      # number of parameters
113                 dof = max(0, n - p) # number of degrees of freedom
114                 alpha = 0.05         # 95% confidence interval = 100*(1-alpha)
115                 tval = stats.distributions.t.ppf(1.0-alpha/2., dof)
116
117                 ci = []
118                 for i, p,var in zip(range(n), params, np.diag(pcov)):
119                     sigma = var**0.5
120                     ci.append(sigma*tval)
121
122                 c_fit, t_fit = params
123                 R_fit = c_fit*np.tan((90.0-t_fit)*np.pi/180.0) #Find the R squared
124
125                 #print results
126                 print(file)
127                 print('AoR=%.1f' %t_fit)
128                 print('CI=%.2f'% ci[1])
129                 AoR=np.append(AoR,t_fit)
130                 CI=np.append(CI,ci[1])
131
132         return [AoR,CI]
133
134 #Change which files to open
135 list_file_name=['positions_particles.csv']
136
137 #Initialise variables
138 AoR=[]
139 CI=[]
140 #Run the main function
141 [AoR_final,CI_final]=fit_cone(AoR,CI,list_file_name)
142
143 #Plot AoR and confidence intervals
144 fig1, ax1 = plt.subplots()
145 ax1.scatter(AoR_final, CI_final)
```

$$E$$
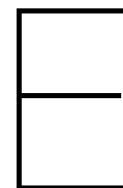
Additional simulations

This appendix contains the data generated for the validation of the DEM penetration test model, which uses different set of input parameters than the one decided in Chapter 5 after performing the DoE. Therefore, the penetration resistance is plotted for the case of spherical particle which have the following set of micro-parameters: $\mu_{s,p-p} = 0.6(-)$ and $\mu_{r_p,p} = 0.8(-)$. Two validation procedures are considered, the first one (option 1) involves keeping the particle size constant and varying the width of the penetrating tool (see Figure E.1 and the results from Table E.1). The second validation method (option 2) consists of varying the particle size such that the same ratios d_{50}/w as for the first validation method are achieved. The penetration resistance can be then compared with the results from the experimental analysis for the same ratios d_{50}/w, as displayed in Figure E.2. The graph shows that there is little to no correlation with the experimental results.
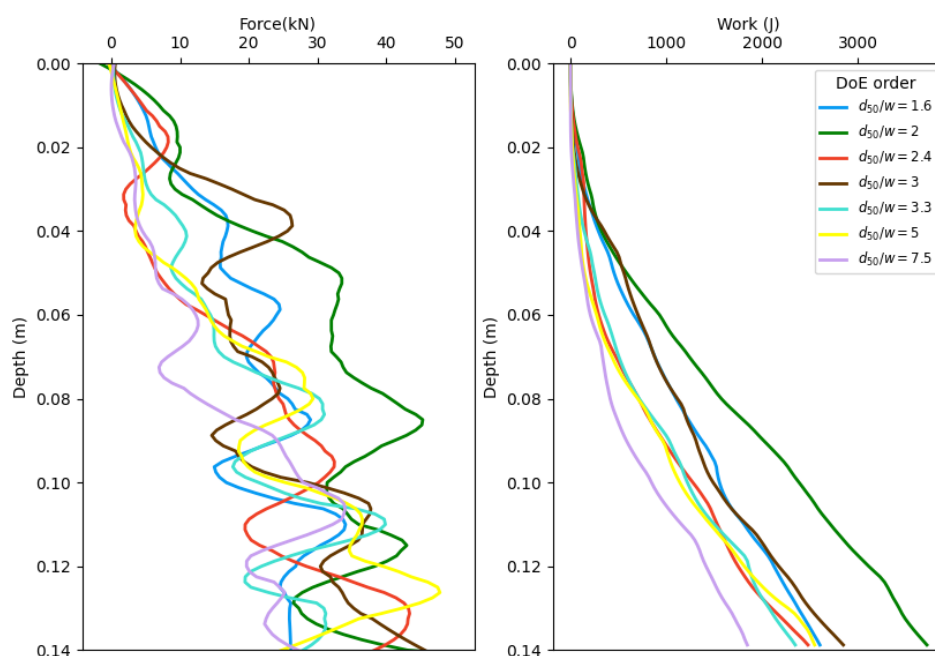
Figure E.1: DEM results of penetration resistance in spherical particles for multiple ratios d_{50}/w

Table E.1: DEM results of penetration work (calculated at 0.14 m depth) in spherical particles with a constant $d_{50} = 30mm$

d_{50}/w	1.6	2.0	2.4	3.0	3.3	5.0	7.5
Work (J)	2601	3717	2477	2846	2344	2547*	1844

* Calibrated reference case

Table E.2: DEM results of penetration work (in J) calculated at 0.14 m depth in spherical particles for multiple combinations of particle size and width of the penetrating tool

	d_{50}=9.5 mm	d_{50}=12 mm	d_{50}=20 mm	d_{50}=30 mm
w=6 mm	6.1	6.9	13.5	2547*
w=4 mm	5.6	5.4	13.3	1844

* Calibrated reference case
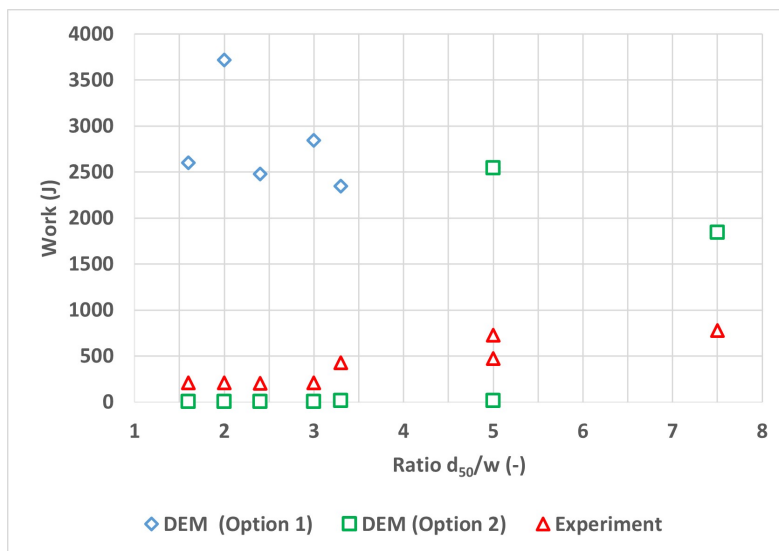
Figure E.2: Results of penetration test: validation comparison with the experimental test